Iraqi J. Laser, issue 2, vol., 20, pp. 1-7 (2021)

IRAQI
JOURNAL
OF
LASER

Hong-Ou-Mandel Dip Measurements of Two Independent Weak Coherent Pulses for Free Space Quantum Key Distribution Systems

Ahmed Ismael Khaleel[1,*] and Shelan Khasro Tawfeeq[1]
**Corresponding author: ahmed@ilps.uobaghdad.edu.iq*
1- Institute of Laser for Postgraduate Studies, University of Baghdad, Baghdad, Iraq

(Received 15/07/2021; accepted 08/12/2021)

Abstract: Preparation of identical independent photons is the core of many quantum applications such as entanglement swapping and entangling process. In this work, Hong-Ou-Mandel experiment was performed to evaluate the degree of indistinguishability between independent photons generated from two independent weak coherent sources working at 640 nm. The visibility was 46%, close to the theoretical limit of 50%. The implemented setup can be adopted in quantum key distribution experiments carried out with free space as the channel link, as all the devices and components used are operative in the visible range of the electromagnetic spectrum.

Keywords: Two-photon interference, indistinguishable photons, MDI-QKD protocol

1. Introduction

The request of implementing quantum key distribution (QKD) protocols with commercially available devices is increasing. The goal is to achieve reliable QKD systems with practical devices and components. This will combine the perfect secrecy offered by QKD protocols and the reliability of the available devices [1].

In 2012 a protocol named measurement-device-independent QKD (MDI-QKD) was presented [2], it removes all loopholes that may cause a security problem in detectors. The key idea of MDI-QKD is that both users (Alice and Bob) act as senders. They transmit signals to a third party (Charlie) which might be untrusted and is supposed to perform a Bell state measurement (BSM) on the incoming signals. Alice and Bob can use imperfect single-photon sources such as attenuated lasers and conclude the contributions from signals containing single-photon. Charlie performs BSM setup using linear optical components, which consists of a 50/50 beam splitter (BS), two polarizing beam splitters (PBSs), and four single-photon detectors (SPDs) [2].

Measuring independent photons with BSM setup will project theses photons into one of the four bell states if theses photons were distinguishable, i.e. they differ in one or more of their characteristics. If the independent incoming photons were indistinguishable in all of their degrees of freedom and met at the beam splitter at the same instant of time then an interference between them will occur causing what is called a Hong-Ou-Mandel (HOM) effect. In this effect, the coincidence measurement between the outputs of the BS will be minimum, known as HOM dip. If single-photon sources were used as independent sources, then coincidences is suppressed completely. For the case of using weak coherent pulses (WCP) as independent sources, the coincidence between them is limited to 50% of their non-interfered case [3].

The basic principle to explain interference is the superposition principle. In classical physics, light is composed from electromagnetic waves, the interference effect is explained by making superposition of these waves. In quantum physics, light quanta is adopted instead of electromagnetic waves, the interference is described by superposition of probability amplitudes. Despite the different approaches, both descriptions typically give the same behavior of single-photon interference [4].

In order to study the interference in quantum physics, two-photon interference is used along with single-photon interference. As the two-photon interference is a second-order interference effect, and it is the simplest higher-order interference of light. Two-photon interference is referred to quantum interference as a result of the quantum nature of the photon [5, 6].

Generating and engineering quantum states are important demands for many quantum applications, in addition with investigating HOM effect for these quantum states, different processes could be realized such as entanglement swapping and entangling independent photons generated by independent sources [7, 8]. In such experiments, precise timing synchronization between the photons from independent sources is required in order to provide accurate temporal matching. [9]

Spontaneous parametric down conversion (SPDC) process was used to generate photon-pairs that was first used to observe two-photon interference between single photons when fed to a beam splitter in its input ports resulting in a decrease in the coincidence counts at the outputs yielding a HOM dip. The same experiment is conducted with independent SPDC-based sources as independent sources, producing entanglement swapping process. WCP's can be used to observe two-photon interference in a setup where coincidence measurements are used to post-select two-photon states from mixed states which is known as entangling process [5, 10-14].

In this paper, a HOM experiment is performed in order to check the indistinguishability of the photons generated from two independent laser sources. These laser sources produce WCP that will be fed to HOM setup. Different optical components will be used in the experiment such as optical filters, attenuators, beam splitter, polarization controllers, fiber coupler and single-photon detectors.

2. Hong-Ou-Mandel Setup

In 1987, Hong, Ou, and Mandel (HOM) had demonstrated an experiment to investigate the two-photon interference effect [15]. This effect occurs if two identical single photons interfere at 50:50 beam splitter. If they overlap perfectly in time, the two photons will always leave the beam splitter from the same port. High degree of interference is directly associated to how much the two photons are identical in their polarization, intensity and wavelength, and how perfectly they will interfere spatially and temporally at the beam splitter. However, when the photons are completely generated from independent sources, this is never easy to achieve. Observing high visibility with fully independently generated photons might be considered as an indicator of approving photon indistinguishability and time overlap [15-18].

If two photons are incident on 50/50 beam splitter at its two input modes as shown in Figure 1.

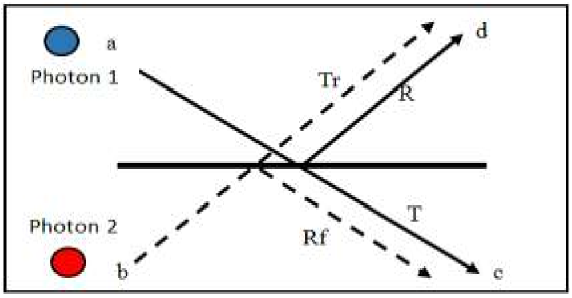

Figure (1): Schematic diagram of ideal beam splitter

They will exit the beam splitter according to the following transformation formula [15,18].

$$|1,1\rangle_{ab} = \hat{a}^{\dagger}\,\hat{b}^{\dagger}|0,0\rangle_{ab} \rightarrow (Tr\hat{c}^{\dagger} + Rf\hat{d}^{\dagger})\,(Rf\hat{c}^{\dagger} + Tr\hat{d}^{\dagger})\,|0,0\rangle_{cd} = (Tr^{2} + Rf^{2})|1,1\rangle_{cd} + \sqrt{2}TrRf\,(|2,0\rangle_{cd} + |0,2\rangle_{cd}) \;\ldots\ldots\ldots\ldots (1)$$

Where a and b denotes the input modes of the beam splitter, c and d are the output modes, *Tr* is the transmittance of the beam splitter and *Rf* is its reflectance.

According to equation 1 there are four possibilities, first: both photons are transmitted, second: both photons are reflected, third: photon (1) is transmitted and photon (2) is reflected, fourth: photon (1) is reflected and photon (2) is transmitted [9].

In general, HOM setup is constructed as shown in Figure 2.

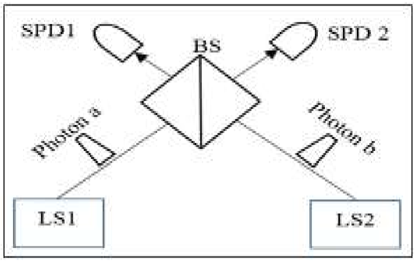

Figure (2): Basic HOM setup. LS: laser source, BS: 50/50 beam splitter, SPD: single-photon detector [9]

If the photons (a and b) were distinguishable, i.e. differ in one or more of their properties such as polarization, frequency or intensity, then all the above mentioned possibilities will be equally likely to occur.

If the photons were indistinguishable, i.e. identical in all of their properties, then the cases when the photons are both transmitted or both reflected, are cancelled out. Only two outcomes will occur by which the two photons will always take the same output path and they will be both directed to the same SPD. Achieving two-photon interference with indistinguishable photons require a temporal and spatial overlap between the two photons at the beam splitter [9].

Visibility is defined generally as

$$V = 1 - \frac{P_1}{P_2} \quad \ldots\ldots\ldots\ldots\ldots\ldots\ldots\ldots\ldots\ldots\ldots (2)$$

where P_1 represents the coincidence count rate for perfect overlap between photons and P_2 represents the coincidence count rate when the photons are sufficiently off with respect to each other. Theoretically when using indistinguishable single photons in a HOM experiment then V=1 as P_1=0 for perfect interference case.[18]

If two WCPs are used, the relation between the visibility and mean photon number per pulse in addition with the polarization mismatch between the pulses is defined as [18, 19]

$$V = \frac{2M * cos^2\phi}{(M+1)^2} \quad \ldots\ldots\ldots\ldots\ldots\ldots\ldots\ldots\ldots\ldots\ldots (3)$$

Where $M = \mu_1/\mu_2$, μ_1 *and* μ_2 are the mean photon number of WCP1 and WCP2 respectively. ϕ is the angle of polarization difference between WCP1 and WCP2. In order to conclude maximum visibility, μ_1 *and* μ_2 must be equal and ϕ must be zero. The maximum achievable visibility when using WCPs is V=0.5. To achieve this, the two interfering coherent states should be identical (i.e., polarization, intensity, frequency in addition with spatial and temporal overlap). For such identical states, laser pulses should be prepared properly.

Checking for a stable HOM interference with high visibility (near 0.5) is a mark for reaching high degree of indistinguishability between independent photons [14] . Figure 3 shows the coincidence counts resulted from the original experiment carried out by Hong, Ou and Mandel in 1987 , in this experiment the position of the beam splitter was shifted in order to achieve perfect spatial overlap between the photons. From the figure, the obtained visibility V=1 as the photons used in the experiment were originated from SPDC process [15]

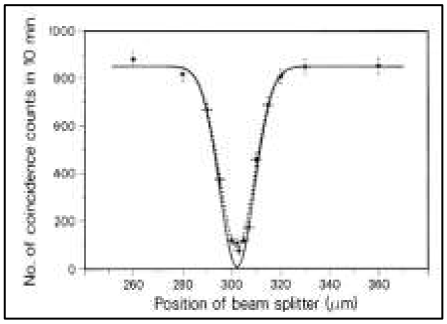

Figure (3): The measured number of coincidences as a function of beam-splitter displacement [15]

3. Detector's Timing resolution

Joint measurements of independent photons are the base for different quantum processes like entanglement swapping, teleportation, etc. To guarantee the required indistinguishability, the two photons, which are originated from different sources, have to meet together at a certain and fixed temporal delay. In order to practically achieve simultaneity, it is useful to use sources working in pulsed excitation mode, by which, the synchronization of the emission times can be controlled and the path lengths are equalized, such that the photons will arrive at the beam splitter at the same time [9, 17, 20]. A different approach might be considered, without performing any timing control for simultaneous emission of independent photons. Time-resolved detection of the photons might be adopted. In this approach, photons are detected at random times due to their random emission times. Among all these randomly arriving photons, only those detected at the same time, are considered for post-selection. This will help to distinguish between photons depending on their arriving times. In such process, the timing resolution of the detectors becomes crucial [21-23] .

For better understanding, consider a detector with timing resolution (T_d), a photon with coherence time (τ_c). Two cases might be discussed as shown in Figure 4.

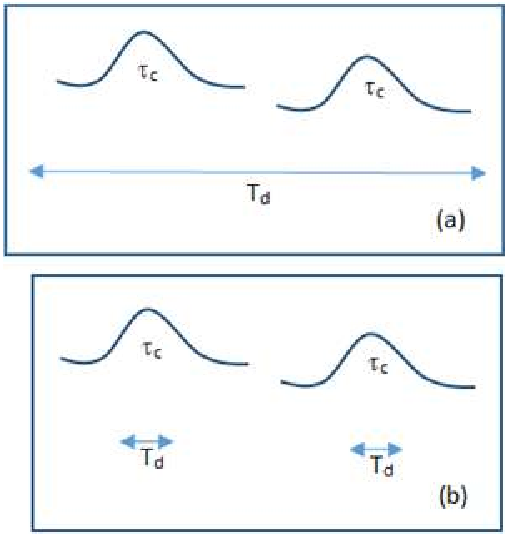

Figure (4): Two photons arrive with a delay of more than their coherence time τ. (a) A detector with a temporal resolution of $T_d > \tau_c$ cannot distinguish them. (b) A detector with a temporal resolution of $T_d < \tau_c$ can distinguish them. [21]

If two photons arrive with a delay **t** between them such that $\tau_c < t < T_d$, as shown in figure 4(a), they will be detected at the same time as the detector cannot distinguish between them although they are distinguishable in principle.

But if $\tau_c > T_d$ as shown in Figure 4 (b), the two photons will be detected at different times as the detector will distinguish between them. Based on such possibility, joint measurement experiments depend on the relation between the coherence time of the photons and the timing resolution of the detectors used [21-23].

4. Experiment and Results

In order to measure the frequency difference between laser sources used. A simple setup is implemented which consists from laser sources, beam splitter and a photodiode, as shown in Figure 5(a). The detected signal represents the beating signal between the two interfered signals which is the frequency difference of the two sources. The fast Fourier transform (FFT) signal is displayed on an oscilloscope as shown in Figure 5(b). The beating frequency is found to be within the limit of 20 MHz. This frequency difference is much smaller than the bandwidth of the optical pulses used in the experiment, as the pulse width is 5 ns and the corresponding bandwidth is 200 MHz. [2,18].

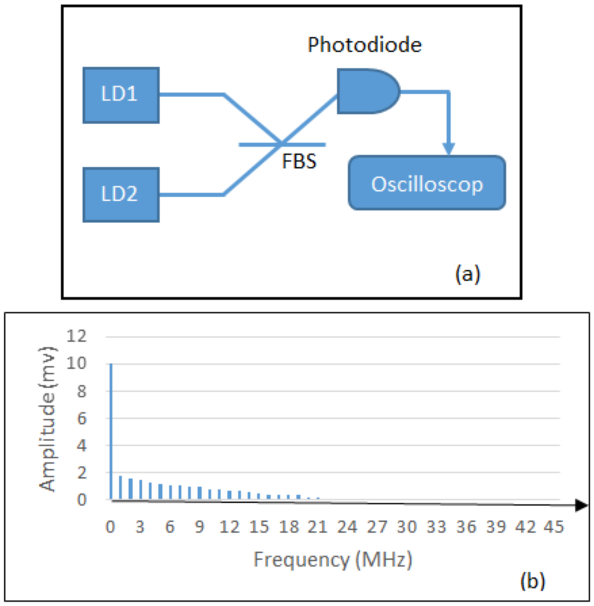

Figure (5): Beating Signal Measurement. (a): experimental setup, (b): FFT of the beating signal

In order to experimentally check the in distinguishability between the optical pulses of our laser sources, the following setup was built as shown in Figure 6.

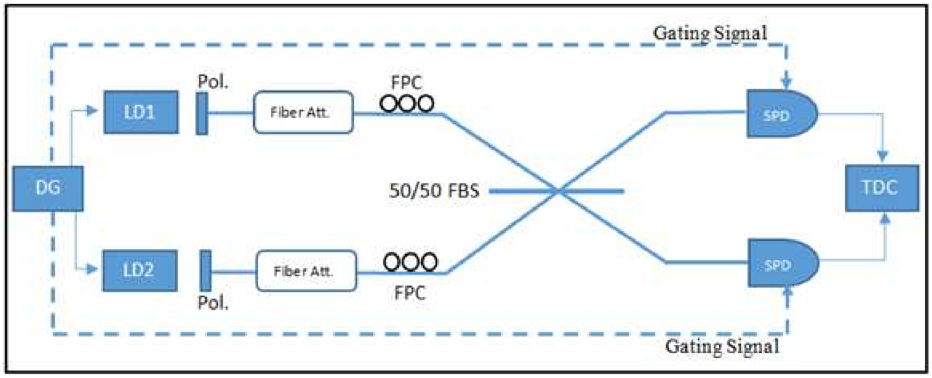

Figure (6): Experimental setup. DG: delay generator, LD: laser diode, Pol.: polarizer, Att.: attenuator, FPC: fiber polarization controller, FBS: fiber beam splitter, SPD: single-photon detector, TDC: time-to-digital convertor.

For the experiment, two laser diodes (NPL64B from Thorlabs) were used, the wavelength is 640 nm, the output pulse width of the lasers can be adjusted from 5 ns to 39 ns. Different fiber-based components were used such as fiber polarization controller (FPC), fiber coupler and variable optical attenuator. These components (from Thorlabs) were selected such that their operation is in the (600-800) nm range.

The detectors are single-photon detectors (PDM series from Micro Photon Devices) with detection efficiency of 40% at 640 nm. The timing resolution is about 250 ps, and they can be operated in two modes free-running and gated mode. Time-to-Digital converter (TDC) device was used (id800 from id-quantique), it contains 8 channels as inputs, with 81 ps bin width.

The procedure of the experiment is as follows: both LDs are run and controlled using the delay generator, their output pulses must have the same polarization states and the same mean photon number. These identical pulses are to interfere with each other at the fiber beam splitter (FBS) which is used to guarantee the spatial overlap between the pulses. The outputs of the FBS are connected to the detectors. A coincidence counts between the outputs of the detectors are to be monitored and registered by TDC. The pulse widths of the laser diodes are set to their minimum value (5ns) and the repetition rate is set at 10 MHz . A delay in the starting time of one of the lasers with respect to the other is carried out by the delay generator. The polarization of the lasers is set to horizontal polarization using optical polarizers. Precise alignment of each FPC is produced by rotating its paddles until observing maximum count rates at the detectors output. The mean photon number,μ, of the LDs is set to 0.3 photon/pulse during the experiment, this was done by adjusting both VOAs. The single-photon detectors were operated in gated mode. The width of the gating signal was set to 70 ns. The output of both SPDs are connected to TDC to monitor and record the coincidence counts between the lasers for different time delay points in order to observe the HOM effect. The delay between the independent LD pulses is changed in steps of 100 ps so that the pulses are first separated and then they gradually overlapped with each other till they overlap completely, the process continues till they are separated again, meanwhile the coincidence counts between the detectors are registered at each step. The width coincidence window was 20 ns.

The complete coincidence counts versus time delay are plotted in Figure 7.

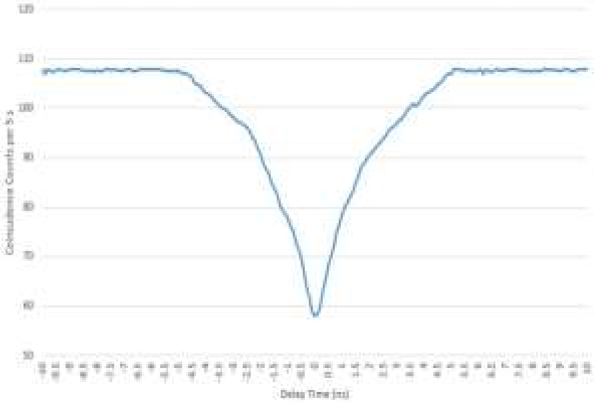

Figure (7): Coincidence counts versus delay time

From Figure 7, the visibility is calculated (equation 2) to be V=46%, close to the theoretical limit of 50%. Different factors might cause the difference in the experimental and the theoretical values such as polarization mismatch, intensity mismatch or spectrum difference.

5. Conclusions

From this work, a Hong-Ou-Mandel experiment was implemented using the experimental setup shown in Figure 6. The results showed that this setup can be used to perform joint measurement to check the indistinguishability between independent photons from two independent weak coherent sources. Which means that these sources are suitable to be used with quantum communication protocols such as MDI-QKD protocol. Based on the laser sources and optical components used in the experiment, since they are all operate in the visible range, free space channel link can be adopted in the implementation of the experiment and taking the advantage of using available laser sources in the visible range. Another advantage is the usage of high detection efficiency offered by the available single-photon detectors, which will help to improve the efficiency of the experiment.

References

[1] Z. Tang, Z. Liao, F. Xu, B. Qi, L. Qian, and H.-K. Lo, “Experimental demonstration of polarization encoding measurement-device-independent quantum key distribution" Phys. Rev. Lett., vol. 112, 190503, 2014.

[2] H. Lo, M. Curty, and B. Qi, “Measurement-device-independent quantum key distribution" Phys. Rev. Lett., vol. 108, 130503, 2012.

[3] Y. Kim, O. Slattery, P. Kuo, and X. Tang, “Conditions for two-photon interference with coherent pulses” PHYS REV A, vol. 87, 063843, 2013.

[4] Y. Kim, O. Slattery, P. Kuo, and X. Tang, “Two-photon interference with continuous-wave multi-mode coherent light” Opt. Express, vol. 22, 3611-3620, 2014.

[5] J. Rarity, P. Tapster, and R. Loudon, “Nonclassical interference between independent sources”, Journal of Optics B: Quantum and Semiclassical Optics, vol. 7, S171, 2005.

[6] J. Liu, D. Wei, H. Chen, Y. Zhou, H. Zheng, H. Gao and Z. Xu, “Two-photon interference with non-identical photons” Opt. Commun. vol. 354, 79-83, 2015.

[7] Y. Xue, A. Yoshizawa and H.Tsuchida, “Hong−Ou−Mandel dip measurements of polarization-entangled photon pairs at 1550 nm” Opt. Express, vol. 18, 8182-8186, 2010.

[8] H. Chen, X. An, J. Wu, Z. Yin, S. Wang, W. Chen and Z. Han “Hong–Ou–Mandel interference with two independent weak coherent states’ Chin. Phys. B, vol. 25, 020305, 2016.

[9] Y. Tsujimoto, Y. Sugiura, M. Tanaka, R. Ikuta, S. Miki, T. Yamashita, H. Terai, M. Fujiwara, T. Yamamoto, M. Koashi, M. Sasaki and N. Imoto “A high visibility Hong-Ou-Mandel interference via a time-resolved coincidence measurement” Opt. Express, vol 25, 12069-12080, 2017.

[10] T. Silva, G. Amaral, D. Vitoreti, G. Temporao and J. Weid “Spectral characterization of weak coherent state sources based on two-photon interference” J OPT SOC AM B , vol 32, 545-549, 2015.

[11] F. Bouchard, A. Sit, Y. Zhang, R. Fickler, F. Miatto, Y. Tao, F. Sciarrino and E. Karimi “Two-photon interference: the Hong–Ou–Mandel effect” Rep. Prog. Phys., vol 84, No. 1, 2020.

[12] A. Nomerotski, M. Keach, P. Stankus, P. Svihra and S. Vintskevich “Counting of Hong-Ou-Mandel Bunched Optical Photons Using a Fast Pixel Camera” Sensors, vol. 20, No. 12, 2020.

[13] H. Kim, O. Kwon and H. Moon “Two-Photon Interferences of Weak Coherent Lights” Scientific Reports, 2021. DOI: https://doi.org/10.21203/rs.3.rs-663547/v1.

[14] H. Ollivier, S. Thomas, S. Wein, I. Maillette de Buy Wenniger, N. Coste, J. Loredo, N. Somaschi, A. Harouri, A. Lemaitre, I. Sagnes, L. Lanco, C. Simon, C. Anton, O. Krebs and P. Senellart ” Hong-Ou-Mandel Interference with Imperfect Single Photon Sources” Phys. Rev. Lett., vol 126, 063602, 2021.

[15] C. Hong, Z. Ou, and L. Mandel, “Measurement of subpicosecond time intervals between two photons by interference," Phys. Rev. Lett., vol. 59, 2044-2046, 1987.

[16] T. Silva, D. Vitoreti, G. Xavier, G. Amaral, G. Tempor˜ao, and J. von der Weid, “Proof-of-principle demonstration of measurement-device-independent quantum key distribution using polarization qubits”, Phys. Rev. A, vol. 88, 052303, 2013.

[17] M. Halder, A. Beveratos, N. Gisin, V. Scarani, C. Simon and H. Zbinden, “Entangling Independent Photons by Time Measurement” Nature Phys., vol. 3, 692-695, 2007.

[18] Z. Liao, *Experimental Realization of Decoy State Polarization Encoding Measurement-Device-Independent Quantum Key Distribution,* M.Sc. thesis, University of Toronto, TO, 2013.

[19] E. Moschandreou, J. Garcia, B. Rollick, B. Qi, R. Pooser and G. Siopsis, “Experimental study of Hong-Ou-Mandel interference using independent phase randomized weak coherent states” arXiv, 1804.02291, 2018.

[20] T. Legero, T. Wilk, A. Kuhn, and G. Rempe, “Time-resolved two-photon quantum interference” Appl. Phys. B, vol. 77, 797–802, 2003.

[21] M. Halder, *Quantum communication with photonic entanglement,* Ph.D. thesis, University of Geneve, GE, 2007

[22] T. Silva, G. Xavier, and J. von der Weid, “Real-time characterization of gated-mode single-photon detectors”, IEEE Journal of Quantum Electronics, vol. 47, 1251–1256, 2011.

[23] C. Kurz, *Quantum Interference of Unpolarized Single Photons,* Diploma thesis, University of Munich, MU, 2010.

قياسات قعر هونك-او-ماندل لنبضتين متشاكهتين ضعيفتين مستقلتين لأنظمة توزيع المفتاح الكمي في الفضاء الحر

احمد اسماعيل خليل، شيلان خسرو توفيق

معهد الليزر للدراسات العليا, جامعة بغداد، بغداد - العراق

الخلاصة: عملية تحضير فوتونات متماثلة هي محور للتطبيقات الكمية كتبادل الفوتونات المتشابكة و عملية التشابك.تم تقديم تجربة (هونك-او-ماندل) لحساب درجة عدم التمايز بين فوتونات تتكون من مصدرين منفصلين بطاقة ضعيفة و متشاكهين تعمل بطول موجي 640 نانومتر. مقدار الرؤية كان بقيمة (46%) و قريبة من الحد النظري بقيمة (50%). بالأمكان استخدام هذه التجربة في تجارب توزيع المفتاح الكمي و التي تنفذ في الفضاء و اعتباره كقناة اتصال ، باعتبار ان كل الأجهزة و المواد و التي تم استخدامها في منطقة الطيف المرئي من المجال الكهرومغناطيسي.

Iraqi J. Laser, issue 2, vol., 20, pp. 8-17 (2021)

IRAQI
JOURNAL
OF
LASER

Parametric Optimization for Fatigue Life of 6061-T6 Aluminum Thin Sheets Processed with High-Speed Laser Shock Peening

Ali M. Khudhair[1,*], **Furat I. Hussein**[2]

**Corresponding author: ali.mohammed1201a@ilps.uobaghdad.edu.iq*

1. *Institute of Laser for Postgraduate Studies, University of Baghdad, Iraq, Baghdad, Iraq.*
2. *Mechatronics Eng. Dep., Al-Khwarizmi College of Engineering, University of Baghdad, Baghdad, Iraq.*

(Received 11/10/2021; accepted 09/12/2021)

Abstract: Aluminum alloys grade 6061-T6 are characterized by their excellent properties and processing characteristics which make them ideal for varieties of industrial applications under cyclic loading, aluminum alloys show less fatigue life than steel alloys of similar strength. In the current study, a nanosecond fiber laser of maximum pulse energy up to 9.9 mJ was used to apply laser shock peening process (LSP) on aluminum thin sheets to introduce residual stresses in order to enhance fatigue life under cyclic loading Box-Behnken design (BBD) based on the design of experiments (DOE) was employed in this study for experimental design data analysis, model building and optimization The effect of working parameters spot size (ω), scanning speed (v) and pulse repetition rate (PRR) at three levels on the fatigue life expressed by the number of cycles (noc) were investigated The experimental results show an exclusive and significant percentage increase in the fatigue life of 505.25% and 477.81% when the ω= 0.04 mm and PRR= 22.5 kHz for two scanning speeds 200 mm/s and 500 mm/s respectively The optimized data extracted from the built model suggest a number of input parameters sets to enhance the performance of the process.

Keywords: fiber laser, aluminum alloy, LSP, high speed, DOE, fatigue.

1. Introduction

Aluminum alloys grade 6061-T6, are characterized by their good corrosion resistance, high strength-to-weight ratio and high toughness. Their excellent processing and welding characteristics make them ideal for varieties of industrial applications. Aluminum alloys find their ways widely in aircraft, automobiles, locomotives, couplings, marine, hydraulic pistons, appliance fittings, valves parts, bike frames and other industries [1, 2].

Under cyclic loading, aluminum alloys show less fatigue life than steel alloys of similar strength [3]. Laser shock penning (LSP) is introduced as one of a cold work surface treatment that enhances fatigue life [4]. Many research works revealed that mechanical properties such as tensile strength, hardness, wear resistance, and corrosion resistance are notoriously improved with LSP [5, 6]. Introducing residual stresses disrupt cracks growth rate and improve mechanical properties such as wear-resistance and fatigue life [7]. Short pulse lasers of high intensity (1 GW/cm^2) improve the surface strength and disrupt flaw propagation by imparting a layer of high compressive residual stresses [8, 9]. Even though nanosecond pulses are shorter than millisecond pulses, the interaction's nature remains thermal compared with shorter pulses such as femtosecond pulses [10, 11]. LSP is a process in which intense-short laser pulses pass through a transparent confining medium (such as water or glass) and focus on a metal surface covered with an absorbing layer. The latter may be an aluminum foil or black film that immediately vaporizes to form expanded plasma resulting in shockwaves against the processed metal followed by residual stresses and microstructure alterations [12]. When the pressure of the shockwave exceeds the material's dynamic yield strength, or HEL

(Hugoniot Elastic Limit), the material exhibits extremely high-stress deformation of about 10^6-10^7 GW/cm2 in a short time, causing local plastic deformation and compressive residual stresses [13].

Many research works investigate the role of LSP in enhancing the performance of cyclic operation for aluminum parts. Rubio-González et al. [14] evaluated the effect of different values of pulse densities on the residual stress field and fatigue crack initiation life. The study revealed higher pulse densities reduce fatigue crack growth and improve the fracture toughness characteristics for tested Al 6061-T6 alloy. Ahmed R. Alhamaoy et al. [15] had applied LSP to improve the cycle fatigue performance for Al 6061-T6 shafts coated with gel as an ablative layer without adding confining medium. Their results show a significant increase in the fatigue life when higher laser pulse energy is used. X. Q. Zhang et al. [16] applied two-sided LSP for Al 7050-T6 alloy to study residual stresses formation, surface feature and fatigue fracture morphology. The compressive residual stress cracks initiation and propagation rate. J. Shenget al. [17] utilized different laser pulse energies to study their effects on the crack propagation behavior for Al 6061-T6 alloy. They concluded that residual stresses caused by expanded plasma pressure could cancel tensile residual stress, reduce the notch driving force as well, and finally delay fatigue. Liu et. al., [18], has studied the effects of laser power density on the fatigue life of Al 7050 alloy subjected to LSP. Both the experimental and numerical results showed that a carefully chosen laser power density, when treating materials like aluminum alloys, can prevent internal cracking.

This paper aims to study the effects of manipulating LSP working parameters on the fatigue life of Al 6061-T6 alloy and utilize a statistical approach to develop a model capable of optimizing the working parameters of the process.

2. **Experimental Work**

An Al 6061-T6 thin plate was employed in this investigation. The chemical composition analysis (Table 1) was carried out at the Baghdad lab of the State Company for Inspection and Engineering Rehabilitation (SIER) in Baghdad. A tensile test was applied for a group of specimens to evaluate the mechanical properties of the alloy. The tensile specimens were cut and prepared according to the standard test method ASTM-E8 [19]. The tensile test was performed at speed of 2 mm/min using 100 kN Universal Testing Machine (Tinius Olsen (H100kU)\USA) under plane stress conditions.

Table (1) The Chemical Composition of Employed Al 6061-T6 Alloy

Element	The percentage ratio %
Si	00.677
Fe	00.548
Cu	00.236
Mn	00.131
Mg	00.844
Cr	00.179
Zn	00.0046
Ti	00.0787
P	00.0012
Pb	00.0094
Al	97.2

Table (2) lists some of the mechanical properties for the employed alloy according to the applied tensile test.

Table (2) Mechanical properties of Al 6061-T6

Property	Experimental
Yield Strength (MPa)	276
Ultimate Strength (MPa)	310
Elongation %	12%
Modulus of elasticity (GPa)	68.9

A thin plate of Al 6061-T6 of 1.6 mm thickness were cut in rectangular shapes of 10 mm × 100 mm dimensions according to the requirement of the fatigue testing device. Black paint was uniformly sprayed with a consistent thickness of 140 µm over the processed area on both sides of the specimen surface as a protective ablating layer as shown in figure (1a). A water layer of 2 mm to 3 mm height over the upper surface of the specimen was applied as a transparent confining layer and to support the built pressure by the plasma plume and reduce possible thermal effects. A nanosecond fiber laser model RFL-P\China (Figure (1b)) that was used in the current study has the following characteristics of 1064 nm wavelength, 81 ns pulse duration, max average power of 100 W and max pulse energy of 9.9 mJ.

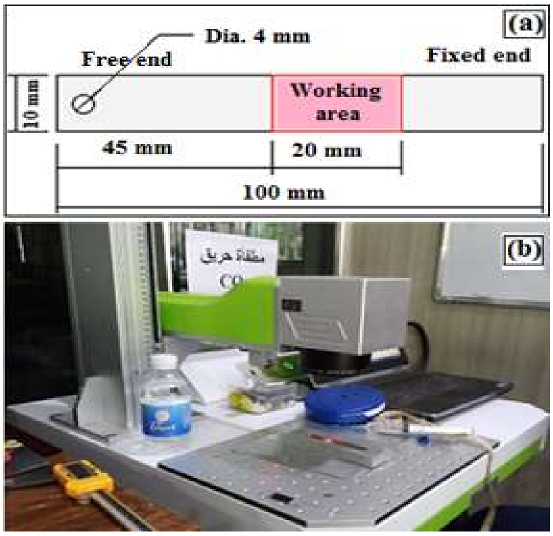

Figure (1): Experimental setup: **a)** fatigue test specimen final dimensions and state, **b)** specimen during processing

The laser beam was focused on the target with a focusing lens of 100 mm focal length and directed over the working area plane via Galvano mirrors with a high-speed reaching > 10000 mm/s maximum value. The irradiation pattern was in a one direction single pass with a variable overlap value along the laser beam direction and the constant overlapping ratio of 10% between two adjacent processed lines. The laser beam intensity in LSP should be high enough to cause plastic deformation in the metal surface. Here, the built pressure value (P) should be at least twice the yield strength value for the alloy. The sufficient value of laser beam intensity (I) can be calculated according to the following relation [20]:

$$P(GPa) = 0.01\,\frac{\sqrt{a}}{2a+3}\,\sqrt{Z}\sqrt{I} \quad \ldots\ldots\ldots\ldots(1)$$

where a is the fraction of absorbed energy that contributes to the plasma's thermal energy and Z is the lower shock impedance between the metal and the confined fluid. [21, 22].

The fatigue test was carried out with the alternating bending device (type HSM20) by applying a predefined load for each specimen group at the free end of the specimen. Each experiment was conducted at room temperature using a constant load with zero mean stress and a frequency of 25 Hz. The produced specimens through the LSP process were classified according to the set of utilized working parameters. Each set was subjected to six tests of different fatigue stresses 263, 235, 222, 217, 210 and 205 MPa. Eighteen specimens were distributed for each fatigue stress sub-group. This makes the overall number for the seventeen groups of working parameters is 306 specimens.

3. Design of Experiments

Design of experiments (DOE) is a method for planning, carrying out, analyzing and interpreting experiments in a systematic way. DOE employs statistical tools to analysis the effect of input variables and their interactions on a response or group of responses. This approach decreases the number of experiments required to develop an experimental model that can be used to investigate the effect of process factors and their interactions on the response [22, 23]. Manipulating of input variables at the same time is possible with DOE to identify the important interactions that may be not observed when applying experiments with one factor at a time method [24]. Response surface methodology (RSM) is a mathematical and statistical technique based on DOE can efficiently model and analyze any process in which the response affected by input variables [25]. RSM can predict the response at various process variables as well as optimize it through find the values of variables that produces the best desired condition for the response [26] .

Design-expert v13 software package was used in current study to perform DOE, analyses data, build RSM model and optimize the process through Box-Behnken design (BBD). Optimization was benefit for predicting the optimum process variables that yields best fatigue life. In RSM, the general second-order polynomial model was used as a functional link between the independent variables and the response surface [27]:

$$Y = b_o + \sum\nolimits_{i=1} b_{ii}\, x_i^2 + \sum_{i=1}^{n} . \sum_{j=i+1}^{n} b_{ij}\, x_i x_{j\,+\,e} \quad \ldots\ldots\ldots\ldots\ldots\ldots(2)$$

where Y is the response, the set *bo*, *bii* and *bij* are linear, quadratic and interaction regression coefficients, *xi* and *xj* are the independent variables and *e* is the experimental/residual error.

Design Expert ® V13 statistical software package from Stat-Ease Inc. was utilized to build the statistical model and analyze the obtained experimental data. BBD was used for three input independent variables namely the pulse repetition rate (PRR), laser spot size (ω) and scanning speed (v) on the dependent response fatigue life. The range of input variable was designed and defined for the software to suggest the number and set of input variable for each experiment. Table (3) lists the lower and higher range for each input variable and their corresponding coded levels. The experiments were carried out to obtain the response values which inserted into the software later.

Table (3) Input parameters ranges and their coded levels

Variable	**Actual values at coded levels**		
	-1	**0**	**+1**
PRR (kHz)	20.00	22.5	25.00
ω (mm)	0.02	0.03	0.04
v (mm/s)	200.00	350	500.00

4. Results and Discussion

4.1 Experimental Results

The fatigue life values representing the responses are expressed by the number of cycles (noc) for each applied stress. The extracted experimental results for noc were inserted into DOE to finish data insertion. The experimental design considered three levels, three independent input parameters (PRR, ω, and v), and seventeen experiments. Table (4) presents the average fatigue life value of three specimens for each set of parameters group subjected to different loads as well as the raw metal noc values.

Table 4: BBD for extraction the response values for fatigue life.

Experiment No.	**Parameters values (Coded values)**			**Responses: Average fatigue life (noc) × 10^4 (cycle)**					
	***PRR* (kHz)**	***ω* (mm)**	***v* (mm/s)**	**noc at 263 (Map)**	**noc at 235 (MPa)**	**noc at 222 (MPa)**	**noc at 217 (MPa)**	**noc at 210 (MPa)**	**noc at 205 (MPa)**
	Raw specimens (not processed)			4.273	9.229	10.749	12.286	15.077	18.508
1	22.5 (0)	0.03 (0)	350 (0)	5.636	9.633	18.468	28.078	38.794	46.812
2	22.5 (0)	0.03 (0)	350 (0)	6.052	13.098	20.233	30.226	43.900	57.098
3	25 (1)	0.04 (1)	350 (0)	4.701	10.717	20.381	30.267	41.874	57.619
4	25 (1)	0.03 (0)	500 (1)	8.568	15.770	21.818	30.688	43.413	51.920
5	25 (1)	0.03 (0)	200 (-1)	4.676	10.903	21.948	31.284	41.023	51.164
6	22.5 (0)	0.04 (1)	500 (1)	13.123	20.904	32.610	43.441	73.353	112.021
7	22.5 (0)	0.02 (-1)	500 (1)	3.760	9.598	19.013	24.047	30.297	38.351
8	20 (-1)	0.04 (1)	350 (0)	4.834	11.011	20.417	30.214	40.217	50.703
9	22.5 (0)	0.02 (-1)	200 (-1)	4.746	10.433	20.812	29.850	40.661	50.106
10	22.5 (0)	0.03 (0)	350 (0)	6.052	13.098	20.233	30.230	43.900	57.098
11	22.5 (0)	0.03 (0)	350 (0)	62.112	10.343	18.757	26.992	36.890	51.329
12	22.5(0)	0.03 (0)	350 (0)	5.120	11.250	13.601	22.551	31.489	50.226
13	20 (-1)	0.02 (-1)	350 (0)	4.378	9.569	20.191	30.144	31.727	54.378
14	20 (-1)	0.03 (0)	500(1)	4.046	10.253	19.050	23.986	34.063	44.319
15	20 (-1)	0.03 (0)	200 (-1)	4.691	11.914	22.453	29.870	40.263	49.000
16	22.5 (0)	0.04 (1)	200 (-1)	10.652	20.428	31.201	40.243	64.010	106.942
17	25 (1)	0.02 (-1)	350 (0)	4.378	9.569	20.191	30.144	31.723	54.378

Two of the applied experiments for different sets of input parameters show significant fatigue life: experiments 6 and 16. It could be deduced from both experiments the PRR of 22.5 and ω of 0.04 mm are the optimum operating conditions at the upper and lower scanning speed ω values of 200 mm/s and 500 mm/s. Compared with raw specimens, noc for these two sets of parameters recorded a percentage increase in fatigue life of 505.25% and 477.81% for experiments 6 and 16, respectively, as seen in figure (2).

The experimental data was represented on boxplot graphs to discover their variability or dispersion, outliers and symmetry. Boxplots graph in figure (3) show the impact of each input parameter at its three levels on data

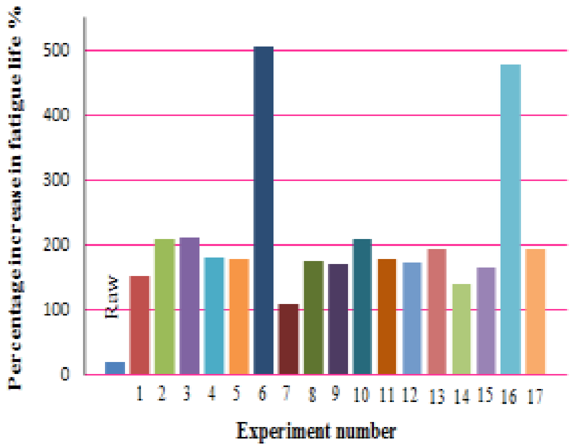

Figure (2): The percentage increase in fatigue life for the processed specimens at an applied stress of 205 MPa

characteristics and distribution. The high level of ω demonstrates more different amounts when compared with the other two parameters PRR and v, as seen in figure (3a). On the other hand, the other two levels of ω exhibit no effect of variability of the response and shorter whiskers. The more significant variability for noc data and wider whiskers can be observed at least for two levels of the v parameters as shown in figure (3b).

No outlier was observed where the whiskers length is shorter than the 1.5 times the interquartile range. The longer boxes of low and high levels for v indicates wider distribution, that is, more scattered data. Figure (3c) demonstrates less distribution and outlier data for the three levels of the parameters PRR. The median lines of the three boxplots overlap with their adjacent boxplots, and then there is likely to be no effective differences between the three levels.

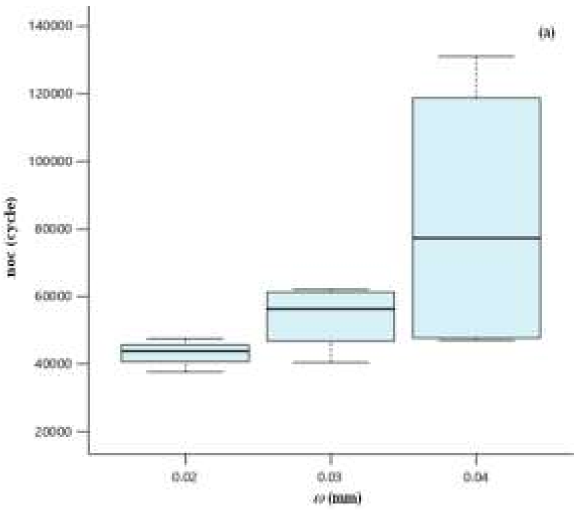

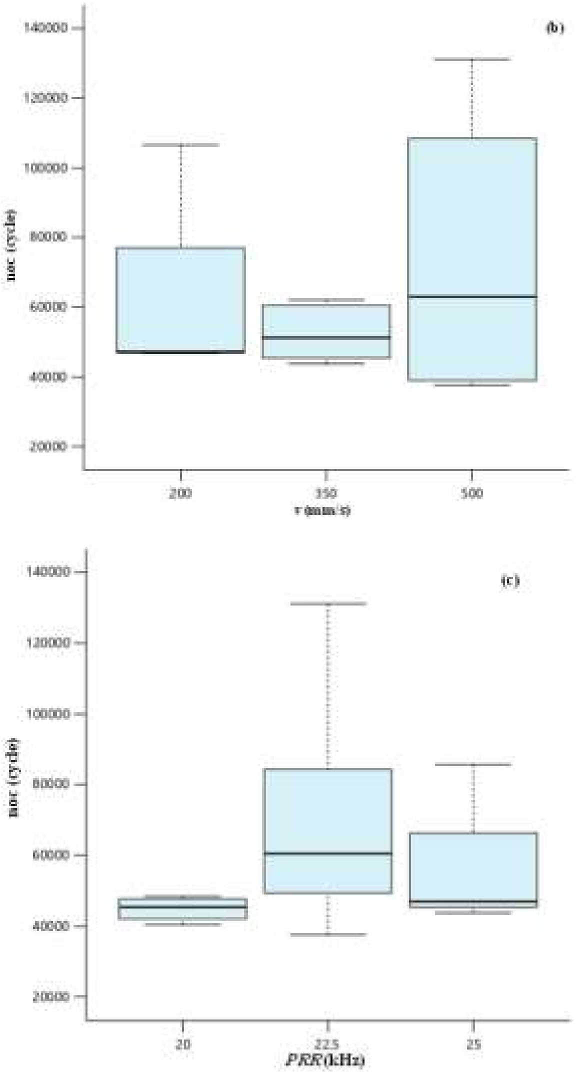

Figure (3): Boxplots representation for the distribution of data at three levels for each input parameter: a) spot size *ω*, b) scanning speed *v* and c) pulse repetition rate *PRR*.

For all three graphs, it can be seen that most of the boxplots for the three parameters are skewed (asymmetric) and don't follow a normal distribution.

4.2 Model Analysis

BBD based on RSM with three independent parameters as input variables and their interactions was utilized to develop the response surface models and their interactions. The response surface was tailored to fit the experimental results obtained from the executed experiments. The models predict found the responses noc at the various combination of working parameters PRR, ω and v. The adequate model without aliased terms after eliminating some combinations of nominal and weird words.

Axiomatically, all of the responses for noc at different applied stresses show different values but approximately the same behavior when modeled. Thus, one of these models will be presented in the current section, reflecting the general conduct of fatigue lives at different applied stresses. The following analysis for the obtained model and optimization is related to the response at the applied pressure of 205 MPa. It is worth to mention the quadratic model was failed to represent the significance of the build model and its related input parameters. This may be related to the nature of obtained data in term of two significant results among almost the same level of data for the others. The cubic model handles the situation after elimination some diagnosed aliased combinations of input parameters. The mathematical model that benefits for predicting the response noc as a function of a set of the input parameters PRR, ω and v is as follow:

$$noc = -2.13 \times 10^{6} + 1.52 \times 10^{5}\, PRR + 7.72 \times 10^{6}\, \omega + 5.05 \times 10^{3}\, v - 114.11\, PRR.v - 89.3 \times 10^{3}\, \omega.v - 3.05 \times 10^{3}\, PRR^{2} + 1.7 \times 10^{8}\, \omega^{2} - 8.76\, v^{2} + 0.206\, PRR.v^{2} - 3 \times 10^{5}\, \omega^{2}.v + 161\, \omega.v^{2} \dots\dots\dots..(3)$$

One-way Analysis of variance test (ANOVA) was applied for the reduced cubic model given in table (5) to test the null hypothesis and analyze the statistically significant differences between the means of variables.

Table (5): ANOVA test for noc at applied stress of 205 MPa.

Source	Sum of Squares	df	Mean Square	*F*-value	*p*-value	
Model	1.013×10^{10}	11	9.207×10^{8}	58.36	0.0001	significant
PRR	4.469×10^{5}	1	4.469×10^{5}	0.0283	0.8729	
ω	1.514×10^{7}	1	1.514×10^{7}	0.9593	0.3723	
v	2.637×10^{8}	1	2.637×10^{8}	16.71	0.0095	
PRR . ω	5.146×10^{8}	1	5.146×10^{8}	32.62	0.0023	
ω . v	2.984×10^{8}	1	2.984×10^{8}	18.91	0.0074	
PRR^2	1.533×10^{9}	1	1.533×10^{9}	97.16	0.0002	
ω^2	1.870×10^{8}	1	1.870×10^{8}	11.85	0.0184	
v^2	1.063×10^{9}	1	1.063×10^{9}	67.36	0.0004	
PRR . v	2.691×10^{8}	1	2.691×10^{8}	17.06	0.0091	
$\omega.v^2$	3.896×10^{7}	1	3.896×10^{7}	2.47	0.1769	
$\omega^2 v$	2.624×10^{9}	1	2.624×10^{9}	166.3	<0.0001	
Residual	7.889×10^{7}	5	1.578×10^{7}			
Lack of fit	4.469×10^{5}	1	4.496×10^{5}	0.0228	0.8873	not significant
Pure error	7.844×10^{7}	4	1.861×10^{7}			
Cor Total	1.021×10^{10}	16				

The F-value of 58.36 for the developed model implies the model is significant. There is only a 0.01%chance that this large F-value occur due to noise. The observed significant p-value of 0.0001 makes both terms of the model are significant. Among the duration of three input parameters, the v is found effective for both F-value and p-value. Likewise, the combinations of input parameters were found significant except the term ω.v2 was insignificant where the p-values greater than 0.10. The Lack of Fit F-value of 0.0228 implies that the Lack of Fit is unimportant relative to the pure error. There is an 88.73% chance that a Lack of Fit F-value this large could occur due to noise. Non-significant lack of fit is a good value to the model fit.

The fit statistics reveal an R^2 value of 0.9923 close to unity and has good agreement with an adjusted R^2 value of 0.9753. The Adequate Precision (Adeq) value measures the signal to noise ratio. The model shows an Adeq Precision value of 28.049, where a ratio greater than 4 is desirable. This can give an indication that the model could be used to navigate the design space. Figure (4) shows the distribution of the actual data points of the response depicted by the experiments on each run versus the predicted values evaluated by the model. It can be seen data points distributed along the 45o line indicating good agreement of experimental and expected results by the model.

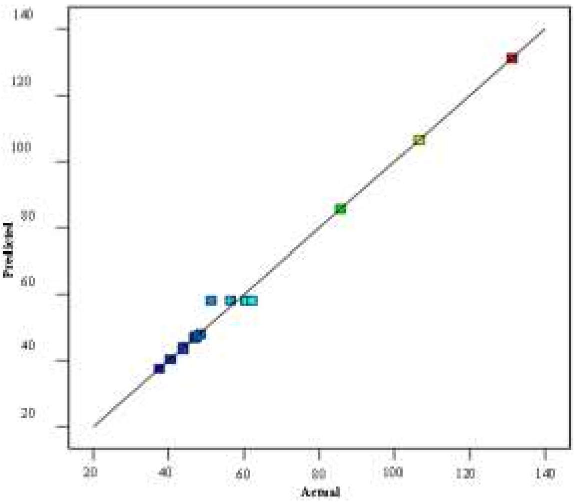

Figure (4): Plot of predicted vs. actual data of the modified model in noc.

According to the experimental results and statistical analysis, RSM plots the three-dimensional graphs for the response noc as a function of two or more input parameters. Figure 5 defines in 3D graph and contour plot the values of noc at a combination of two input parameters for a certain fixed value for the third one. The effect of PRR and ω for a fixed value of v 200 mm/s is illustrated in Figure 5a. The impact of PRR and ω on the fatigue life indicated that noc was maximum at ω=0.04 mm and PRR= 22.5 kHz. It is clear that noc has increased with increasing ω and PRR towards the maximum and moderate values respectively. For the same graph, if v switched to average values of 350 mm/s, the response surface decreases before increasing to the maximum at v=500 mm/s. High scanning speed results in a high cooling rate and low interaction time with the target, resulting in less roughness and high hardness.

However, when the speed declines, the interaction time increases, and the cooling rate decreases, resulting in increased surface roughness accompanied by lower hardness [28].

The effect of PRR and v on the response, at fixed value of ω=0.03 mm, is depicted in Figure 5b. Moving PRR from the moderate to high values gives higher values of noc at the terminals of v 200 mm/s and 500 mm/s. Changing the value of ω to the minimum lowers the response surface down and vice versa. The induced compressive residual stresses at the surface obviously increase for a certain depth with increasing ω [29].

The effect of ω and v on the noc when the PRR at 22 kHz is shown in figure (5c). The noc shows two significant peaks when ω= 0.04 mm and v is at the maximum or minimum values. Lowering the value of PRR lowers the response surface and keeps the same pattern. This may be related to plasma formation rule related to the laser intensities value. At low intensity of less than 1 GW/cm2 LSP is not verified. At moderate range of 1 GW/cm2 to 7 GW/cm2, the plasma pressure reaches its maximum limit. When the intensity increases above 7 GW/cm2, plasma saturation and light shielding occur [30].

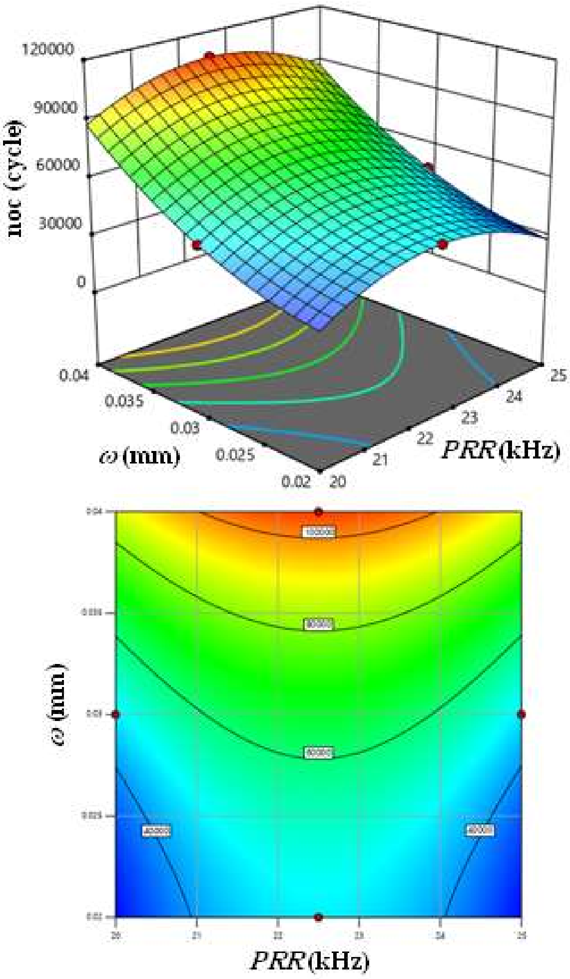

a) *PRR* vs. ω at v=200 mm/s.

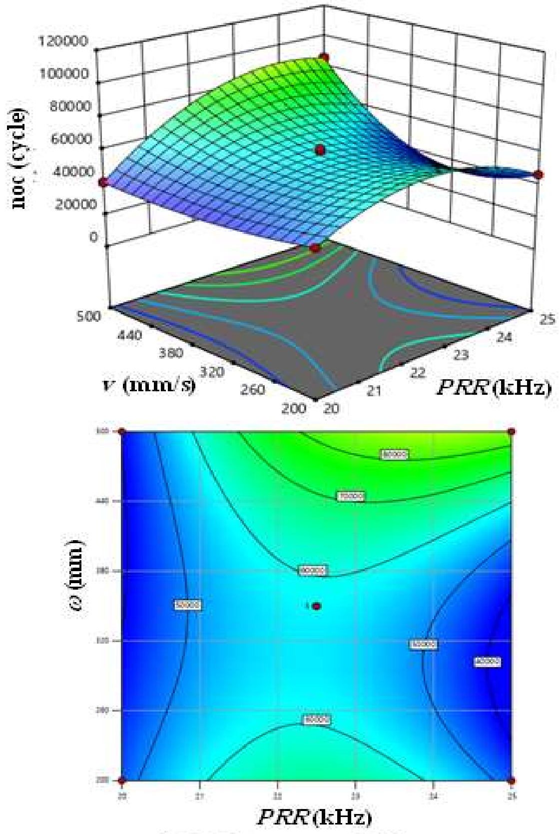

b) PRR vs. v at ω=0.03 mm.

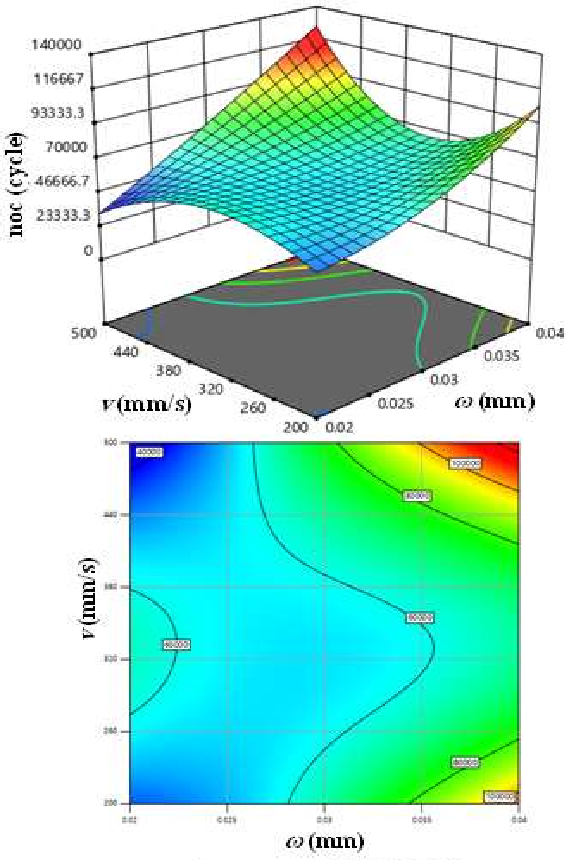

c) ω vs. v at PRR=22 kHz.

Figure (5): 3D response plots for noc.

4.3 Optimization

To enhance the fatigue life efficiency, the optimum suggested operating parameters were introduced by the model as shown in Figure 6. In the criteria of optimization, three optimized conditions were extracted out by setting three different criteria:

a) Maximum response could be attained for PRR range of 22 - 25 kHz and ω range of 0.035 – 0.04 mm when the experiment operates at v of 500 mm/s as shown in Figure 6a.

b) Figure 6b shows it is possible maximize the response through two conditions at constant value of ω equals to 0.04 mm and PRR range of 21 – 25 kHz. The highest one is when v equals 500 mm/s and the lowest one at v equals to 200 mm/s .

c) To maximize the response Figure 6c reveals two sets optimized conditions at PRR of 25 kHz. The largest one when the v equals 500 mm/s and ω=0.04 mm and the smaller one when the v equals 200 mm/s for same value of ω.

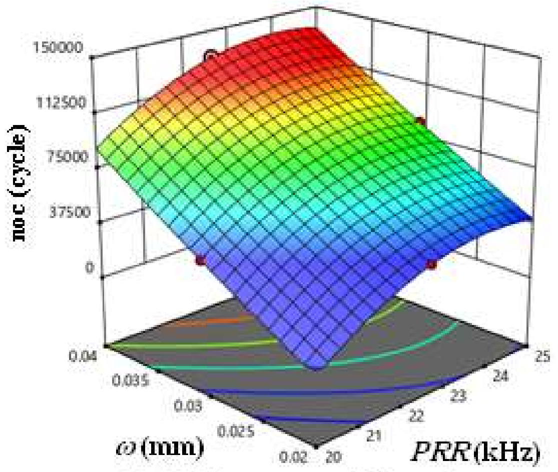

(a) PRR vs. ω at v=500 mm/s.

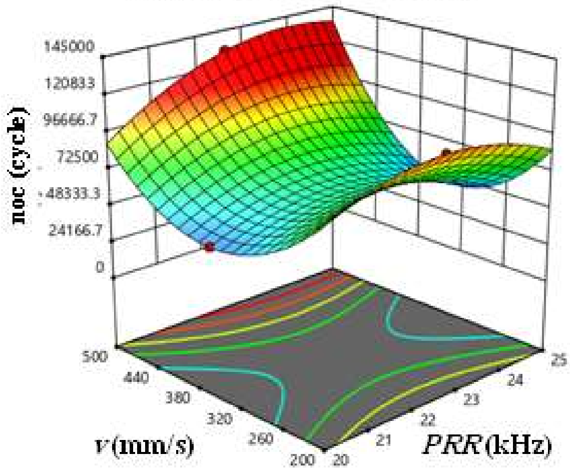

(b) PRR vs. v at ω=0.04

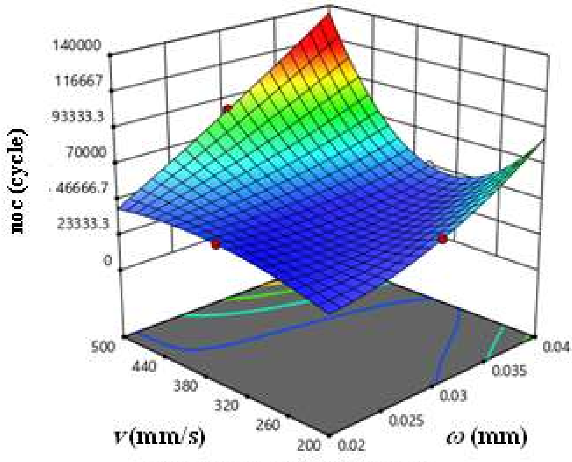

(c) v vs. ω at PRR=25 kHz.

Figure (6): 3D response plots for desired response values.

5. Conclusions

LSP treatment for Aluminum 6061-T6 thin sheets, reveals a significant improvement in fatigue life under cyclic loading. The following concluded remarks are extracted from the current study:

1. Processing samples with LSP showed a variety range of improvement for the fatigue life with respect to the untreated samples. At two sets of input parameters, the results were highly considerable. When the PRR equals 22.5 kHz and ω was 0.04 mm the percentage increase in fatigue life was 505.25% and 477.81% at the minimum and maximum scanning speeds 200 mm/s and 500 mm/s respectively.
2. The experiments results show that both v followed by the ω are the most effective parameter reveal a wider variance in the fatigue life values represented by noc.
3. The quadratic model failed to explore the design space due to the few numbers of significant results (only two) which may be considered as noise. Therefore, experimental modeling switched toward the cubic model after terminating the aliased combination of parameters.
4. The presented model reveals a variety of conditions for improving the fatigue life results such as: when applying the v at 500 mm/sec for PRR range of 22 – 25 kHz and ω range of 0.035 – 0.04 mm. Another optimization set when the scanning speed v at its maximum or minimum limits at ω of 0.04 mm and PRR from 21 to 25 kHz.

6. Acknowledgment

The authors are grateful for the support provided by the Institute of Laser for Postgraduate Studies at University of Baghdad and Mechatronics Engineering Department, Al-Khwarizmi College of Engineering at University of Baghdad.

7. References

[1] R. I. Rodriguez, J. B. Jordon, P. G. Allison, T. Rushing, and L. Garcia, "Microstructure and mechanical properties of dissimilar friction stir welding of 6061-to-7050 aluminum alloys," Materials & Design, vol. 83. Elsevier BV, pp. 60–65, Oct. 2015. doi: 10.1016 /j.matdes.2015.05.074.

[2]S. Malopheyev, I. Vysotskiy, V. Kulitskiy, S. Mironov, and R. Kaibyshev, "Optimization of processing- microstructure- properties relationship in friction-stir welded 6061-T6 aluminum alloy," Materials Science and Engineering: A, vol. 662. Elsevier BV, pp. 136–143, Apr. 2016. doi: 10.1016 /j.msea. 2016.03.063.

[3] H. Hao, D. Ye, and C. Chen, "Strain ratio effects on low-cycle fatigue behavior and deformation microstructure of 2124-T851 aluminum alloy," Materials Science and Engineering: A, vol. 605. Elsevier BV, pp. 151–159, May 2014. doi: 10.1016/j.msea. 2014.03.040.

[4] J. P. Hirth, "Effects of hydrogen on the properties of iron and steel," Metallurgical Transactions A, vol. 11, no. 6. Springer Science and Business Media LLC, pp. 861–890, Jun. 1980. doi: 10.1007/bf02654700.

[5] C. Correa et al., "Random-type scanning patterns in laser shock peening without absorbing coating in 2024-T351 Al alloy: A solution to reduce residual stress anisotropy," Optics & Laser Technology, vol. 73. Elsevier BV, pp. 179–187, Oct. 2015. doi: 10.1016/j.optlastec.2015.04.027.

[6] U. Trdan, M. Skarba, and J. Grum, "Laser shock peening effect on the dislocation transitions and grain refinement of Al–Mg–Si alloy," Materials Characterization, vol. 97. Elsevier BV, pp. 57–68, Nov. 2014. doi: 10.1016/j.matchar.2014.08.020 .

[7] C. Montross, "Laser shock processing and its effects on microstructure and properties of metal alloys: a review," International Journal of

Fatigue, vol. 24, no. 10. Elsevier BV, pp. 1021–1036, Oct. 2002. doi: 10.1016/s0142-1123(02)00022-1 .

[8] R. Fabbro, P. Peyre, L. Berthe, and X. Scherpereel, “Physics and applications of laser-shock processing,” Journal of Laser Applications, vol. 10, no. 6. Laser Institute of America, pp. 265–279, Dec. 1998. doi: 10.2351/1.521861 .

[9] W. Guo et al., “Laser shock peening of laser additive manufactured Ti6Al4V titanium alloy,” Surface and Coatings Technology, vol. 349. Elsevier BV, pp. 503–510, Sep. 2018. doi: 10.1016/j.surfcoat.2018.06.020 .

[10]A. Issa, F. I. Hussein Al-Najjar, A. Al-Hamaoy, and B. G. Rasheed, “Physical principles of laser–material interaction regimes for laser machining processes,” Laser Micro- and Nano-Scale Processing. IOP Publishing, Aug. 2021. doi: 10.1088/978-0-7503-1683-5ch3.

[11]F. I. Hussein Al-Najjar, A. Al-Hamaoy, B. G. Rasheed, and A. Issa, “Effective working parameters of laser micro-/nano-machining,” Laser Micro- and Nano-Scale Processing. IOP Publishing, Aug. 2021. doi: 10.1088/978-0-7503-1683-5ch4.

[12] J. Zhao et al., “A rapid one-step nanosecond laser process for fabrication of super-hydrophilic aluminum surface,” Optics & Laser Technology, vol. 117. Elsevier BV, pp. 134–141, Sep. 2019. doi: 10.1016/j.optlastec.2019.04.015 .

[13] C.-Y. Shih et al., “Two mechanisms of nanoparticle generation in picosecond laser ablation in liquids: the origin of the bimodal size distribution,” Nanoscale, vol. 10, no. 15. Royal Society of Chemistry (RSC), pp. 6900–6910, 2018. doi: 10.1039/c7nr08614h.

[14] C. Rubio-González et al., “Effect of laser shock processing on fatigue crack growth and fracture toughness of 6061-T6 aluminum alloy,” Materials Science and Engineering: A, vol. 386, no. 1–2. Elsevier BV, pp. 291–295, Nov. 2004. doi: 10.1016/j.msea.2004.07.025.

[15]A. R. Alhamaoy, G. Sh. Sadiq, F. I. Hussein, and S. N. Ali, “The Cyclic Fatigue Behavior for 6061-T6 Al Alloy Shafts Processed by Laser Shock Peening,” Materials Science Forum, vol. 1002. Trans Tech Publications, Ltd., pp. 21–32, Jul. 2020. doi: 10.4028/www.scientific.net/msf.1002.21.

[16] X. Q. Zhang et al., “Investigation on effect of laser shock processing on fatigue crack initiation and its growth in aluminum alloy plate,” Materials & Design (1980-2015), vol. 65. Elsevier BV, pp. 425–431, Jan. 2015. doi: 10.1016/j.matdes.2014.09.001.

[17] S. Huang et al., “Effects of laser energy on fatigue crack growth properties of 6061-T6 aluminum alloy subjected to multiple laser peening,” Engineering Fracture Mechanics, vol. 99. Elsevier BV, pp. 87–100, Feb. 2013. doi: 10.1016/j.engfracmech.2013.01.011.

[18] Q. LIU, C. H. YANG, K. DING, S. A. BARTER, and L. YE, “The effect of laser power density on the fatigue life of laser-shock-peened 7050 aluminium alloy,” Fatigue & Fracture of Engineering Materials and Structures, vol. 30, no. 11. Wiley, pp. 1110–1124, Nov. 2007. doi: 10.1111/j.1460-2695.2007.01180.x .

[19] Standard Test Methods for Tension Testing of Metallic Materials

[20] T. Takata, M. Enoki, P. Chivavibul, A. Matsui, and Y. Kobayashi, “Effect of Confinement Layer on Laser Ablation and Cavitation Bubble during Laser Shock Peening,” MATERIALS TRANSACTIONS, vol. 57, no. 10. Japan Institute of Metals, pp. 1776–1783,2016.doi:10.2320/matertrans.m2016150.

[21] D. Devaux, R. Fabbro, L. Tollier, and E. Bartnicki, “Generation of shock waves by laser- induced plasma in confined geometry,” Journal of Applied Physics, vol. 74, no. 4. AIP Publishing, pp. 2268–2273, Aug. 15, 1993. doi: 10.1063/1.354710.

[22] P. K. Park, D. H. Cho, E. Y. Kim, and K. H. Chu, “Optimization of carotenoid production by Rhodotorula glutinis using statistical experimental design,” World Journal of Microbiology and Biotechnology, vol. 21, no. 4. Springer Science and Business Media LLC, pp. 429–434, Jun. 2005. doi: 10.1007/s11274-004-1891-3.

[23] L. M. Collins, J. J. Dziak, and R. Li, “Design of experiments with multiple independent variables: A resource management perspective on complete and reduced factorial designs.,” Psychological Methods, vol. 14, no. 3. American Psychological Association (APA), pp. 202–224, 2009. doi: 10.1037/a0015826.

[24] B. Durakovic, “Design of experiments application, concepts, examples: State of the art,” Periodicals of Engineering and Natural Sciences (PEN), vol. 5, no. 3. International University of Sarajevo, Dec. 28, 2017. doi: 10.21533/pen.v5i3.145.

[25]M. Kumari and S. K. Gupta, “Response surface methodological (RSM) approach for optimizing the removal of trihalomethanes (THMs) and its precursor’s by surfactant modified magnetic nanoadsorbents (sMNP) - An endeavor to diminish probable cancer risk,” Scientific Reports, vol. 9, no. 1. Springer Science and Business Media LLC, Dec. 2019. doi: 10.1038/s41598-019-54902-8.

[26] K. A. Mohamad Said and M. A. Mohamed Amin, “Overview on the Response Surface Methodology (RSM) in Extraction Processes,” Journal of Applied Science & Process Engineering, vol. 2, no. 1. UNIMAS Publisher, May 12, 2016. doi: 10.33736/jaspe.161.2015.

[27] S. L. C. Ferreira et al., “Box-Behnken design: An alternative for the optimization of analytical methods,” Analytica Chimica Acta, vol. 597, no. 2. Elsevier BV, pp. 179–186, Aug. 2007. doi: 10.1016/j.aca.2007.07.011 .

[28] N. R. Dhar and M. Kamruzzaman, “Cutting temperature, tool wear, surface roughness and dimensional deviation in turning AISI-4037 steel under cryogenic condition,” International Journal of Machine Tools and Manufacture, vol. 47, no. 5. Elsevier BV, pp. 754–759, Apr. 2007. doi: 10.1016/j.ijmachtools.2006.09.018.

[29] Y. Liu, D. Xu, M. Agmell, A. Ahadi, J.-E. Stahl, and J. Zhou, “Investigation on residual stress evolution in nickel-based alloy affected by multiple cutting operations,” Journal of Manufacturing Processes, vol. 68. Elsevier BV, pp. 818–833, Aug. 2021. doi: 10.1016/j.jmapro.2021.06.015.

[30] C. Montross, “Laser shock processing and its effects on microstructure and properties of metal alloys: a review,” International Journal of Fatigue, vol. 24, no. 10. Elsevier BV, pp. 1021–1036, Oct. 2002. doi: 10.1016/s0142-1123(02)00022-1.

تحسين معلمات عمر الكلال لألواح الألومنيوم الرقيقة نوع T6-6061 المُعالجة بالسفع بالليزر فائق السرعة

علي محمد خضير[1] , فرات ابراهيم حسين[2]

[1] معهد الليزر للدراسات العليا/جامعة بغداد
[2] قسم هندسة الميكاترونكس/كلية الهندسة الخوارزمي/جامعة بغداد

الخلاصة: تتميز سبائك الألومنيوم نوع T6-6061 بخصائصها الممتازة ومزيا سهولة المعالجة التي تجعلها مثالية لأنواع مختلفة من التطبيقات الصناعية. تظهر سبائك الألومنيوم عند التحميل الدوري عمرا للكلال أقل من سبائك الصلب ذات الخواص الميكانيكية المماثلة. في الدراسة الحالية تم استخدام ليزر الألياف نوع النانوثانية بقدرة عالية تصل إلى 100 واط لتطبيق عملية سفع باالليزر على صفائح الألومنيوم الرقيقة لاضافة اجهادات داخلية من أجل تعزيز وزيادة عمر الفشل الكلالي تحت التحميل الدوري. في هذه الدراسة تم استخدام تصميم Box-Behnken (BBD) بناءً على اسلوب تصميم التجارب (DOE) لتحليل بيانات التصميم التجريبي وبناء النماذج المبنية على نتائج المختبر وتحسينها. تم التحقيق في تأثير معلمات التشغيل وهي حجم البقعة (ω) وسرعة المسح (v) ومعدل تكرار النبضات (PRR) بثلاثة مستويات مختلفة القيمة على عمر الكلال المعبر عنه بعدد الدورات اللازمة لحدوث الفشل (noc). أظهرت النتائج زيادة حصرية في عمر الكلال بنسب مئوية قدرها 505.25٪ و 477.81٪ عند $\omega = 0.04$mm و PRR = 22.5kHz لسرعتي المسح 200 mm/s و 500 mm/s على التوالي. تم الحصول من النموذج التطبيقي المبنى عدة مقترحات لمعلمات الادخال التي من الممكن ان تحسن المخرجات و أداء العملية متمثلة بعمر كلال أعلى.

Iraqi J. Laser, issue 2, vol., 20, pp. 18-23 (2021)

IRAQI
JOURNAL
OF
LASER

The influence of no-core fibre length on the sensitivity Optical fibre Humidity sensor

Suroor L. khashin[1,*], **Hanan J. Taher**[1]

*Corresponding author: Suroorlazem95@gmail.com

1. Institute of Laser for Postgraduate Studies, University of Baghdad, Iraq, Baghdad, Iraq.

(Received 14/10/2021; accepted 29/12/2021)

Abstract : Reflection optical fibre Humidity sensor is presented in this work, which is based on no core fibre prepared by splicing a segment of no core fibre (NCF) at different lengths 1-6 cm with fixed diameter 125 µm and a single mode fibre (SMF). The range of humidity inside the chamber is controlled from 30% to 90% RH at temperature ~ **30 °C**. The experimental result shows that the resonant wavelength dip shift decreases linearly with an increment of RH% and the sensitivity of the sensor increased linearly with an increasing in the length of NCF. However, a high sensitivity 716.07pm/RH% is obtained at length 5cm with good stability and reputability. Furthermore, the sensor is shifted towered a short wavelength (Blue shift).

Keywords: Optical Fibre sensor, RH sensor, No-core fibre, Circulator, Multimode Interference

1. Introduction

Relative humidity (RH) can be defined as the ratio of moisture content in the air to the total moisture (saturated) level that the air can carry at the same temperature [1]. Measuring RH is considered a significant importance parameter in a wide range of applications, such as bacterial growth, process control, product quality, food and beverage processing, automotive, and meteorological industries [2, 3]. Recently, optical fibre sensors have attracted extensive attentions in many fields of sensing, such as refractive index (RI) sensor [4], pH sensor [5], strain sensor [6], temperature sensor [7], curvature sensor [8], and humidity sensor [9]. Optical fibre humidity sensors have distinctive features such as being lightweight, small size, low cost, and having low attenuation and immunity to electromagnetic interference, making them an ideal sensing medium for several real-world applications [10, 11].

By measuring the changes in polarization, wavelength, phase and intensity of light passing through the sensing region, there are four types of optical fibre interferometer, namely Fabry-perot, Sagnac, Michelson, and Mach Zehnder interferometer. In 2016, Li-Peng Sun et. al. Proposed an optical fibre RH sensor based on a microfiber Sagnac loop interferometer, with a range of RH from 30%RH to 90%RH and sensitivity up to ~201.25 pm/%RH [12]. In 2021, CHENG ZHOU et. al., Proposed RH sensor that is based on sensitivity amplification and a reduction mechanism Internal–external Fabry–Perot cavity (IEFPC) and a range of humidity 40%–92% RH and sensitivity up to 715 pm/% RH [13]. In 2019, Piaopiao Wang et. al., Proposed a Methylcellulose (MC) film-coated RH sensor that is based on Michelson interferometer, with 30%-85% RH and sensitivity 133 pm/%RH [14]. In 2016, Suaad Sahib Hindal, Hanan J. Taher proposed an optical fibre RH sensor based on Photonic Crystal Fibre Interferometers (PCFIs) based on Mach Zehnder. The range of humidity in their proposal was 27% RH to 85% RH with a sensitivity of 5.86 pm / %RH [15]. In optical fibre humidity sensors (OFHS) based on MZI, the light is guided and modulated by a no core fibre and the surrounding medium, then is collected by a detector. As the RH is a function of the refractive index (RI), so any change in the RH effect on the transmitted or reflected light that passes through or interacts with the medium.

In this paper, a reflection optical fibre sensor is proposed and manufactured to be used to measure RH. The structure of the proposed sensor is easy, low cost and high sensitivity.

2. Experimental Work

2.1 Sensing Principle

Figure (1) shows the diagram of the proposed RH that is based on NCF (FG125LA from Thorlabs). It has a cladding with a diameter 125 μm, and SMF (corning SMF-28). The section of the NCF and SMF was spliced using a fusion splicer (Fujikura FSM-60S) [16]. The structure was made with a flat end of NCF using a cleaver. Different lengths of NCF were spliced with a single mode fiber. As shown in figure (1), the sensing beam is exposed to the surrounding medium while the reference beam is kept secluded. Any change in the surrounding medium will have an effect on the sensing beam, which induces phase difference. This phase shift generates a constructive or destructive interference pattern. As the light guided from SMF to the NCFs, the high order modes are excited and propagated within the NCF. These excited modes interfere with one another as they propagate along NCF length, giving rise to a multi-mode interference (MMI).

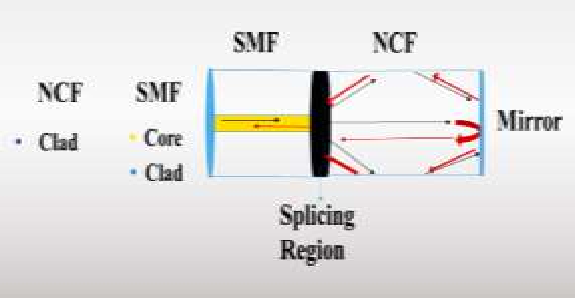

Figure (1): The structure of no core fiber (SNCF)

The reflected wavelength can calculate according to equation (1) [17]:

$$\lambda_{\circ} = \mathrm{p}\left(\frac{\mathrm{n}D^{2}}{2L}\right) \ldots\ldots\ldots\ldots\ldots\ldots\ldots\ldots\ldots\ldots\ldots\ldots\ldots (1)$$

where, $\lambda_{\circ}$ is the peak wavelength, n is the refractive index of the NCF, L is the length of the NCF, D is the diameter of the NCF, and p self-image, which is an integer number. When the light travel distance L over the NCF, a part of the light will escape as losses while a part of the light will collide at the end face of the fiber (mirror), then it reverses and travels a distance of 2L before coupling again at the SMF [18]. For different lengths, the self-image is formed when the modes travel along the NCFs, because of MMI effects. The initial mode is refocused at the length of the NCF.

2.2 Experimental set-up

Figure (2) shows the SNCF configuration. The system consists of a broadband source (BBS) with range 1450-1650nm (model: SLD1550S-A1 from Thorlabs) and circulator that contains three ports one of them is connected to BBS, and the second part is contacted to the optical spectrum analyzer OSA(YOKOKAWA, Ando AQ6370) with 0.02 nm resolution and the third port is connected to SNCF Humidity sensor.

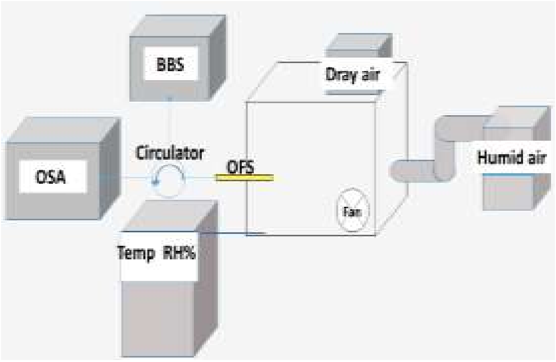

Figure (1): The experimental setup of the RH sensor.

SNCF is placed inside the chamber at different lengths of the NCF (1-6 cm). The chamber is placed in a plastic box that contains a small hole to allow the OFS entry inside the chamber. The chamber consists of three fans; one of these fans allows wet air to spread into the chamber while the other fans expel the air outside the chamber. An electronic RH meter is connected to the chamber to control the RH changes, in which the RH is slowly increased by 10% steps in the range 30 % - 90 % RH at approximately constant temperature of ~ 30 °C.

3. Results and discussion

In this work, OFHS has prepared by using different lengths of NCFs with diameter 125 μm. The structure is placed inside the chamber. At each RH, the reflection spectrum is measured after stabilizing for 10 seconds. It has been observed that the sensitivity is increased as the length of NCF is increased. Moreover, as the humidity increased the reflection spectrum shifted to a shorter wavelength (blue shift) where shown in figures (3-8).

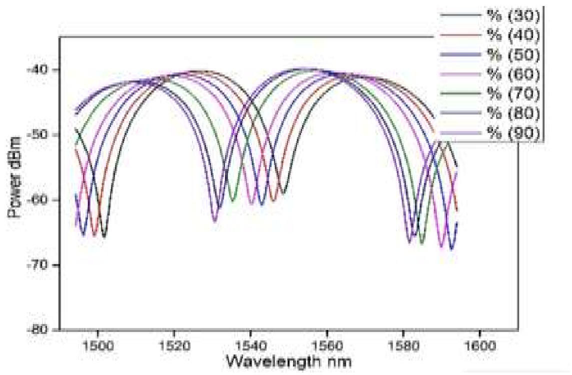

Figure (3): Reflection spectrum of NCFS for length 1 cm and diameter 125 μm.

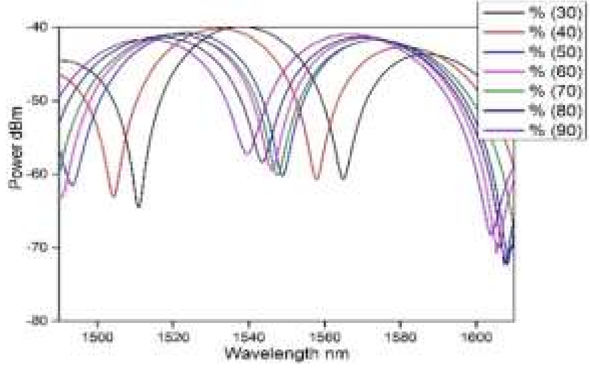

Figure (4): Reflection spectrum of NCFS for length 2 cm and diameter 125 μm.

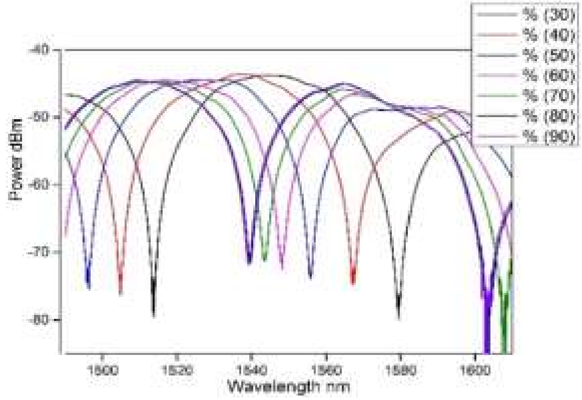

Figure (5): Reflection spectrum of NCFS for length 3 cm and diameter 125 μm.

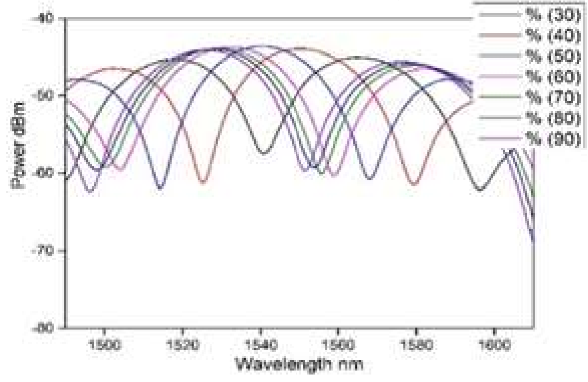

Figure (6): Reflection spectrum of NCFS for length 4 cm and diameter 125 μm.

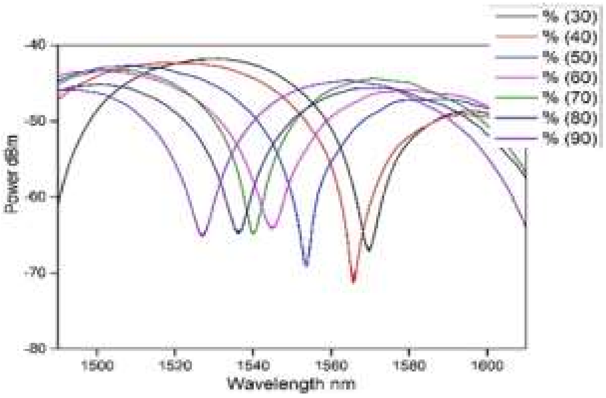

Figure (7): Reflection spectrum of NCFS for length 5 cm and diameter 125 μm.

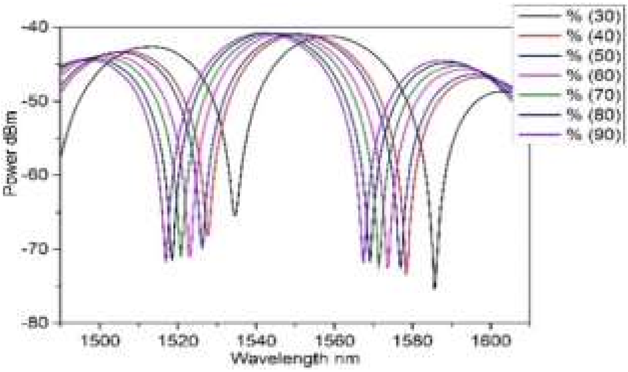

Figure (8): Reflection spectrum of NCFS for length 6 cm and diameter 125 μm.

Is shown in figures (9-14), the relation between linear fitting and RH% with rang 30%-90%. Any change in the length will have an effect on the sensitivity. When the length increases, an increase in the sensitivity is expected. For all lengths of NCFs, wavelength shift is approximately linear with an increase of relative humidity.

Table (1): lengths of NCFs with relative humidity

Length in cm	Sensitivity in pm/RH%
1	322.1
2	358.7
3	588.5
4	703.5
5	716.07
6	272.1

All lengths are shifted towered a short wavelength (blue shift). The highest sensitivity is reported as shown in figure (13), where the sensitivity was 716.07pm/RH% which was achieved at length 5 cm of NCF that reveals a high wavelength shift causing a higher sensitivity for RH sensor. All lengths of NCFs were prepared without dip coats and they were uncoated.

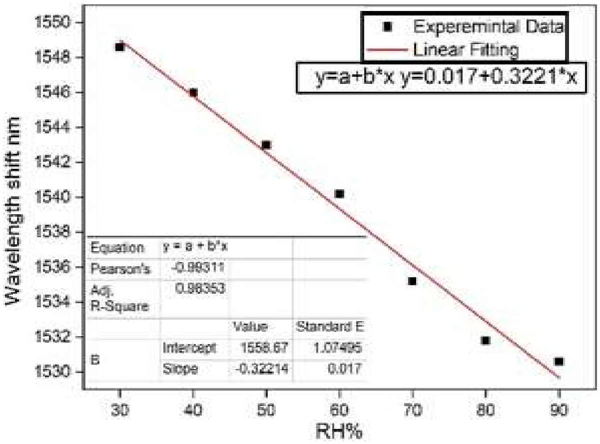

Figure (9): Linear fitting of NCFS for length 1 cm against RH% with sensitivity 322.1 pm/RH%.

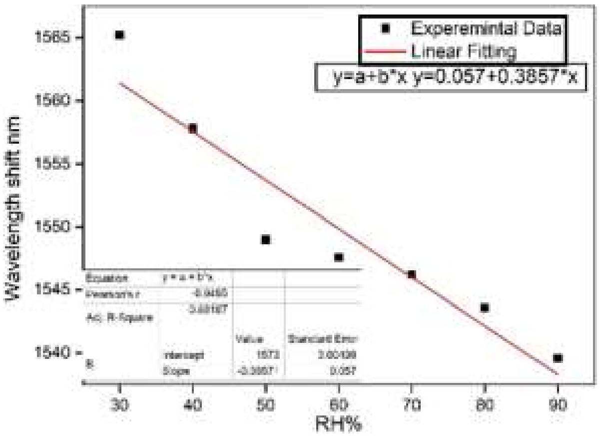

Figure (10): Linear fitting of NCFS for length 2 cm against RH% with sensitivity 385.7pm/RH%.

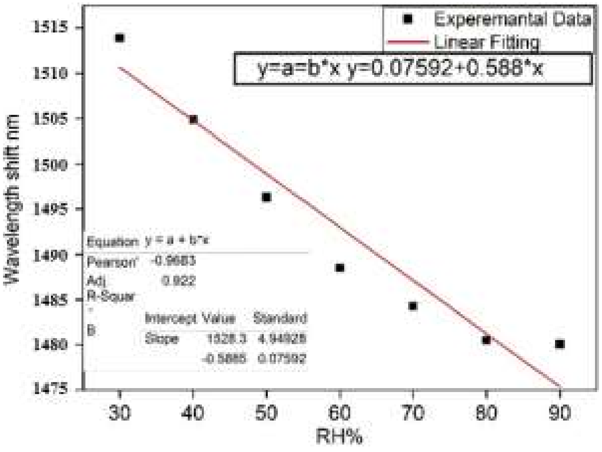

Figure (11): Linear fitting of NCFS for length 3 cm against RH% with sensitivity 588.5 pm/RH%.

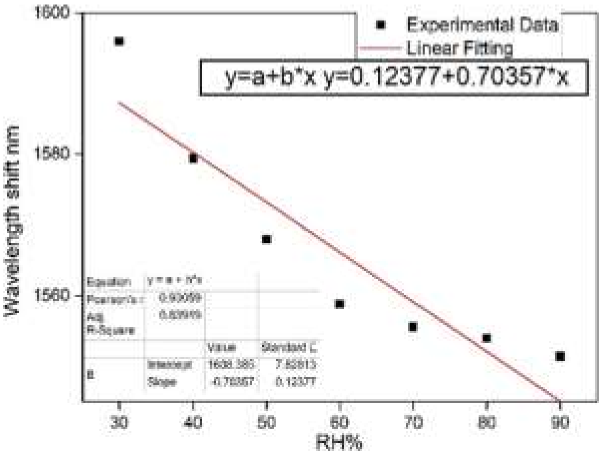

Figure (12): Linear fitting of NCFS for length 4 cm against RH% with sensitivity 703.5pm/RH%.

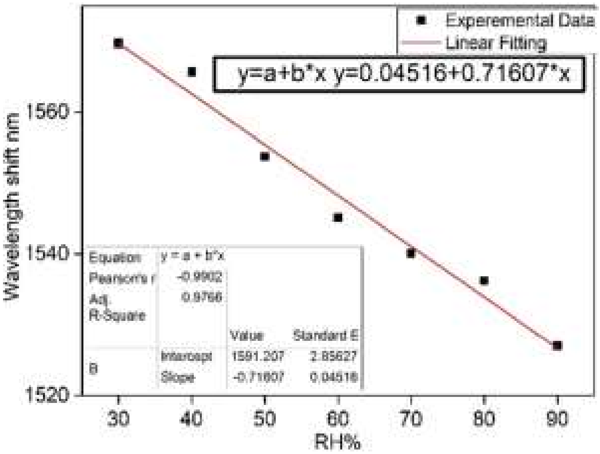

Figure (13): Linear fitting of NCFS for length 5cm against RH% with sensitivity 716.07 pm/RH%.

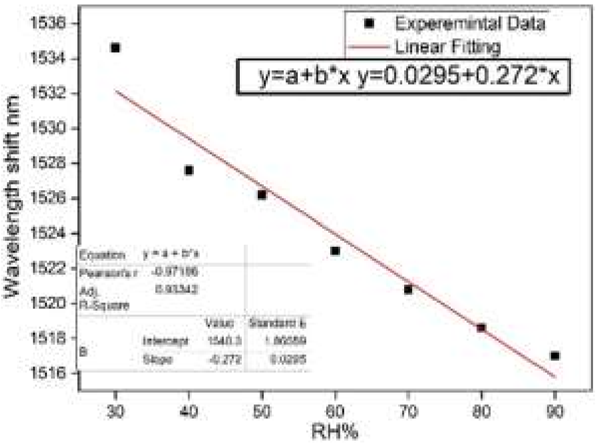

Figure (14): Linear fitting of NCFS for length 6 cm against RH% with sensitivity 272.1pm/RH%.

Figure (15), shows the relation between the sensitivity and the length of the NCF. As the length increases, the sensitivity is increased. The reason for this behavior can be interpreted as follows: when the effective area of the lengths increases and the interaction between the water vapor and the cladding modes occurs that leads to getting a small phase shift between the interference modes. For a longer wavelength of 6 cm, the sensitivity will be decreased as at length 6 cm the interference will be diminution (distractive interference) which leads to an increase in the propagation losses of interference cladding modes. Additionally, in a length of 6 cm, the spacing of the fringe will be narrow, which causes a limited measurement range.

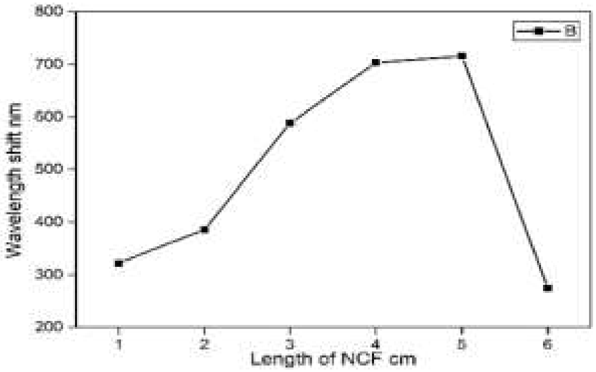

Figure (15): Relation between sensitivity in Pm/RH and the change in length of the NCF in cm.

Stability and reputability are another important conditions in the operation system of any sensor. The results of the spectrum shift as a function of RH were recorded in two different ways with increasing and decreasing RH that are shown in figure (16). The difference between the measurements was one day and the sensor still works normally with good stability and repeatability.

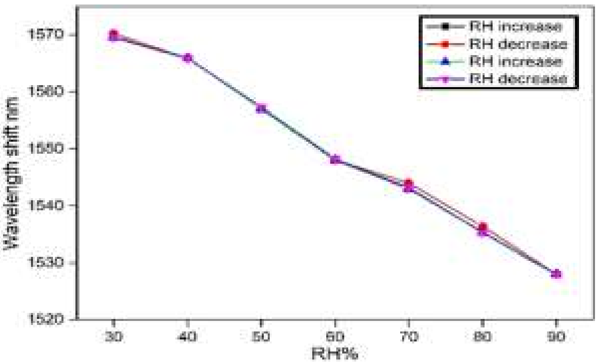

Figure (16): Humidity stability and Reputability.

4. Conclusion

In summary, a simple reflective optical fibre humidity sensor based on no core fibre (NCF) prepared. The structure has been fabricated by using different lengths of NCF with diameter 125µ□ where splicing to SMF. The end of NCF has cleaved to get a flat (mirror) end. Humidity (RH) ranged 30%-90% at temperature ~ 30 °C.

As the humidity increases, the reflection spectrum of the sensor moved toward the short wave direction (blue shift). The sensitivity increase as the length increases from the length 1 cm to length 5 cm. The sensitivity was increased 322.1 pm/RH%, 385 pm/RH%. 7,588.5 pm/RH%, 703.5 pm/RH%, 716.07 pm/RH%, and 272.1 pm/RH% at a length of 6cm. It can be concluded the highest sensitivity is achieved 716.07 pm/RH% at the length of 5 cm, and at length 6 cm the sensitivity will be decreased to 272.1 pm/RH%. This is because at a length 6 cm, the propagation losses of interference cladding modes are increased. Furthermore, the spacing of the fringe will be narrow, which causes limited measurement, and hence the sensitivity is decreased. The proposed humidity sensor shows good repeatability and stability with high sensitivity.

5. Reference

[1] Hamid Farahani , Rahman Wagiran and Mohd Nizar Hamidon "Humidity Sensors Principle, Mechanism, and Fabrication Technologies: A Comprehensive Review". Sensors. 14, 7881-7939, 2014.

[2] Zhang, Z.F.; Zhang, Y. "Humidity sensor based on optical fiber attached with hydrogel spheres". Opt. Laser Technol. 74, 16–19, 2015.

[3] Torres, D.L.; Elousa, C.; Villatoro, J.; Zubiac, J.; Rothhardt, M.; Schuster, K.; Arregui, F.J. "Enhancing sensitivity of photonic crystal fiber interferometric humidity sensor by the thickness of SnO2 thin films". Sens. Actuators B Chem. 251, 1059–1067,2017.

[4] Y. Zhao, X.G. Li, L. Cai, et al., "Measurement of RI and temperature using composite interferometer with hollow-core Fiber and photonic crystal fiber", IEEE Trans. Instrum. Meas. 65 (11), 2631–2636,2016,

[5] Y. Zheng, L.H. Chen, X. Dong, et al., Miniature pH optical Fiber sensor based on Fabry–Perot interferometer, IEEE J. Sel. Top. Quantum Electron. 22(2), 1–5, 2016.

[6] Y. Sun, D. Liu, P. Lu, et al., "High sensitivity optical fiber strain sensor using

twisted multimode fiber based on SMS structure", Opt. Commun. 405, 416–420 2017.

[7] S. Wu, G. Yan, Z. Lian, et al., "An open-cavity Fabry–Perot interferometer with PVA coating for simultaneous measurement of relative humidity and temperature", Sensors Actuators B 225, 50–56,2016.

[8] Z. Shao, X. Qiao, W. Bao, et al., "Temperature-independent gas refractometer based on an S-taper fiber tailored fiber Bragg grating", Opt. Commun. 374, 34–38 2016.

[9] Q. Hu, S. Zhang, W. Yang, et al., "Highly sensitive curvature sensor based on long period fiber grating with alternately splicing multiple single/multimode structure", Opt. Fiber Technol., Mater. Devices Syst. 37, 69–73 2017.

[10] Rajan,G. "Advanced Techniques and Applications", Optical Fiber Sensors 1st ed.; CRC Press: Boca Raton, FL, USA, 2015.

[11] Hartog, A. "An Introduction to Distributed Optical Fibre Sensors", 1st ed.; CRC Press: Boca Raton, FL, USA, 2017.

[12] Li-Peng Sun, Jie Li, Long Jin, Yang Ran, Bai-Ou Guan. "High-birefringence microfiber Sagnac interferometer based humidity sensor", Sensors and Actuators B231, 696-700, 2016.

[13] Cheng Zhou, Qian Zhou, Bo Wang, Jiajun Tian, and Yong Yao. "High-sensitivity relative humidity fiber-optic sensor based on an internal–external Fabry–Perot cavity Vernier effect". Optics Express, Vol. 29, No. 8, 11854, 2021.

[14] Piaopiao Wanga, Kai Ni, Bowen Wanga, Qifei Maa, Weijian Tian. "Methylcellulose coated humidity sensor based on Michelson interferometer with thin-core fiber". Sensors and Actuators, A288, 75-78, 2019.

[15] Suaad Sahib Hindal, Hanan J. Taher. "Performance of humidity sensor based on photonic crystal fiber interferometer". Iraqi Journal of Physics,Vol.14, No.30, PP. 83-89, 2016.

[16] Huda T. Al-Swefee, Sarah K. Al-Hayali and Abdulhadi A. Al-Janabi."Enhanced Relative Humidity Sensor via Diameter of No-Core Fiber Structure". Iraqi J. Laser, No.1, Vol.18, pp.19-23, 2019.

[17] Socorro, A.B.; Del Villar, I.; Corres, J.M.; Arregui, F.J.; Matias, "I.R. Mode transition in complex refractive index coated single-mode–multimode–single-mode structure". Opt. Express, 21, 12668–12682, 2013.

[18] Wang, Q.; Farrell, G. "All-fiber multimode-interference- base refractometer sensor: Proposal and design". Opt. Lett. 31, 317–319, 2006.

تأثير التغيير في الطول للالياف المنزوعة اللب لقياس التحسس للرطوبة النسبية

سرور لازم ,حنان جعفر.

معهد الليزر للدراسات العليا، جامعة بغداد، بغداد، العراق

الخلاصة: تم بناء متحسس للرطوبة النسبية الذي يعمل في نمط الانعكاس، حيث تم تصنيع المتحسس باستخدام أطوال مختلفة من الألياف منزوعة القلب ذات أطوال مختلفة (1-6) سم وقطر ثابت 125مايكروميتر ذو نهايات مسطحة ولحامها مع ليف بصري أحادي. تم ضبط الرطوبة داخل الجهاز لقياس الرطوبة (30%-90%) بدرجة حرارة مقاربة 30سيلزي.أضهرت النتائج المختبرية أن قمم التداخل تقل تدريجيا مع زيادة نسبة الرطوبة والتحسس يزداد بزيادة الطول للألياف منزوعة القلب. حيث إن قمم التداخل تزحزحت نحو الأطوال الموجية القصيرة مع زيادة مقدار الرطوبة. تزداد التحسس عند زيادة الطول للألياف منزوعة القلب حيث كانت اعلى قيمة للتحسس (716.07بيكومتر/النسبة المئوية للرطوبة النسية) للطول 5 سم. اظهر المتحسس استقراريه عالية. يمتاز متحسس الرطوبة المصمم بأنه ذو حجم صغير، سهولة تصنيع وحساسية عالية.

Iraqi J. Laser, issue 2, vol., 20, pp. 24-31 (2021)

IRAQI
JOURNAL
OF
LASER

Experimental Study to The Effect of Applying Stressing Force on Etched Polarization Maintaining Fiber as Hybrid Fabry-Perot /Mach-Zehnder inline fiber interferometer

Nada F. Noori [1], **Tahreer S. Mansoor** [1]
**Corresponding author: Tahreer@ilps.uobaghdad.edu.iq*
1. Institute of Laser for Postgraduate Studies, University of Baghdad, Iraq, Baghdad, Iraq.

(Received 27/10/2021; accepted 29/12/2021)

Abstract: The increased interest in developing new photonic devices that can support high data rates, high sensitivity and fast processing capabilities for all optical communications, motivates a pre stage pulse compressor research. The pre-stage research was based on cascading single mode fiber and polarization maintaining fiber to get pulse compression with compression factor of 1.105. The demand for obtaining more précised photonic devices; this work experimentally studied the behavior of Polarization maintaining fiber PMF that is sandwiched between two cascaded singe mode fiber SMF and fiber Bragg gratings FBG. Therefore; the introduced interferometer performed hybrid interference of both Mach-Zehnder and Fabry-Perot interferometers. The hybrid interference is resulted from the interference of the forward, backward and X,Y polarization components of the propagating light along the cascaded fibers. In conclusion spectral pulse compression with maximum compression factor in range of 3-6 was obtained by tuning applied stress on the shortest etched PMF segment of the interferometer (i.e. 8cm length). Such interferometer can support fine tunable all optical band pass filter

Key words: inline fiber interferometer, polarization maintaining fiber, HF fiber etching, Mach-Zehnder interferometer

1. Introduction

Hybrid Inline fiber interferometers are trending among the recent research areas due to their attractive advantages of light weight, compact size, immunity to electromagnetic interference [1], signal modulation capability, pulse compression [2], simultaneous sensing capability of two or more measured and, compatibility with fiber-based systems [3]. Moreover; current trends in fiber optic interferometers is to minimize the device for micro-scale applications. Since the interferometers provide a lot of temporal and spectral information, the detected signal can be quantitatively determined by various means for detecting the changes in the wavelength, phase, intensity, frequency, bandwidth, and so on [4]. With these sensing indicators, they achieved remarkable performance with large dynamic range, high accuracy, and high sensitivity [5]. Hybrid inline fiber interferometer usually can be built by cascading more than one type of interpolated misalignment along the optical bath of the fiber. such misalignment was ensured in previous studies by both cascading different types of optical fibers and imposing a reflective cross-sectional surface in addition to tapering of two or more regions along the same optical fiber...etc. and in our previous work [6-9]. Polarization maintaining fibers PMF are generally used to eliminate the effect of polarization mode dispersion along optical fibers. Polarization mode dispersion usually alter the phase of the propagating mode along the optical fiber [9]. Hybrid inline fiber interferometer were implemented in pre-stage work by sandwiching multi-mode fiber between two single mode-fiber Bragg gratings [8]a very fine tuned optical filter was obtained while PMF sandwiched between two single mode fibers was used to build Mach-Zehnder interferometer PM-

MZI [10]. The introduced PM-MZI worked as goon pulse compressor with pulse compression factor of 1.103 compression [2],[10]. While compression factor of 0.99 were ensured after our pre-stage work using photonic crystal fiber [11].

Fabry-Perot interferometer (FPI) sensors are widely used in a variety of fields that range from industry to biochemistry has become an attractive choice for force and strain sensing for their compact structure, high sensitivity, flexibility and small cross sensitivity. Through the strain experiment, they found that the interferometer with a larger cavity has a higher strain sensitivity.[12],[13],[14]

This work experimentally studied the effect of applying mechanical stressing force on etched polarization maintaining fiber sandwiched between two FBG cavity to produce hybrid Fabry-Perot Mach-Zehnder inline fiber interferometer. Since the two identical highly reflecting FBG (>90%) operates as Fabry-Perot cavity and the cascaded structure that consists from etched polarization maintaining fiber between two single mode fiber works as Mach Zehnder interferometer. Five different mass weights were used to apply mechanical stress along the etched PMF and thus the resulted change in optical power, central wavelength shift and spectral width were recorded.

2. Method and procedure

Hybrid inline fiber interferometer occurs when interference pattern obtained along the optical fiber due to more than one mechanism[15][16]. In this work hybrid inline fiber interferometer is obtained from two types of interferometers in one structure. The first type is the Mach-Zehnder interferometer which is implemented using 20 min etched polarization maintaining fiber of three different lengths (8,16, and 24 cm) sandwiched between two single mode fibers of 10 cm length. Since the polarization maintaining fiber has a beat length L_B characteristic which defines the length that polarization components of the propagating light will be remained separated along the fiber[9],[17]. The L_B of the used PMF (Thorlabs- PMDCF) in this work is equal to 5mm and hence interference between the different polarization components will be occurred after 5mm along the second single mode fiber. In addition to polarization components interference we have the evanescent wave obtained on the edges of the etched region of the PMF which develops some unguided waves propagating in the clad of the PMF at the etched zone resulting from the difference of the effective refractive index of the fiber at that zone, these unguided more recombined as guided modes again when they enter the second not etched segment of the PMF[18],[19]. The second interferometer type in this work is the Fabry-Perot inline fiber interferometer resulted from the interference of the forward and backward light waves reflected between the two identical fiber Bragg gratings applied on the both sides of the previously mentioned Mach-Zehnder interferometer as shown in the experimental schematic diagram of figure (2). The interference pattern of any interferometers can simply be described by the general interference formula expressed in equation Error! Reference source not found.. The developed phase change along each separated Mach-Zehnder arm of this work can be expressed by equation Error! Reference source not found. [6],[21]-[22]

$$\mathbf{H(\lambda) = I_1(\lambda) + I_2(\lambda) + 2\sqrt{I_1(\lambda)I_2(\lambda)}\ \cos(\Delta\varphi)} \ldots\ldots\ldots\ldots\ldots\ldots\ldots\ldots\ldots\ldots (\mathbf{1})[23]$$

$$\boldsymbol{\varphi} = \frac{\boldsymbol{\omega\Delta n_{eff}\, L}}{\mathbf{c}} \ldots\ldots\ldots\ldots\ldots\ldots\ldots\ldots\ldots\ldots (\mathbf{2})[23]$$

Where $I_{1,2}$ represent the intensity of interfering light beams as a function of wavelength and φ represent the phase change of the interfering waves and it is a function of effective refractive index change Δn_{eff}, angular frequencyω, wavelength λ and optical path length L.

Beat length L_B of the polarization maintain fiber is directly related to the birefringence B can be calculated using equation Error! Reference source not found.. The birefringence B of the used PMF in this work is equal to 2.5×10^{-4}

$$\boldsymbol{LB = \frac{2\pi}{\Delta\beta} = \frac{\lambda}{B}} \ldots\ldots\ldots\ldots\ldots\ldots\ldots\ldots\ldots\ldots (\mathbf{3})[\mathbf{9}]$$

$$\boldsymbol{B = \Delta n_{eff} = n^x_{eff} - n^y_{eff}}[9]$$

Where Δβ is the difference between the two x and y components of wave propagation constant along the PMF and $n^{x,y}_{eff}$ is the effective refractive index as a function of wavelength for both x and y polarization component. The inline Mach-Zehnder interferometer at this work was designed according to phase equation (2); thus the Beat length 5mm gives phase difference N×75°, and three PMF lengths of 8cm, 16 and 24 which gives phase difference of N×58 ° and N×63°.

For hybrid interference the interference of each type of interferometer needs to be represented mathematically in separated formula thus the Mach-Zehnder interference is represented by equation (5) and the Fabry-Perot one is represented by equation (6) [24]

$$I_{MZ} = I_1 + I_2 + 2\sqrt{I_1 I_2}\cos\left(\frac{2\pi n_{eff} L_{mzi}}{\lambda}\right) \ldots\ldots\ldots.(5)$$

$$I_{FP} = I_{Fw} + I_{BW} + 2\sqrt{I_{FW} I_{BW}}\cos\left(\frac{4\pi n_{eff} L_{FPI}}{\lambda}\right)..(6)$$

where, I_1 and I_2 are the intensity of the core and cladding mode, respectively. I_{FW} and I_{BW} are the forward and backward reflected light intensities between FBGs respectively. $\Delta n_{eff} = n_{eff}^{core} - n_{eff}^{clad}$ effective refractive index difference between core mode and cladding mode. L_{mzi} and L_{FPI} are the length of Mach-Zehnder interferometer and Fabry-Perot cavity respective which are equal to 28,36 and 44 for the MZI and 78,86,94 cm for the FPI.

The applied force on the PMF was done using series of different weight masses laid side by side along the etched zone of the PMF. Since the etched region is very brittle therefore to protect it from being raptured or damaged a thin slice of glass was used to isolate the weight mass and uniformly distribute their stressing effect on the PMF. The applied weights with their equivalent force in Newton are shown in table (1)

Error! Reference source not found.): The Equivalent force of the applied weight masses on the PMF cross-sectional

Weight in (g)	Force (N)
0	0
40	0.392266
80	0.784532
150	1.470997
300	2.941

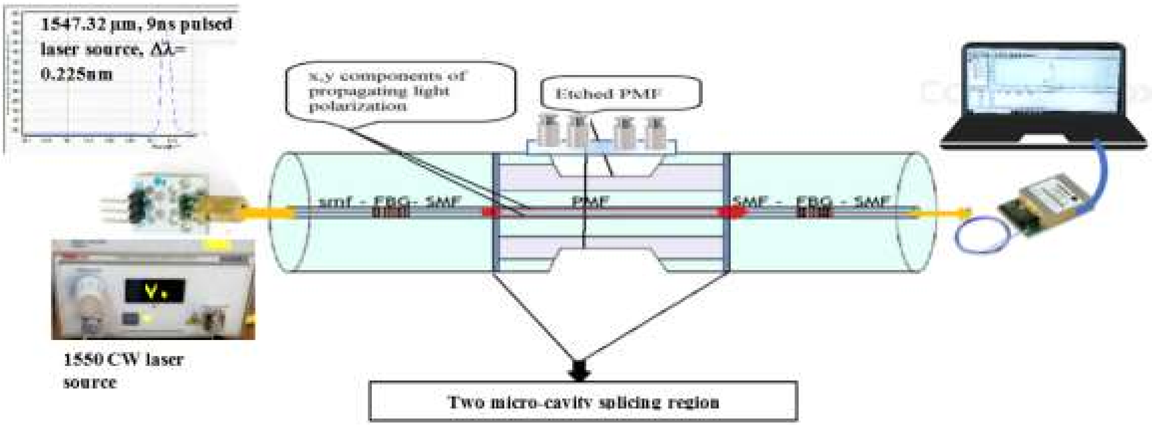

Figure (1): The schematic diagram of the experimental set up

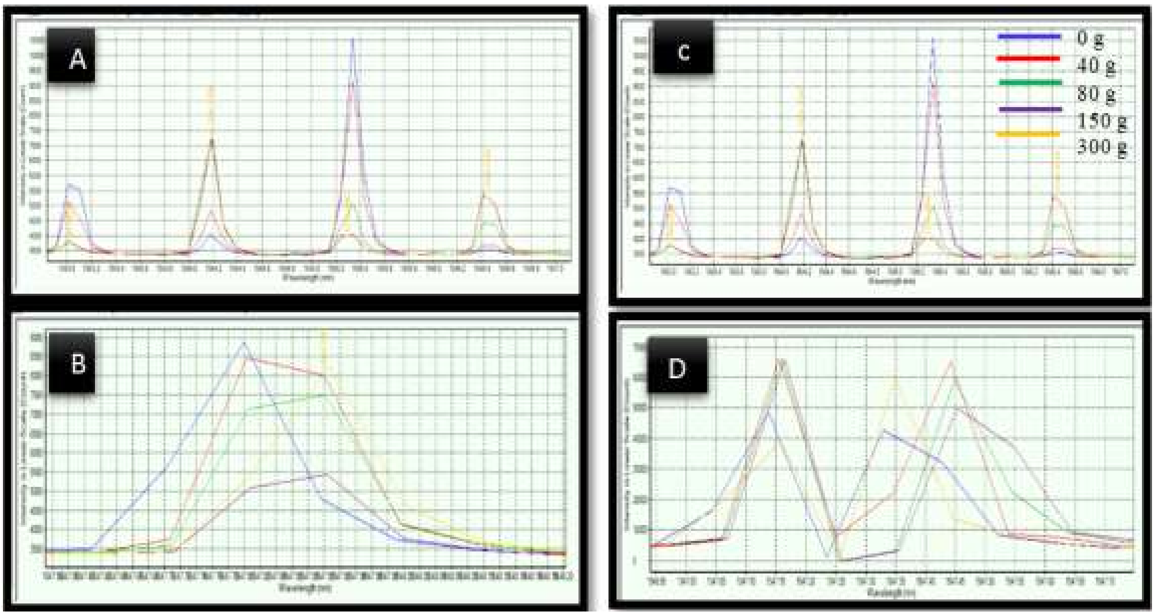

Figure (2): The spectrum of the experimental measurement output signal from the interferometer using FBGA interrogator. A: for the CW laser source and 8cm PMF, B: for pulsed laser diode and 8cm PMF, C: CW Laser with 16 cm PMF, D: pulsed laser and 16 cm PMF

The Experimental procedures were carried for two different types of C-band laser sources the first one is pulsed laser diode has central wavelength of 1547.32µm, 9ns pulse duration, 0.225nm spectral width and 1.33 mW peak power as shown in figure (2-a). while the CW laser has five peaks centered at 1542-1550 nm with 2nm spacing between each two consequent peak. The peak power obtained from the CW laser can be tuned from 0.2 to 0.9 mW but power of 0.7 mW was applied to the structure. The Fabry-Perot cavity was implemented using two identical fiber Bragg gratings of 1546.7 nm central wavelength, 90% reflectivity, 10 mm the grating segment length is 0.2 nm bandwidth The used spectral visualizer was FBGA interrogator (Bayspec) as shown in figure (2). In order to homogenously apply mass of 40 g along the etched region of the PMF; 4 masses of 10 g reference value was lied side by side next to each other along almost 4 cm of the etched fiber. the preparation of etched segment was explained in our previous work [7] by using HF bath of 4 cm length and hence there is an error percent raised from not all the clad was removed with same amount because the manual control to etching period is considered as source of error besides the cleaning of the sample after etching can take slightly different duration in seconds range they can be the second source of error

3. Results and discussion

The resulted effect of the stressing elements on the hybrid interferometer was investigated in term of central wavelength, spectral width, and Peak power variation as shown in figures (3-5) By looking for the central wavelength shift under the effect of stressing weight; it is obvious that there is almost no magnificent shift. Most cases are of nearly same central wave length except the case of FBG- cavity with CW laser source the fluctuation toward the shorter wavelengths were occurring as a result of the increasing of the applied stress.

The proposed advantage of using the FBGs around the both ends of the PMF is to produce the hybrid interference between forward and backward wave with PM-MZI interferometer. Thus Fabry-Perot cavity operation can be obtained. Then expected behavior of such hybrid interferometer is to increase the quality of the signal obtained from stress detection region along the etched PMF and obtain higher power from the interferometer. But unfortunately according to figures (3-5) (a) we can see that FBG cavity decreased the power of the hybrid interferometer FP-PMMZI incredibly. However still the Fabry Perot cavity showed feasible change to the pulse width (FWHM) against the applies stress when it is compared with the case of PM-MZI alone without cavity.

The central wavelength change was very slight in the most cases except for the 24 cm PM-MZI and 24 cm FP-PMMZI we can see slight obvious red-shift.

Spectral pulse compression of were obtained with highest compression factor ($FWHM_{i/p}/ FWHM_{o/p}$) of 6.818 with the shortest cavity of 8cm PMF length but range between 1-3 spectral compression were obtained from the whole structure as shown in Table (2- a & b)

Table (2): The spectral pulse compression factor with respect to applied stress in case of (a) No Fabry Perot Cavity, (b) Fabry Perot Cavity

	(a) No Fabry –Perot Cavity			(b) Fabry –Perot Cavity		
Force (N)	***8cm PMF***	***16 cm PMF***	***24cm PMF***	***8cm PMF***	***16 cm PMF***	***24cm PMF***
0	1.44230769	0.81227437	1.53061224	1.65441176	0.80357143	1.70454545
0.392266	1.28571429	0.86538462	3.125	2.08333333	0.76013514	1.99115044
0.784532	3	0.74013158	1.63043478	4.32692308	0.76271186	0.80357143
1.470997	4.24528302	0.9	2.16346154	4.32692308	1.99115044	3.16901408
2.941	3.62903226	0.74013158	1.74418605	6.81818182	2.10280374	1.875

The tunable spectral width of the interferometer can be used as tunable band pass filter that can be tuned over very fine range in nm regime for the used laser in this study tuning range of the spectral pulse was between 0.1-0.3 nm.

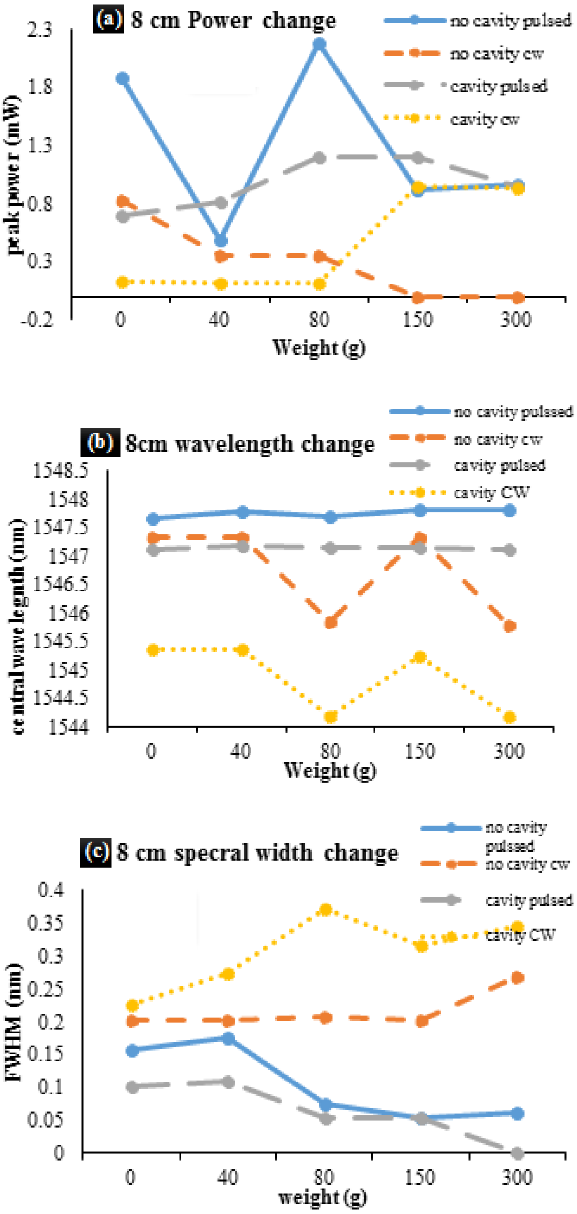

Figure (3): The effect of stressing weights on the 8cm PM-MZI. (a) power change, (b) wavelength change and (c) is the FWHM change with respect to stress

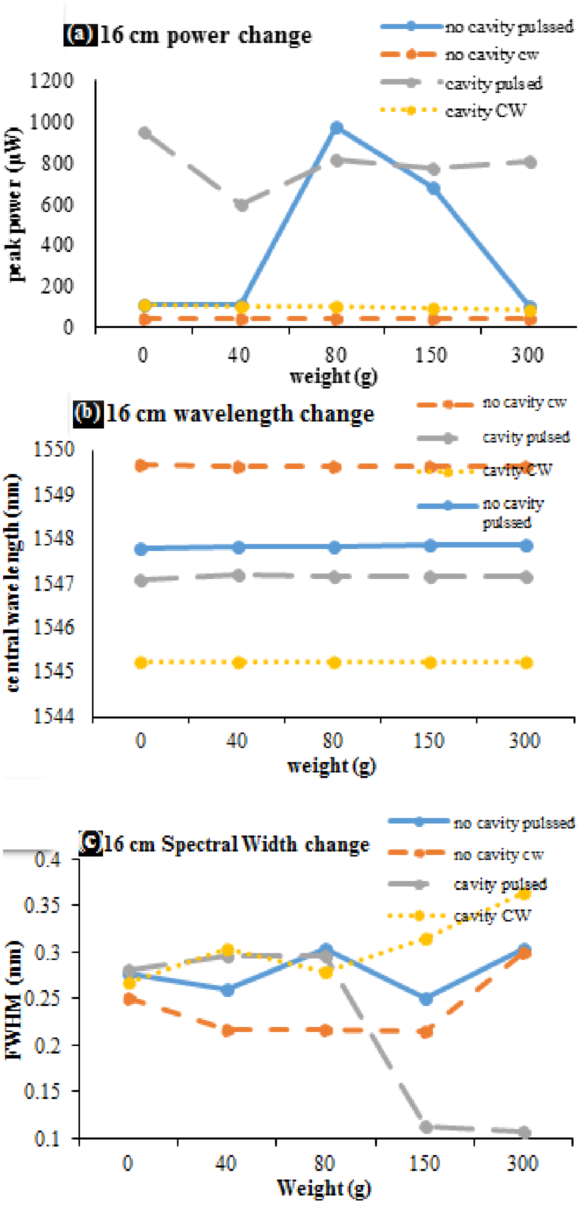

Figure (4): The effect of stressing weights on the 16 cm PM-MZI. (a) power change, (b) wavelength change and (c) is the FWHM change with respect to stress.

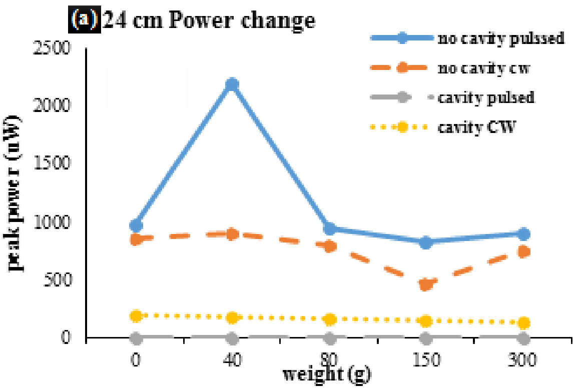

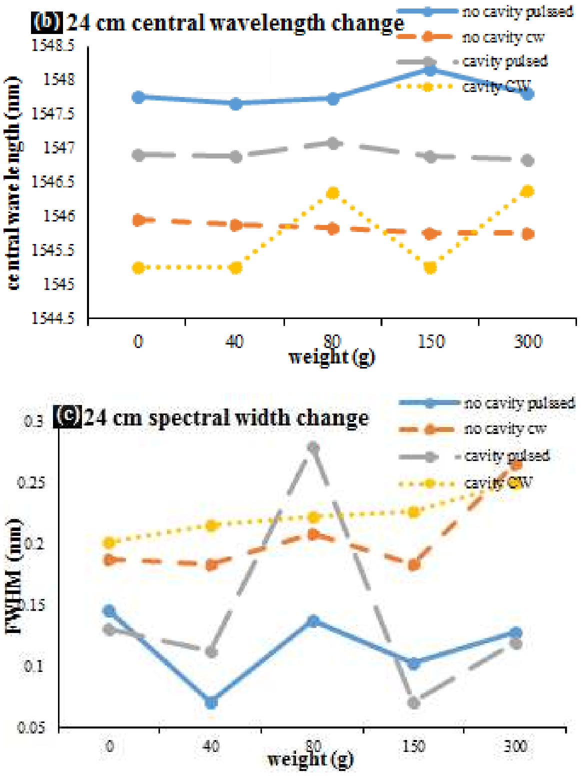

Figure (5): The effect of stressing weights on the 24 cm PM-MZI. (a) power change, (b) wavelength change and (c) is the FWHM change with respect to stress

4. Conclusions

This paper studied experimentally the effect of stressing Hybrid Fabry-Perot/ Mach-Zehnder interferometer consists from polarization maintaining fiber, single mode fiber and fiber Bragg grating and in conclusion it was found that Fabry-Perot cavity reduced the wavelength shift that should have occurred under stress and out power is reduced significantly. In contrast to previous PM-MZAI [2]; this FP-PMMZI developed temporal dispersion to optical pulse and significant spectral pulse width compression with tunable compression factor that increases by increasing the applied tuning stress. Therefore tunable all optical spectral band pass filter was obtained.

5. References

[1] Zhu, T., Wu, D., Liu, M., & Duan, D. W. In-line fiber optic interferometric sensors in single-mode fibers. Sensors, **12**, (8), pages 10430 – 10449. Switzerland (2012). https://doi.org/10.3390/s120810430

[2] Mutar, B. H., Noori, N. F., Hammadi, Y. I., & Mansour, T. S. In-line fiber tunable pulse compressor using PM-Mach Zehnder interferometer, Journal of Mechanical Engineering Research and Developments, **44,** (5), 287–297 (2021).

[3] Li, L., Xia, L., Xie, Z., Hao, L., Shuai, B., & Liu, D. In-line fiber Mach-Zehnder interferometer for simultaneous measurement of refractive index and temperature based on thinned fiber. Sensors and Actuators, A: Physical, **180,** 19–24. (2012).https://doi.org/10.1016/j.sna.2012.04.014

[4] Korposh, S., James, S. W., Lee, S. W., & Tatam, R. P.. Tapered Optical Fibre Sensors: Current Trends and Future Perspectives. Sensors (Switzerland), **19**(10). (2019) https://doi.org/10.3390/s19102294

[5] Bal, H. K., Brodzeli, Z., Dragomir, N. M., Collins, S. F., & Sidiroglou, F. Uniformly thinned optical fibers produced via HF etching with spectral and microscopic verification. Applied Optics, **51**(13), 2282–2287. (2012). https://doi.org/10.1364/AO.51.002282

[6] Krzysztof Iniewski, "OPTICAL FIBER SENSORS, Advanced Techniques and Applications", Taylor & Francis Group, 2015 International Standard Book Number-13: 978-1-4822-2829-8 (eBook - PDF)

[7] Tahreer S. Mansoor, N. F. N. (2021) "Theoretical and Experimental Study to The Effect of Etching on Polarization Maintaining Fiber of Mach-Zehnder interferometer", Design Engineering, pp. 6973-6981. Available at: http://www.thedesignengineering.com/index.php/DE/article/view/4188 (Accessed: 16October2021).

[8] Tahreer S. Mansoor, N. F. N. (2021). Design and Construction of Tunable Band Pass Filter Using Hybrid FPMZI. Design Engineering, 6959-6972. Retrieved from http://www.thedesignengineering.com/index.php/DE/article/view/4187

[9] Ivan P. Heckman, Alan E. Willner, "optical fiber telecommunications" Academic Press is an imprint of Elsevier, California 92101-4495, USA Theobald's Road, London WC1X 8RR, UK, ISBN: 978-0-12-374171-4

[10] Mutar, B. H., & Mansour, T. S. "Design of Tunable Optical Band Pass Filter based on in-Line PM- Mach Zehnder Interferometer". Iraqi Journal of Laser, **20**(1), pp. 6-12. (2021). Available at:

https://ijl.uobaghdad.edu.iq/index.php/IJL/article/view/257 (Accessed: 22August2021).

[11] Wang, X., Liao, J., Pan, J., Yang, H., & Li, X. (2021). Observation of Ultrashort Laser Pulse Evolution in a Silicon Photonic Crystal Waveguide. 2–7.

[12] Guozhao Wei, Qi Jiang, Force sensitivity and fringe contrast characteristics of spheroidal Fabry-Perot interferometers. Optics express vol. 28, issue 17, page 24586–24598. 2020

[13] Chyad, R. M., Ali, A. H., Hammed, A. A., Mahdi, B. R., Khalef, N. H., Mahmoud, A. I., & Rasheed, H. M.. Acoustic Fiber Sensors by Fabry- Perot Interferometer technology. Journal of Physics: Conference Series, 1660(1). (2020) https://doi.org/10.1088/1742-6596/1660/1/012052

[14] Xu, Y., Lu, P., Chen, L., & Bao, X. Recent developments in micro-structured fiber optic sensors. Fibers, 5(1). (2017). https://doi.org/10.3390/fib5010003.

[15] Peng, W., Zhang, X., Gong, Z., & Liu, Y.. "Miniature fiber-optic strain sensor based on a hybrid interferometric structure". IEEE Photonics Technology Letters, 25(24), 2385–2388. (2013) https://doi.org/10.1109/LPT.2013.2284965

[16] Wang, J., Liu, B., Wu, Y., Mao, Y., Zhao, L., Sun, T., Nan, T., & Han, Y. Temperature insensitive fiber Fabry-Perot / Mach-Zehnder hybrid interferometer based on photonic crystal fiber for transverse load and refractive index measurement. Optical Fiber Technology, **56** 7–13. (November 2019), https://doi.org/10.1016/j.yofte.2020.102163

[17] John Senior, M. Yousif Jamro," Optical Fiber Communications Principles and Practice", Third edition, Prentice Hall Europe, 2009, ISBN: 978-0-13-032681-2

[18] Patil, S. H., Saha, A., & Barma, M. D. Performance analysis of cladding etched fiber Bragg grating based refractive index sensor. 2018 2nd International Conference on Electronics, Materials Engineering and Nano-Technology, IEMENTech 2018, 6, 1–3. https://doi.org/10.1109/IEMENTECH.2018.8465251

[19] Kumar, A., Single Mode Optical Fiber based Refractive Index Sensor using Etched Cladding. 0–4. 2011https://doi.org/10.21427/wh9t-ce84

[20] Flores, R., Janeiro, R., & Viegas, J. Optical fiber Fabry-Pérot interferometer based on inline micro cavities for salinity and temperature sensing. Scientific Reports, 9(1), 1–9. (2019) https://doi.org/10.1038/s41598-019-45909-2

[21] Series Editors Paul L. Kelley, Ivan P. Kaminow, Govind P. Agrawal, "Applications of Nonlinear Fiber Optics", Academic press, ISBN:0-12-045144-1, https://doi.org/10.1016/B978-0-12-374302-2.X5001-3

[22] Li, L., Xia, L., Xie, Z., Hao, L., Shuai, B., & Liu, D. In-line fiber Mach-Zehnder interferometer for simultaneous measurement of refractive index and temperature based on thinned fiber. Sensors and Actuators, A: Physical, 180, 19–24. (2012). https://doi.org/10.1016/j.sna.2012.04.014

[23] Zhu, C. C., Yu, Y. Sen, Zhang, X. Y., Chen, C., Liang, J. F., Liu, Z. J., Meng, A. H., Jing, S. M., & Sun, H. B. Compact Mach-Zehnder interferometer based on tapered hollow optical fiber. IEEE Photonics Technology Letters, 27(12), 1277–1280. (2015). https://doi.org/10.1109/LPT.2015.2417212

[24] Wang, J., Liu, B., Wu, Y., Mao, Y., Zhao, L., Sun, T., Nan, T., & Han, Y. Temperature insensitive fiber Fabry-Perot /Mach-Zehnder hybrid interferometer based on photonic crystal fiber for transverse load and refractive index measurement. Optical Fiber Technology, 56, 7–13. (2020). https://doi.org/10.1016/j.yofte.2020.102163

دراسة عملية لتأثير الاجهاد المسلط على ليف بصري مستقطب محفور مستخدم لبناء مداخل ضوئي خطي ليفي هجين بين نوعي ماخ زندر وفابري بيروت

ندى فارس نوري   د. تحرير صفاء منصور

معهد لليزر للدراسات العليا – جامعة بغداد

الخلاصة: الحاجة المتزايدة لتطوير أجهزة فوتونية لها القدرة على نقل إشارات الاتصالات الضوئية بكميات كبيرة وسرع عالية حفز لتقديم هذا البحث الذي يعتبر تتمة الى بحث سابق مبني بنفس الالياف وتمكن من تحقيق ضغط للبضة البصرية بمعامل ضغط مقداره 1.105. هذا البحث قدم دراسة عملية لمداخل ضوئي خطي مبني على تعاقب الالياف الضوئية وقد استخدم لغرض الدراسة ليف بصري احادي النمط على جانبي ليف بصري مستقطِب للضوء وحصر الجميع بليف بصري محزز نوع براغ ليقوم بعمل هجين بين نوعين من المدخلات الضوئية نوع فابري بيروت وماخ زندر معا. يتحقق المداخل نوع ماخ زندر من تداخل موجتين ذات استقطاب مختلف اما النوع الثاني من المداخلات وهو فابري بيروت فيتحقق نتيجة لتداخل الموجة الساقطة والمنعكسة على حزوز الليف المحزز. تمكن هذا النوع الهجين من المداخلات الليفية الخطية من تحقيق انضغاط طيفي للموجة الخارجة منه بمعامل انضغاط يتراوح بين 3-6 وسجل اعلى انضغاط مع أقصر طول لليف المستقطب للضوء وهو 8سم كما وتم تمكين تعيير الانضغاط للموجة بتسليط اجهاد على المنطقة المحفورة من الليف.

Iraqi J. Laser, issue 2, vol., 20, pp. 32-41 (2021)

IRAQI
JOURNAL
OF
LASER

On the use of Aluminium as a plasmonic material in polarization rotators based on a hybrid plasmonic waveguide

Farooq Abdulghafoor Khaleel[1,*], **Shelan Khasro Tawfeeq**[1]

**Corresponding author: farook.abd1101a@ilps.uobaghdad.edu.iq*

1. *Institute of Laser for Postgraduate Studies, University of Baghdad, Iraq, Baghdad, Iraq.*

(Received 21/11/2021; accepted 29/12/2021)

Abstract: The Aluminium (Al) material emerged as a plasmonic material in the wavelength ranges from the ultraviolet to the visible bands in different on-chip plasmonic applications. In this paper, we demonstrate the effect of using Al on the electromagnetic (EM) field distribution of a compact hybrid plasmonic waveguide (HPW) acting as a polarization rotator. We compare the performance of Al with other familiar metals that are widely used as plasmonic materials, which are Silver (Ag) and Gold (Au). Furthermore, we study the effect of reducing the geometrical dimensions of the used materials on the EM field distributions inside the HPW and, consequently, on the efficiency of the polarization rotation. We perform the study based on the Finite Element Method (FEM) using COMSOL software at an operation wavelength of 700 nm. This paper verifies that the Al could be used as an efficient plasmonic material in integrated single-photon sources for quantum key distribution systems.

Key words:

1. Introduction

The photonic applications at the visible and infrared wavelengths depend widely on plasmonics. Recent researches showed considerable progress in plasmon-based light trapping [1, 2], surface-enhanced spectroscopy [3, 4], sensors [5, 6], optoelectronic devices [7, 8], nonlinear optics [9, 10], and photocatalysis [11, 12]. In nanoscale devices, extending the plasmonic excitation effect from infrared, visible to the ultraviolet wavelengths range is a major challenge. The challenge arises from the limited performance (i.e. weak resonance effect) of the common plasmonic metals, which are Au and Ag, at the visible and UV wavelengths ranges [13, 14]. The Ag exhibited rapid oxidation that deteriorates the plasmonic effects, while the interband transitions in Au increase at the visible wavelength ranges and below and act as a dissipative channel that weakens the plasmonic effect [15, 16]. However, the Al emerged as a preferable plasmonic metal at the visible and UV wavelengths because of its strong resonance at these wavelengths, natural availability, low cost, and fabrication easiness and accuracy down to 5 nm linewidth [17, 18].

One of the most important integrated plasmonic devices is the polarization rotators [19]. Recently, the polarization rotators are applied in integrated single-photon sources in polarization-based quantum key distribution systems [20]. The aim of [20] was to control the output polarization of the emitted photons from a quantum emitter (QE) coupled to an HPW acting as a polarization rotator. Moreover, the emission wavelength of most QEs is 700 nm, where the Au and Ag plasmonic metals begin to lose their plasmonics properties [21].

This paper compares the performance of using Au, Ag, and Al as plasmonic metals in polarization rotators based on HPW. Furthermore, the effect of using different plasmonic metals on the miniaturization of the integrated HPW will also be discussed. This paper is arranged as follows: Section (2) demonstrates the principles of the polarization rotators. Section (3) compares the performance of the polarization rotator using different plasmonics metals. Finally, Section (4) concludes our findings.

2. The principles of integrated polarization rotators

In general, the HPW at the telecommunication wavelengths (1.3 or 1.55) µm is composed of a thin dielectric spacer of low refractive index (silica (SiO_2)) that separates a high refractive index medium (silicon (Si)) from a metal conductor (gold (Au) or silver (Ag)) as shown in figure (1).

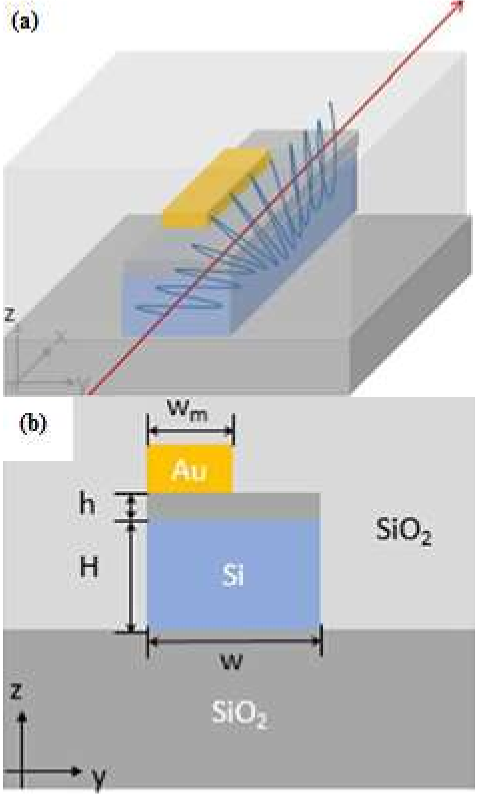

Figure (1): The general structure of an HPW at a wavelength of 1.55 µm, (a) A 3D view, (b) A 2D cross-section [22]

The HPW propagation modes are a combination of the photonic modes supported by the high refractive index medium (i.e. photonic waveguide) and the SPP modes at the metal-dielectric boundary (i.e. PW). The HPW combines two features— the small losses feature exhibited by a photonic waveguide and the high light confinement feature exhibited by the PW [22]. The HPW is selected as a basis for polarization rotators because of its structure and features.

Figure (1. a) presents how the HPW can perform as an integrated linear polarization rotator. Figure (1. b) shows the rotator's cross-section, which shows that the metal has a reduced width than the Si and SiO_2 layers forming an asymmetric HPW [22]. The asymmetry structure destroys the horizontal symmetry in the Si and, consequently, rotates the optical axes of the supported propagation eigenmodes. Therefore, the asymmetric HPW supports two orthogonal propagation modes rotated by an optical axis angle (θ), which is defined by [23]:

$$tan(\theta) = \iint \frac{\epsilon(y,z)E_y^2(y,z)dydz}{\epsilon(y,z)E_z^2(y,z)dydz} \ldots\ldots\ldots\ldots (1)$$

Where $\epsilon(y,z)$ is the real part of the permittivity distribution in the (y-z) plane, and E_z and E_y are the horizontal and transversal electric field distribution of the propagation mode, respectively. The resulting two orthogonal propagation modes for the polarization rotator presented in Figure (1) are shown in Figure (2) for different Au widths (w_m) [22]:

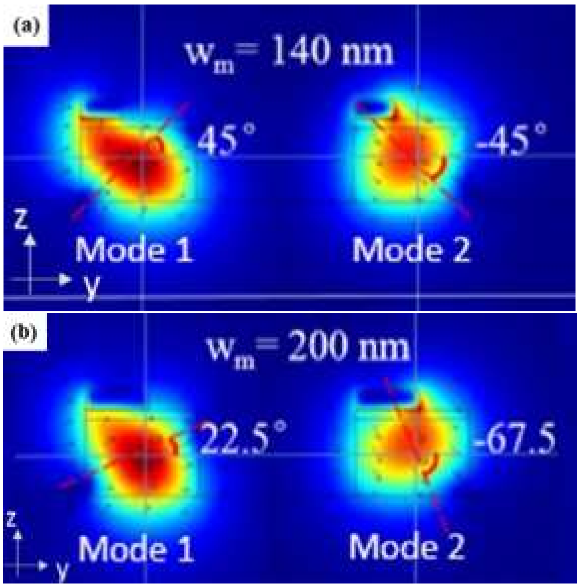

Figure (2): The magnetic field distribution of the two orthogonal propagation modes for an Au width of (a) 140 nm and (b) 200 nm resulting in θ of 45° and 22.5°, respectively [22]

The Au's width varies the angle of the optical axis of the propagation mode, and consequently, the output polarization. Moreover, the Au's length (L) identifies the difference between the phase (δ) of the two propagation modes in the metal part, which are related by [23]:

$$\delta = \frac{2\pi L}{\lambda}|n_1 - n_2| \ldots\ldots\ldots\ldots\ldots\ldots\ldots\ldots\ldots\ldots\ldots (2)$$

Where n_1 and n_2 are the real parts of the effective indices of the two orthogonal propagation modes, and λ is the wavelength. Consequently, by selecting a certain metal length and width, the rotator can perform as λ/4 or λ/2 waveplate. The polarization rotator proposed in [23] operates efficiently at a 1550 nm wavelength. However, it is a challenge to find a metal that preserves the orthogonality of the propagation modes at 700 nm. Such a metal is required in polarization rotators that control the emission polarization of an embedded QE inside the HPW. Besides, alternative materials to Si and SiO_2 should be chosen to support the light's propagation at 700 nm. Table (1) shows the n and κ for different materials, where n is the real part of the material's refractive index that determines the light's phase velocity and κ is the imaginary part of the material's refractive index that determines the attenuation coefficient.

The Si material shows a considerable value of κ at 700 nm and, hence, the light propagating in the Si material is significantly attenuated as Beer-Lambert law implies. Recently, gallium phosphide (GaP) played an important role in many modern photonic integrated circuits (PICs) [26]. GaP supports strong light confinement and small mode volume due to its high refractive index at 700 nm [27]. Consequently, the alternative material at 700 nm that shows a comparable refractive index for the Si at 1550 nm is the GaP as shown in Table (1).

Moreover, the SiO_2 and the hydrogen silsesquioxane (HSQ) materials show a comparable refractive index at a wide range of wavelengths as shown in Table (1). However, the HSQ material is selected as a basis for the 700 nm HPW because it is a widely used material in on-chip plasmonic single-photon sources and it could be experimentally converted to SiO_2 with the same performance [21, 28]. The reasons for choosing the Al as a plasmonic material include its strong plasmonic resonance, simple manufacturing processes, and low cost [29]. The Al could be fabricated down to a 5 nm scale, which makes it easily handled during the manufacturing process [17, 18]. Both gold and silver exhibit high plasma wavelength and, therefore, weak plasmonic resonance in contrast to Al at 700 nm. Although the Au and Ag have approximately comparable refractive indices as shown in Table (1), Au and Ag failed to achieve the polarization rotation at a wavelength of 700 nm because of the real part n's deterioration.

Table (1): The refractive indices information for different materials [24]

Material	**n**	**κ**	**n**	**κ**	**n**	**κ**	**The model**
	@ 700 nm		**@ 1.3 µm**		**@ 1.55 µm**		
Si	4.0679	0.25109	3.5226	0	3.48	0	Pierce and Spicer
SiO_2	1.4553	0	1.4469	0	1.444	0	Malitson
Au	0.131	4.0624	0.38797	8.7971	0.52406	10.742	Johnson and Christy
Ag	0.041	4.8025	0.10898	9.4317	0.14447	11.366	Johnson and Christy
GaP	3.2992	0	3.1447	0	3.128	0	Adachi
HSQ	1.41	0	1.41	0	1.41	0	Dow Corning® XR-1541 E-Beam Resist [25]
Al	1.9214	8.142	1.3481	12.917	1.5785	15.658	Rakić

3. Simulation results

The polarization rotation requires that the GaP photonic waveguide supports two orthogonal propagation modes for each case of output polarization, which was achieved by using Al (strong plasmonic resonance) instead of Au and Ag (weak plasmonic resonance) as shown in Figure (3) for 0°, 90°, 45°, and -45° output polarization cases. In the following simulations, the refractive index information for Al and GaP are based on RakiA and Aspnes and Studna models, respectively, that are defined in the COMSOL's material library. Consequently, the refractive indices for the Al and GaP are 1.9214 + 8.142i and 3.2543 at 700 nm, respectively. Figure (3) shows that there exist two orthogonal modes, for each case of output polarization, supported by the HPW at optimum dimensions.

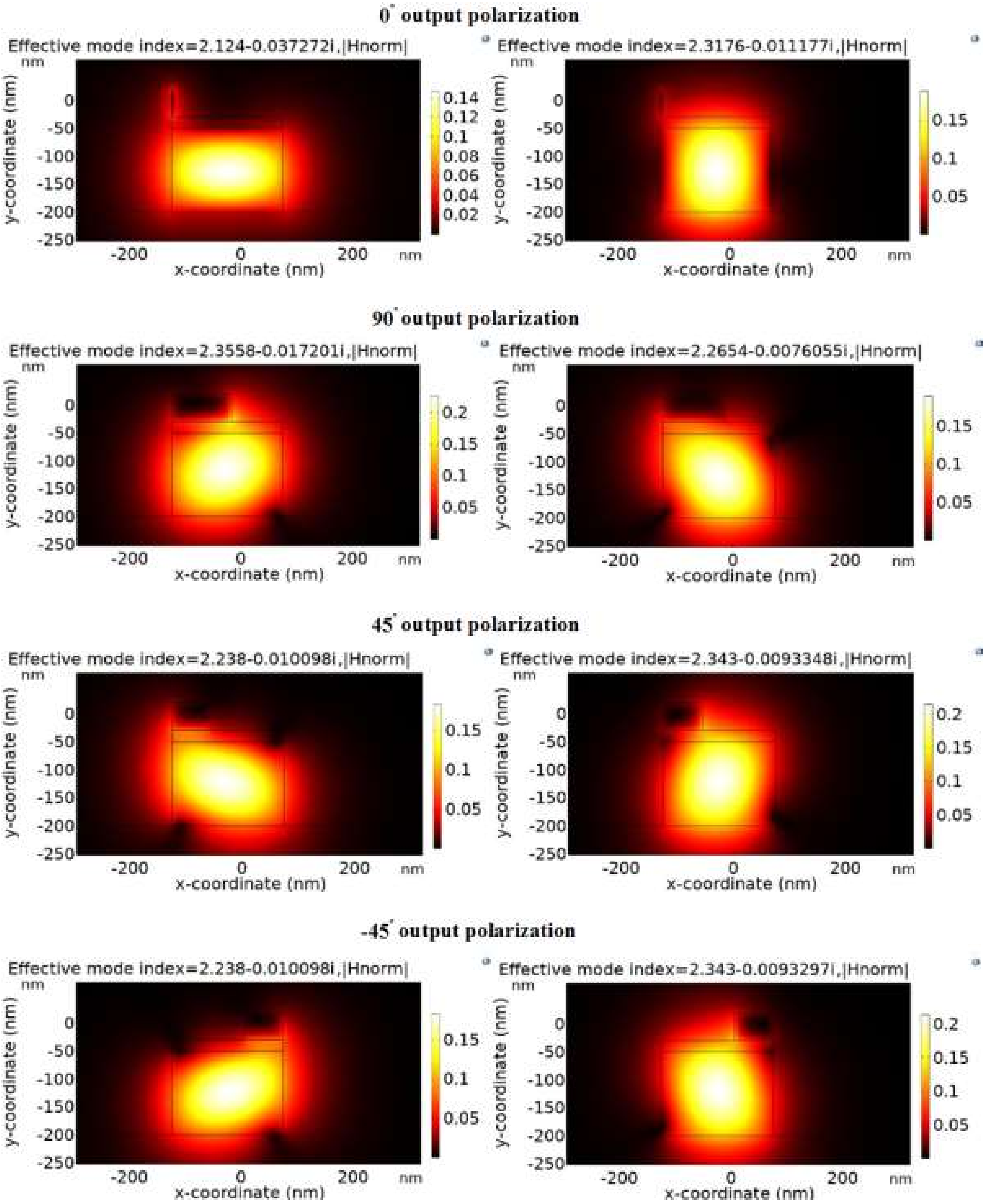

Figure (3): The two orthogonal modes supported by the HPW for each case of output polarization for Al material at 700 nm

However, the propagation modes lose their orthogonality if an Au or Ag metal is used instead of the Al metal (at the same optimum dimensions) as shown in figure (4).

Au, 0°, output polarization

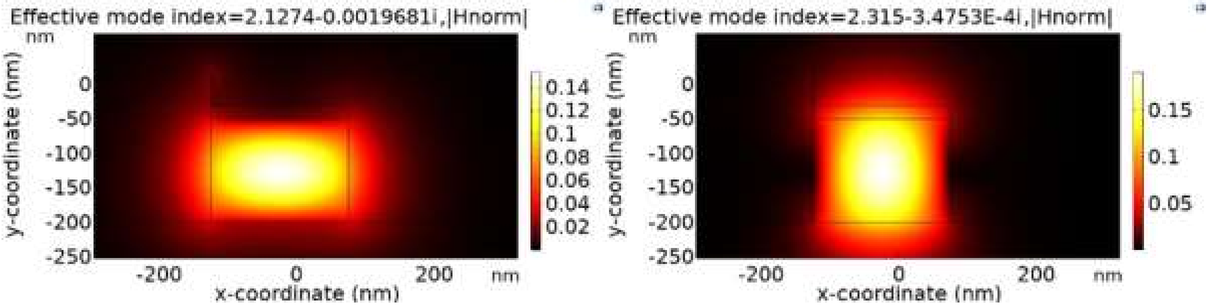

Au, 90°, output polarization

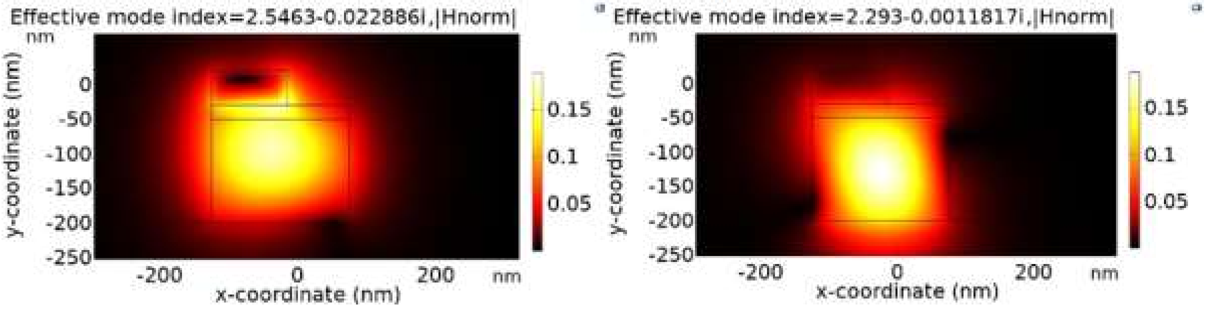

Au, 45°, output polarization

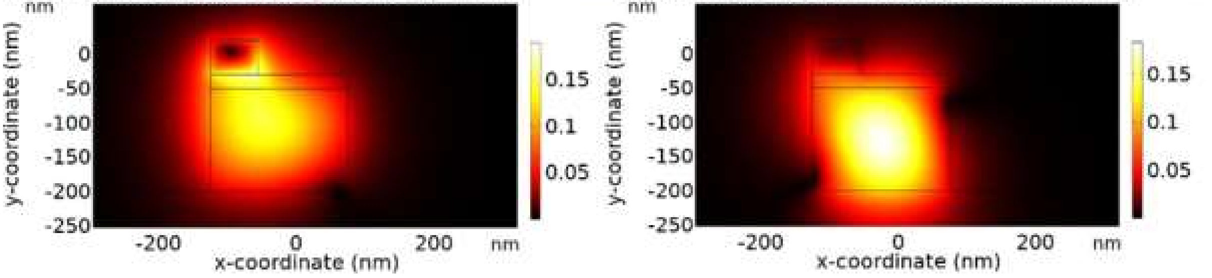

Au, -45°, output polarization

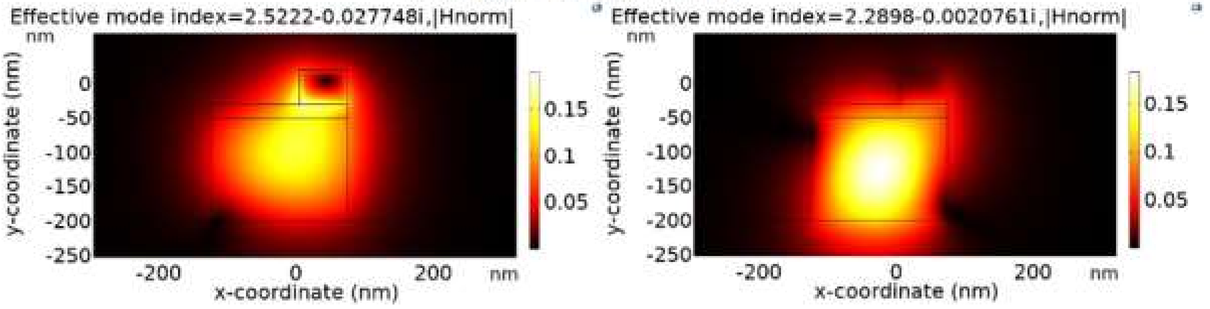

Ag, 0°, output polarization

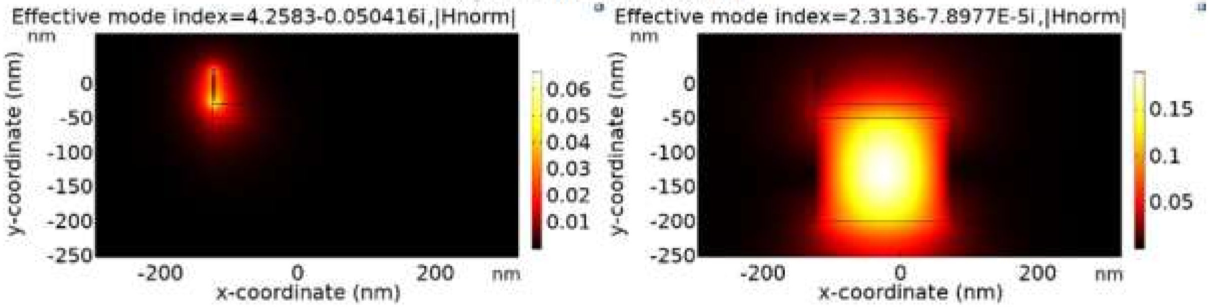

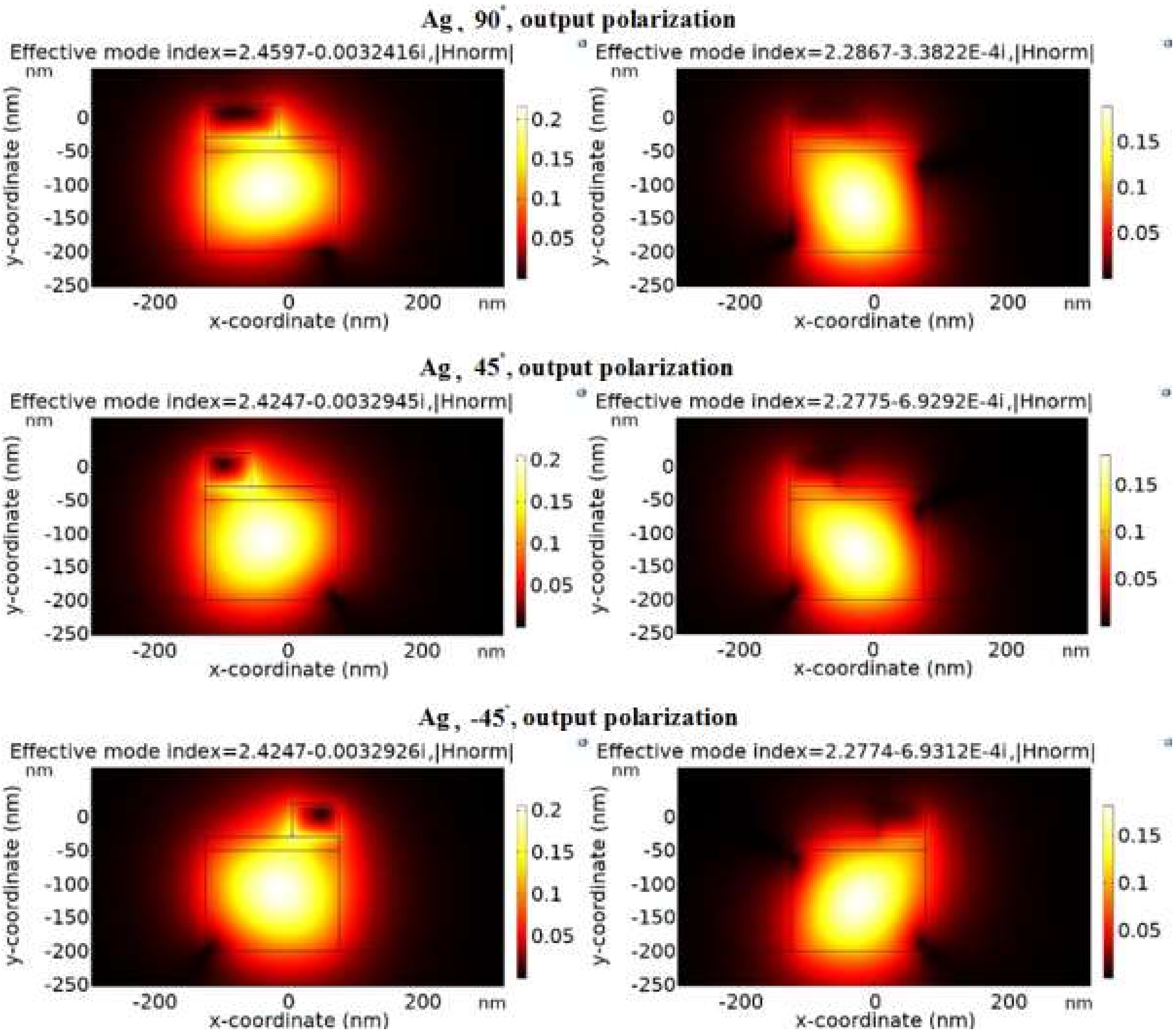

Figure (4): The two orthogonal modes supported by the HPW for each case of output polarization when Au and Ag metals are used at 700 nm.

On another hand, a mandatory requirement to control the output polarization of the HPW is that the HPW's geometrical dimensions should support the propagation of two orthogonal modes. The dimensions of the HPW are determined by the local search algorithm. Most of the on-chip plasmonic single-photon sources used 250 nm (width) and 180 nm (height) for the HSQ pattern deposited above silver or gold as shown in figure (5) [21,28,30].

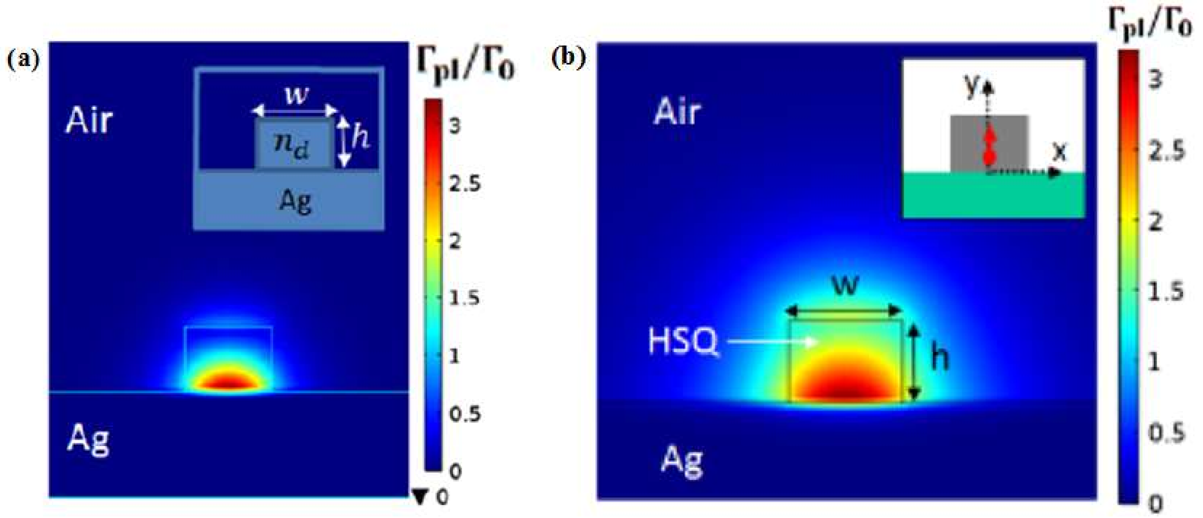

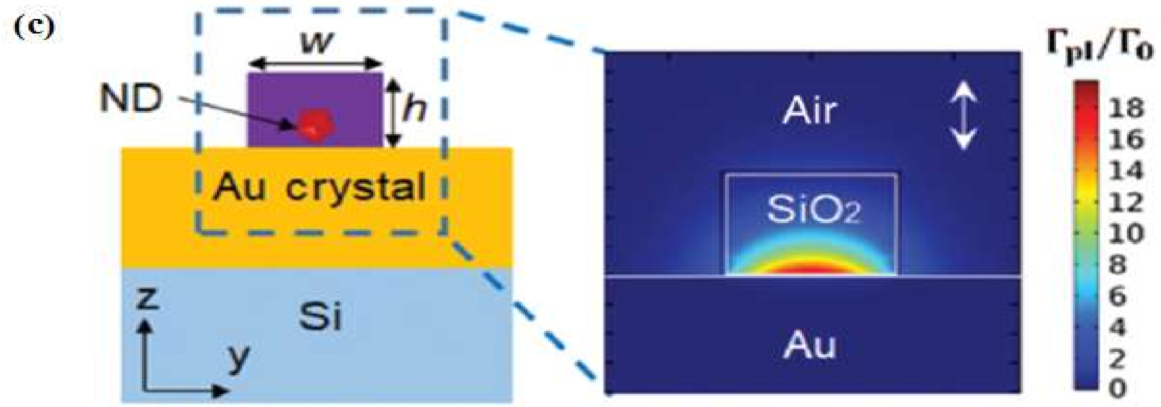

Figure (5): The HSQ's geometries in DLSPP waveguides used as on-chip plasmonic single-photon sources. (a) [21], (b) [30], (c) [28]

The 250 nm (width) and 180 nm (height) dimensions were considered as a reference to select the GaP photonic channel dimensions in the HPW, which achieved the orthogonality of the propagation modes condition in the GaP region as shown in Figure (6. a,b). However, the proposed work tends to miniaturize the dimensions of the HPW to save space on the integrated circuit. Hence, the width and the height of the GaP photonic waveguides decreased while keeping the Al bar and the HSQ spacer heights fixed at 50 nm and 20 nm, respectively. The minimum dimensions of the GaP region that supports the propagation of two orthogonal modes are 200 nm (width) and 150 nm (Height) as shown in Figure (6. c,d). The propagation modes lose their orthogonality if the GaP's width or height is reduced to 190 nm or 145 nm, respectively, as shown in Figure (6. e-h).

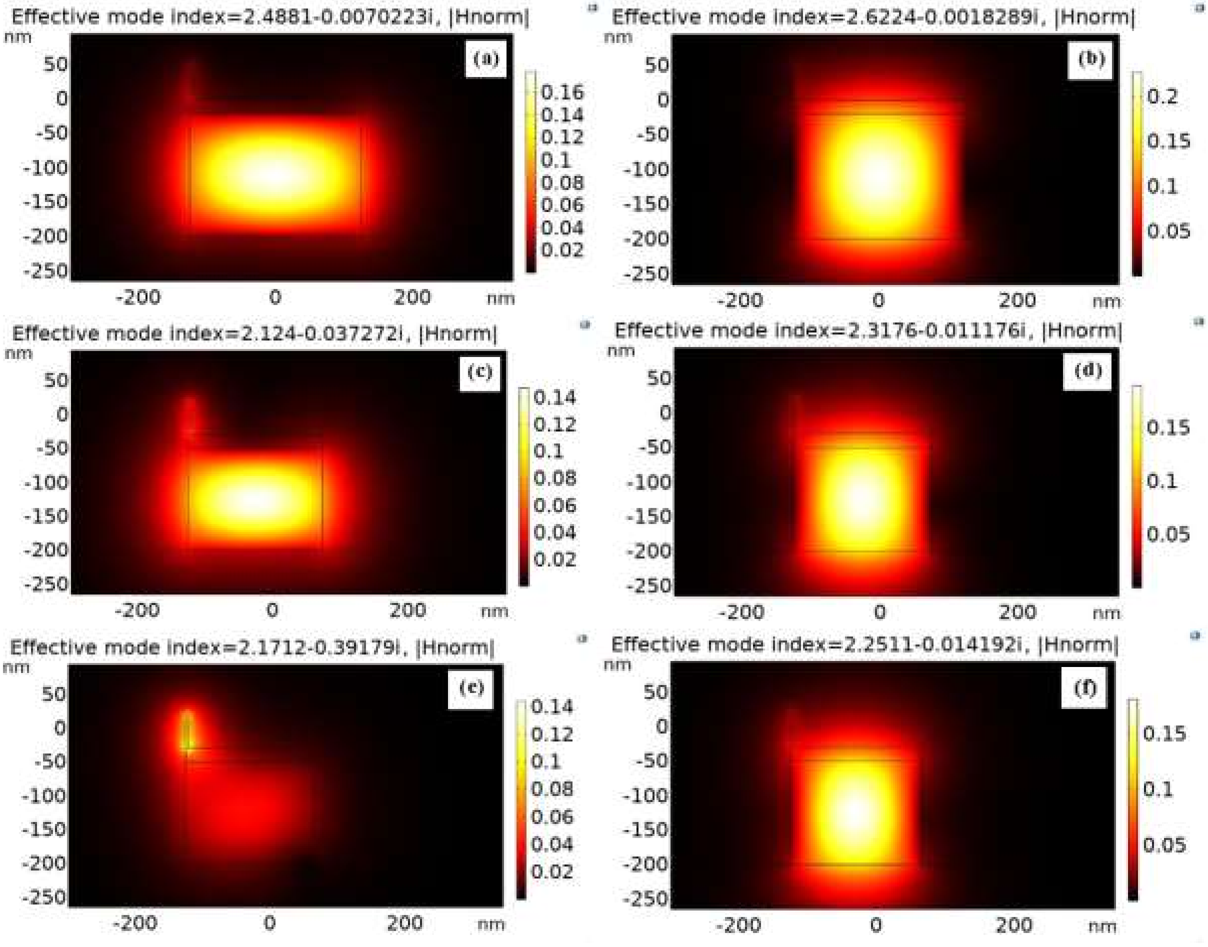

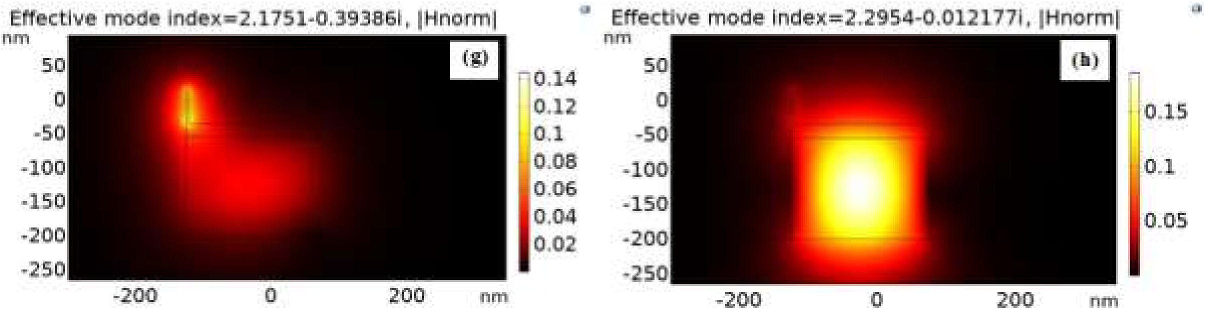

Figure (6): The orthogonal modes field distribution when the width and height of the GaP region is (a), (b) 250, 180 nm, (c), (d) 200, 150 nm, (e), (f) 190, 150 nm, and (g), (h) 200, 145 nm, respectively.

The HSQ spacer covers the GaP and, consequently, has the same width as the GaP layer. However, the HSQ spacer's height and the Al bar's width affect the mechanism of the polarization control technique, and, consequently, their optimum values are justified in [20]. Finally, the Al metal height affects the orthogonality of the propagation modes. If the Al metal bar height is set to 45 nm, the orthogonality is lost as shown in figure (7. a,b). Consequently, the minimum Al bar's height that enables the GaP region to support the propagation of two orthogonal modes is 50 nm as shown in figure (7. c,d).

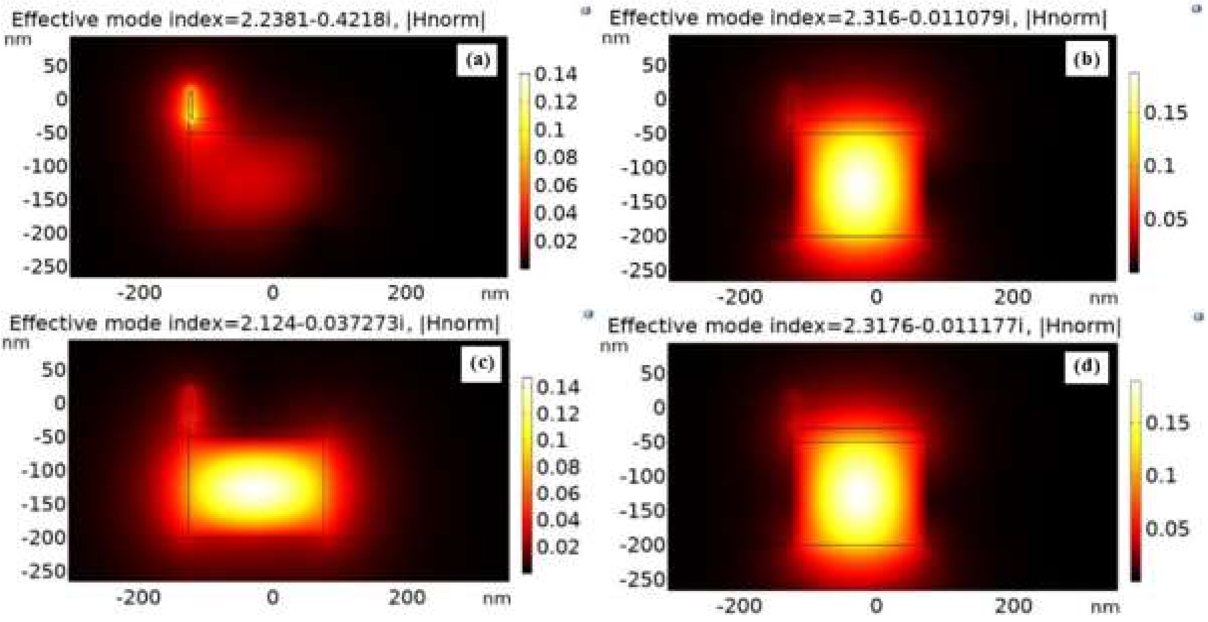

Figure (7): The orthogonal modes field distribution with Al bar's height of (a), (b) 45 nm, and (c), (d) 50 nm.

4. Conclusions

The Al metal proved to be an efficient plasmonic material for 700 nm wavelength plasmonic applications in comparison to Au or Ag. The Al succeeded in preserving the orthogonality of the propagation modes for the HPW with minimum possible geometrical dimensions. Other metals could be investigated for different plasmonic applications at the visible and UV wavelengths range such as copper, lead, etc. Moreover, the compactness of the plasmonic polarization rotator has its unique geometrical limitations. Different PW topologies could be further investigated in the future for further miniaturization of the plasmonic circuit at the visible or UV wavelengths range.

5. References

[1] T.F. Villesen, C. Uhrenfeldt, B. Johansen, A.N. Larsen, Self-assembled Al nanoparticles on Si and fused silica, and their application for Si solar cells, Nanotechnology. 24 (2013).

[2] T.F. Villesen, C. Uhrenfeldt, B. Johansen, J.L. Hansen, H.U. Ulriksen, A.N. Larsen, Aluminum nanoparticles for plasmon-improved coupling of light into silicon, Nanotechnology. 23 (2012).

[3] C. D'Andrea, J. Bochterle, A. Toma, C. Huck, F. Neubrech, E. Messina, B. Fazio, O.M. Maragò, E. Di Fabrizio, M. Lamy de La Chapelle, P.G. Gucciardi, A. Pucci, Optical Nanoantennas for Multiband Surface-Enhanced Infrared and Raman Spectroscopy, ACS Nano. 7 (2013).

[4] Y. Zheng, T. Thai, P. Reineck, L. Qiu, Y. Guo, U. Bach, DNA-Directed Self-Assembly of Core-Satellite Plasmonic Nanostructures: A Highly Sensitive and Reproducible Near-IR SERS Sensor, Adv. Funct. Mater. 23 (2013).

[5] N. Mattiucci, G. D'Aguanno, H.O. Everitt, J. V Foreman, J.M. Callahan, M.C. Buncick, M.J. Bloemer, Ultraviolet surface-enhanced Raman scattering at the plasmonic band edge of a metallic grating, Opt. Express. 20 (2012).

[6] A. Ono, M. Kikawada, R. Akimoto, W. Inami, Y. Kawata, Fluorescence enhancement with deep-ultraviolet surface plasmon excitation, Opt. Express. 21 (2013).

[7] H. Zhang, J. Zhou, W. Zou, M. He, Surface plasmon amplification characteristics of an active three-layer nanoshell-based spaser, J. Appl. Phys. 112 (2012).

[8] Y. Chen, G. Song, J. Xiao, L. Yu, J. Zhang, Subwavelength polarization beam splitter with controllable splitting ratio based on surface plasmon polaritons, Opt. Express. 21 (2013).

[9] A. Grubisic, V. Schweikhard, T.A. Baker, D.J. Nesbitt, Coherent Multiphoton Photoelectron Emission from Single Au Nanorods: The Critical Role of Plasmonic Electric Near-Field Enhancement, ACS Nano. 7 (2013).

[10] G.F. Walsh, L. Dal Negro, Enhanced Second Harmonic Generation by Photonic–Plasmonic Fano-Type Coupling in Nanoplasmonic Arrays, Nano Lett. 13 (2013).

[11] S. Mukherjee, F. Libisch, N. Large, O. Neumann, L. V Brown, J. Cheng, J.B. Lassiter, E.A. Carter, P. Nordlander, N.J. Halas, Hot Electrons Do the Impossible: Plasmon-Induced Dissociation of H2 on Au, Nano Lett. 13 (2013).

[12] A.O. Govorov, H. Zhang, Y.K. Gun'ko, Theory of Photoinjection of Hot Plasmonic Carriers from Metal Nanostructures into Semiconductors and Surface Molecules, J. Phys. Chem. C. 117 (2013).

[13] J.M. McMahon, G.C. Schatz, S.K. Gray, Plasmonics in the ultraviolet with the poor metals Al, Ga, In, Sn, Tl, Pb, and Bi, Phys. Chem. Chem. Phys. (Incorporating Faraday Trans. 15 (2013).

[14] G. V Naik, V.M. Shalaev, A. Boltasseva, Alternative Plasmonic Materials: Beyond Gold and Silver, Adv. Mater. 25 (2013).

[15] A. Taguchi, Y. Saito, K. Watanabe, S. Yijian, S. Kawata, Tailoring plasmon resonances in the deep-ultraviolet by size-tunable fabrication of aluminum nanostructures, Appl. Phys. Lett. 101 (2012).

[16] G. Maidecchi, G. Gonella, R. Proietti Zaccaria, R. Moroni, L. Anghinolfi, A. Giglia, S. Nannarone, L. Mattera, H.-L. Dai, M. Canepa, F. Bisio, Deep Ultraviolet Plasmon Resonance in Aluminum Nanoparticle Arrays, ACS Nano. 7 (2013).

[17] M. Kjaergaard, F. Nichele, H.J. Suominen, M.P. Nowak, M. Wimmer, A.R. Akhmerov, J.A. Folk, K. Flensberg, J. Shabani, C.J. Palmstrøm, C.M. Marcus, Quantized conductance doubling and hard gap in a two-dimensional semiconductor–superconductor heterostructure, Nat. Commun. 7 (2016).

[18] T. Morgan-Wall, H.J. Hughes, N. Hartman, T.M. McQueen, N. Marković, Fabrication of sub-15 nm aluminum wires by controlled etching, Appl. Phys. Lett. 104 (2014).

[19] F. Wang, Y. Chen, T. Ma, H. Liu, X. Wang, C. Jin, Mid-infrared polarization rotator based on a Si3N4-CaF2 hybrid plasmonic waveguide with asymmetric metal claddings, Appl. Opt. 60 (2021).

[20] F.A. Khaleel, S.K. Tawfeeq, The spontaneous emission performance of a quantum emitter coupled to a hybrid plasmonic waveguide with specified output polarization for on-chip plasmonic single-photon source, Photonics Nanostructures - Fundam. Appl. 45 (2021).

[21] H. Siampour, S. Kumar, S.I. Bozhevolnyi, Nanofabrication of Plasmonic Circuits Containing Single Photon Sources, ACS Photonics. (2017).

[22] L. Gao, Y. Huo, K. Zang, S. Paik, Y. Chen, J.S. Harris, Z. Zhou, On-chip plasmonic waveguide optical waveplate, Sci. Rep. 5 (2015).

[23] J.N. Caspers, M.Z. Alam, M. Mojahedi, Compact hybrid plasmonic polarization rotator, Opt. Lett. 37 (2012).

[24] Refractive index database, (n.d.). www.refractiveindex.info (accessed June 10, 2021).

[25] Dow Corning® XR-1541 E-Beam Resist, (2008).

[26] B. Tilmann, G. Grinblat, R. Berté, M. Özcan, V.F. Kunzelmann, B. Nickel, I.D. Sharp, E. Cortés, S.A. Maier, Y. Li, Nanostructured amorphous gallium phosphide on silica for nonlinear and ultrafast nanophotonics, Nanoscale Horiz. 5 (2020).

[27] K. Schneider, P. Welter, Y. Baumgartner, H. Hahn, L. Czornomaz, P. Seidler, Gallium Phosphide-on-Silicon Dioxide Photonic Devices, J. Light. Technol. 36 (2018).

[28] H. Siampour, O. Wang, V.A. Zenin, S. Boroviks, P. Siyushev, Y. Yang, V.A. Davydov, L.F. Kulikova, V.N. Agafonov, Ultrabright single-photon emission from germanium-vacancy zero-phonon lines : deterministic emitter-waveguide interfacing at plasmonic hot spots, Nanophotonics. (2020).

[29] M.W. Knight, N.S. King, L. Liu, H.O. Everitt, P. Nordlander, N.J. Halas, Aluminum for Plasmonics, ACS Nano. 8 (2014).

[30] H. Siampour, S. Kumar, S.I. Bozhevolnyi, Chip-integrated plasmonic cavity-enhanced single nitrogen- vacancy center emission, Nanoscale. (2017).

حول استخدام الالمنيوم كمادة بلازمونية في مدورات القطبية المبنية على الدليل الموجي الهجين

فاروق عبد الغفور خليل[1]* ، أ.م.د. شيلان خسرو توفيق[1]

[1]معهد الليزر للدراسات العليا – جامعة بغداد، بغداد - العراق

*Farook.abd1101a@ilps.uobaghdad.edu.iq

الخلاصة: ظهرت مادة الالمنيوم كمادة بلازمونية فعالة في الاطوال الموجية الممتدة من المدى تحت البنفسجي والمدى المرئي في عدة تطبيقات بلازمونية متكاملة. نستعرض في هذا البحث تاثير مادة الالمنيوم على توزيع المجال الكهرومغناطيسي لدليل موجي هجين مدمج يعمل كمدور قطبية. تمت مقارنة تاثير الالمنيوم مع مواد اخرى واسعة الاستخدام كمواد بلازمونية وهي الفضة والذهب. بالاضافة الى ذلك، تمت دراسة تاثير تصغير ابعاد المواد المستخدمة على توزيع المجال الكهرومغناطيسي في داخل الدليل الموجي الهجين وبالنتيجة على كفاءة تدوير القطبية. تم تنفيذ هذه الدراسة بناءا على نظرية العناصر المحددة باستخدام برنامج الكومسول وبطول موجي 700 نانومتر. يثبت هذا البحث كفاءة استخدام الالمنيوم كمادة بلازمونية في دوائر البواعث احادية الفوتون لانظمة توزيع المفتاح الكمي.

Iraqi J. Laser, issue 2, vol., 20, pp. 42-48 (2021)

IRAQI
JOURNAL
OF
LASER

Laser Micro and Nano Drilling of Aluminium Alloy Using Tungsten Carbide and Silica Carbide Nanoparticles

Nibras H. Abed [1,*], **Mahmoad SH. Mahmoad** [1]
**Corresponding author: nebras.hamed1201a@ilps.uobaghdad.edu.iq*
1. Institute of Laser for Postgraduate Studies, University of Baghdad, Iraq, Baghdad, Iraq.

(Received 19/12/2021; accepted 30/12/2021)

Abstract: The micro and nano drilling holes are produced by a Q-switched Nd :YAG laser (1064 nm) interaction with 8009 Al alloy using two kinds of nanoparticles. Nanoparticles are tungsten carbide (WC) and silica carbide (SiC). The micro and nano holes have been investigated with different laser pulse energies (600, 700 and 800)mJ, different repetition rates (5Hz and 10Hz) and different concentrations of nanoparticles (90%, 50% and 5%). The results indicate that micro and nano holes have been achieved under conditions of 600 mJ laser pulse energy, 5Hz laser repetition rate, and 5% concentration of the nanoparticles (for the two types of nanoparticles). The diameters of holes are increase to millimetres and cracks are formed with increasing of the laser pulse energy, laser repetition rate and high concentration of nanofluid.

Keywords: Laser Microdriling and Nanodrilling, Al-Alloy, Nanoparticles

1. Introduction

Drilling is one of the most common machining operations in the manufacturing industry [1]. Laser microdrillings give high aspect ratio than tool micro drillings. Minimum microhole sizes can be as low as 1 micron in thin materials. Microdrilling is not characterized just by small drills but also a accurate rotation technique of the special drilling cycle. The laser systems can be used for micromachining, microdrilling microcutting, precision machining, and fine cutting, microfabrication, marking, engraving and milling [2].

In laser beam machining process (LBM) the material removal rate (MRR) is not reliant on mechanical or physical properties of material but thermoptical properties of the material. In many cases, laser micromachining is a more cost-effective alternative to the processes such as electrical discharge micro machine (EDM). In most cases laser micromachining works best if the feature to be produced is less than 1mm in depth. For example, microhole drilling is normally limited to materials less than 1.5 mm thick and aspect ratios less than 30:1 [2, 3]. Laser microhole drilling processes provide access to world leading precision hole drilling technology. This process can be used by femtosecond laser micromachining with very high peak powers which provide for minimal thermal damage to surroundings and high aspect ratios [4]. Microdrilling process has a great use for manufacturing of sophisticated items. Laser microdrilling gives a high aspect ratio than tool micro drillings [5]. Generally, pulsed mode is used for laser micromachining with high resolution in depth and lateral dimensions. The parameters of laser beam such as pulse energy, pulse frequency, pulse width and focal length, additionally the properties of nanoparticles are very influential and enhanced the properties of holes. Laser drilling process can be applied on a wide range of different materials including of super alloys and irradiated on advanced materials like nanoparticles which its properties like higher toughness, ductility, high temperature stability, high strength and wear resistance make tungsten carbide(WC) and silica carbide(SiC) nanoparticles materials highly competitive against other conventional materials [4].

Pulsed Nd:YAG laser microdrilling on different materials have been carried out to study the effect of the process parameters which effect on material removal rate (MRR), formation of holes and heat affected zone (HAZ) width [6].

2. Laser interaction with nanoparticles

The interactions of the laser's electromagnetic wave with the electrons of a particle lead to absorption and scattering of the particle's electrons by the laser's photons. The particle warms up if the energy of the electrons can be quickly transferred to the crystal lattice due to excellent heat transfer between the electrons and the phonons.

The particle can melt and gradually fade away if enough energy is absorbed. The amount of energy that a particle absorbs from the pulse laser beam is calculated by [7]:

$$E_{abs} = \frac{E_\circ}{A_\circ}\sigma_{abs}^{\lambda} \ldots\ldots\ldots\ldots\ldots\ldots\ldots\ldots\ldots\ldots\ldots\ldots\ldots (1)$$

where $J = E_\circ / A_\circ$ and is laser fluence, E_o is pulse energy, A_o is spot size area and σ_{abs}^{λ} is the particles absorption cross section, which strongly depends on the laser wavelength, so the energy of the particle´s absorb is equal to [7]:

$$E_{abs} = J\sigma_{abs}^{\lambda} \ldots\ldots\ldots\ldots\ldots\ldots\ldots\ldots\ldots\ldots\ldots\ldots\ldots (2)$$

For a spherical shape of nanoparticles the amount of energy absorbed by nanoparticles can be calculated [7]:

$$Q_{abs}^{\lambda} = \frac{4\,\sigma_{abs}^{\lambda}}{\pi d_p^2} \ldots\ldots\ldots\ldots\ldots\ldots\ldots\ldots\ldots\ldots\ldots\ldots\ldots (2)$$

Where d_p the diameter of nanoparticle, Q is the absorption efficiency (unit less) and both Q and σ also strongly depend on laser wavelength, particle size and shape [7]. Tungsten carbide (WC) and Silica carbide (SiC) have hard-facing nanoparticles offer a distinct combination of high hardness and high toughness [8], with melting point (2870°C and 2730°C) respectively [9].

The absorption curves, Qabs = Qabs(dp) for the particles can be calculated when the absorption efficiency (or absorption cross section) was known. The amount of energy absorbed by a particle of any size from the laser pulse can be calculated using Eq. (1). According to the equation, this energy is spent for the particle heating–melting–evaporation process. If the amount of absorbed energy is rather small, only particle heating can be expected. And with more absorbed energy, melting occurs as can be shown in figure (1) [7].

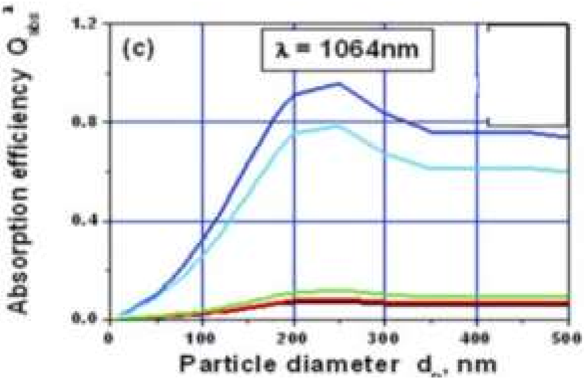

Figure (1): particle –size dependence of absorption efficiency for Nd:YAG laser[7]

There are three inherent problems. These problems are the high reflectivity of aluminium to light even down to short ultraviolet wavelengths (as shown in figure (2)), the high thermal conductivity of aluminium, and the self oxidation [10].

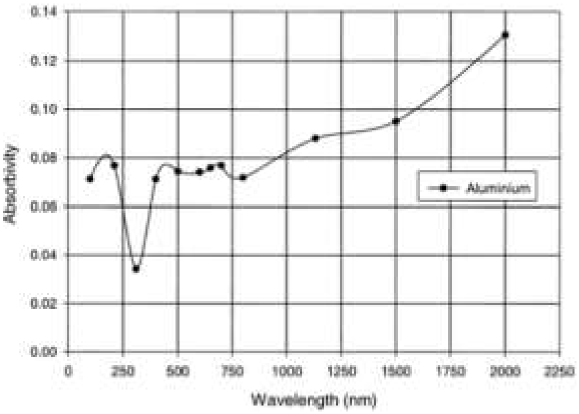

Figure (2): Absorptivity of aluminium as a function of incident wavelength [10]

Aluminium is the third most prevalent element in the Earth's crust. It is the chemical element of the 3rd group in the periodic table of the elements [11]. It has low melting and boiling point. The plasma formed above the surface of aluminium, will be responsible for changing the dimensions of the laser-drilled holes due to the transfer of heat to the material surface. This will therefore affect the precision obtainable. The emission of vapour and particulates from the surface during the interaction event will also be responsible for scattering the incoming radiation. Melt erosion of the sidewalls of the drilled hole caused by the high vapour pressure above the surface of the material during laser irradiation of the surface will push the melt up and out of the hole. This will also alter the geometry of the percussion-drilled the hole [10].

In this work, 8009 Al alloy was used because of the importance of this alloy in manufacturing a new supersonic aircraft, missile fins (it is the bases in which a 30- 40 % of weight saving may be expected), the helicopters transmission shafts, and many other different applications [12, 13]. Aluminium 8009 alloy has excellent heat resistant properties [14]. Additionally aluminium 8009 alloy can possess a desirable combination due to high temperature specific strength, corrosion resistance, electrical, thermal conductivity, and creep resistance at temperatures in excess of 300°C [15]

3. The experimental setup

The experimental setup for obtaining the micro and nano holes based on nanoparticles in different materials can be shown in figure (3).

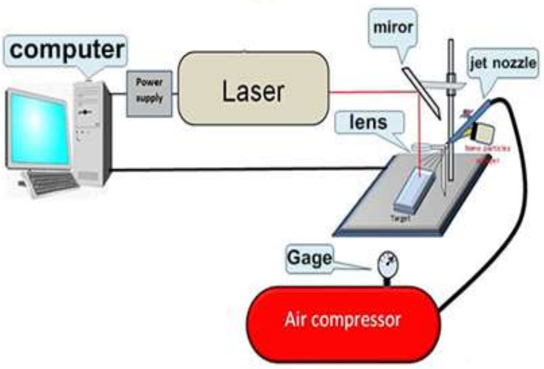

Figure (3): Schematic diagram of the experimental setup for laser metal micro and nano drilling by nanoparticles

The setup consists of Q-switched Nd:YAG laser (1064nm) source, air compressor which is pumping air to the jet nozzle. Two types of nanoparticles (tungsten carbide of 55nm grain size and silicon carbide of 50 nm grain size) were used separately; convex lens with 100mm focal length and the target was 8009 Al alloy of 0.1 mm thickness. This alloy has good thermal stability, high temperature strength and high wear resistance and good thermally properties [16]. The chemical components of this alloy are aluminium, manganese, titanium, iron, silicon, zinc and vanadium [17]. The laser pulse width is (10 ns), pulse repetition rates were (5 and 10) Hz, laser pulse energies were (600, 700, 800) mJ.

The initial step was to prepare the nanoparticle fluid by combining various percentages of nanoparticles with water to increase the performance and heat transmission characteristics of nanofluids [18]. This solution is placed on a magnetic stirrer device at 50°C for 20-30 minutes to create a homogenous suspended particulate solution with different nanoparticle concentration ratios (90%, 50%, and 5%)It is difficult to make the nanofluid to be totally homogeneous during the experiment because it needs time to take the nanofluid from the magnetic stirrer and then putting it in the container of jet nozzle and then using it for drilling.

The nanofluid is placed in a small container in the jet nozzle. This jet nozzle is connected to a compressor with air pressure (150-200) psi. The second step is using the jet nozzle to spray the nanofluid on the material's surface. The laser beam is focused on the nanofluid spray above the surface of aluminium alloy at the same moment. This method is applied with the two types of nanoparticles and with the same laser parameters but with different exposure time.

4. Result and discussion

4.1 Drilling of Aluminium alloy without using nanoparticles

When the laser pulse energy was 600mJ, and increased to (700-800)mJ, repetition rate is 10Hz and exposure time is (40sec), the drilling holes were not obtained, as shown in figure (4). This figure shows the effect of the laser pulse on the alloy. There is only a thermal effect (without obtaining any holes on the target). This means that the laser with its maximum energy, with high repetition rate and with a long exposure time, couldn't make any hole in the target.

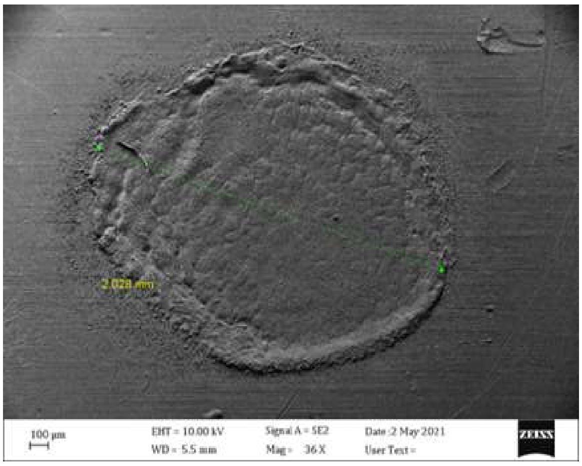

Figure (4): The FESEM test of aluminium alloy without nanoparticles (laser energy is 800mJ, repetition rate is 10Hz and exposure time is 40 se**c**

4.2 Drilling of Aluminium alloy with silicon carbide (SiC) nanoparticles

When the concentration ratio of nanofluid is 90% (of nanoparticles), the laser pulse energy is 800mJ, repetition rate is 10Hz and exposure time is (5-10) sec, the aggregations of nanoparticles and microcracks were obtained on the target, as shown in figure (5). This case can be attributed to the high concentration of nanoparticles and high laser energy leading to very large numbers of (SiC) nanoparticles are melted in a very short time (5sec.) and falling on the target. Some of them cause cracks and others cause agglomerations on the surface.

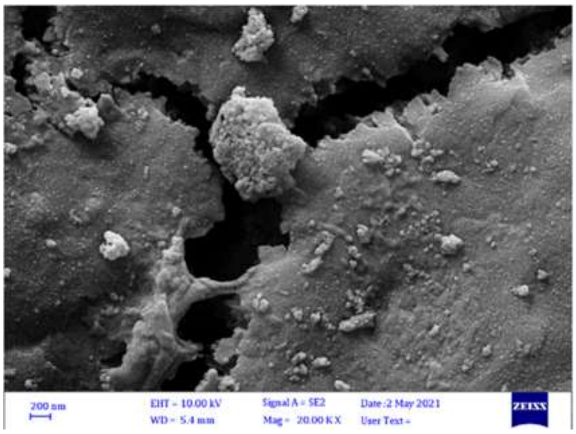

Figure (5): The FESEM test Aluminium alloy drilled by pulsed laser and high concentration of silicon carbide nanoparticles (laser energy is 800mJ, frequency is 10Hz, exposure time is 5sec and 90%concentration ratio)

When the concentration ratio of nanofluid was reduced to 50% (of nanoparticles), the laser pulse energy is 600mJ, repetition rate is 5Hz and exposure time (5-10) sec, the microholes were obtained on the target. The FESEM image of Aluminium alloy (figure (6)) shows some amount of (SiC) nanoparticles are melted in and come down to surface to drill micro holes and some of (SiC) nanoparticles accumulated sufficiently forming cracks on the target.

If the concentration ratio of the nanofluid is reduced to 5% (of the nanoparticles), the laser pulse energy is 600mJ, repetition rate is 5Hz and exposure time is (5-10)sec, the micro and nano holes for aluminium alloy are achieved with the minimum heat affected zone (HAZ) width. Figure (7) shows few numbers of fine nano holes appear on the target due to light concentration of nanoparticles. The number of nanoparticles in the fluid will be small. This will lead to make the number of these particles per unit volume is also small. These small sizes of nanoparticle groups will melt in a short time according to its size and density causing these holes.

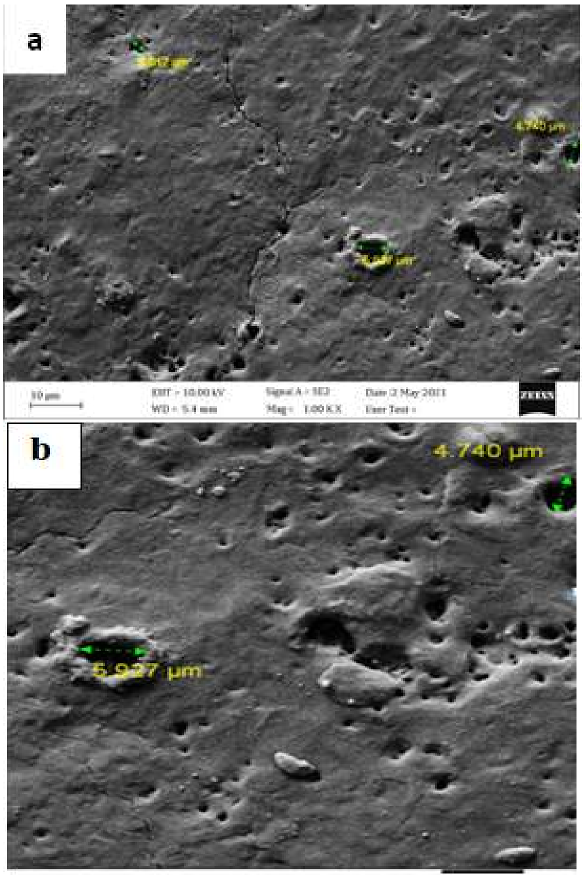

Figure (6, a-b): The FESEM test of aluminium alloy with laser energy of 600mJ, repetition rate of 5Hz, exposure time is10sec, and 50% concentration ratio of silica carbide nanoparticles

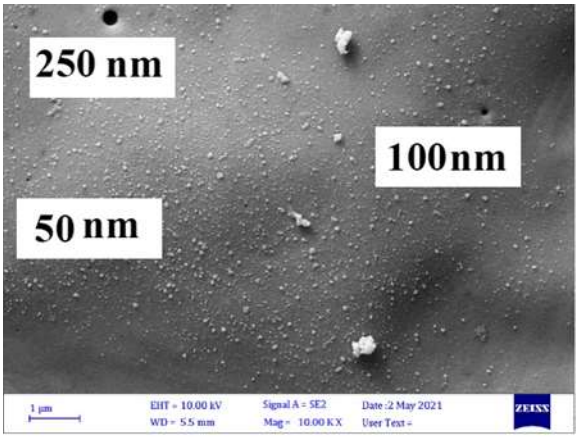

Figure (7): The FESEM test of nanoholes in aluminium alloy with laser energy of 600mJ, 5Hz repetition rate, exposure time is 5sec and 5% nanoparticle concentration ratio

4.3 Drilling of Aluminium alloy with tungsten carbide (WC) nanoparticles

When the concentration ratio of nanofluid is 90% (of the nanoparticles), the laser pulse energy is 800mJ, repetition rate is 10Hz and exposure time is (30sec), the aggregations of nanoparticles were obtained, as shown in figure (8a). Irregular holes in millimetre were obtained also on the target, as shown in figure (8b). This belongs to the high laser energy, and high concentration of (WC) nanoparticles. These nanoparticles have larger grain size, higher density and different physical properties as compared to SiC nanoparticles. Therefore, large numbers of nanoparticles need more time (30sec.) to melt and drill, they accumulated and fallen on to drill the target with irregular holes and also aggregated on the surface.

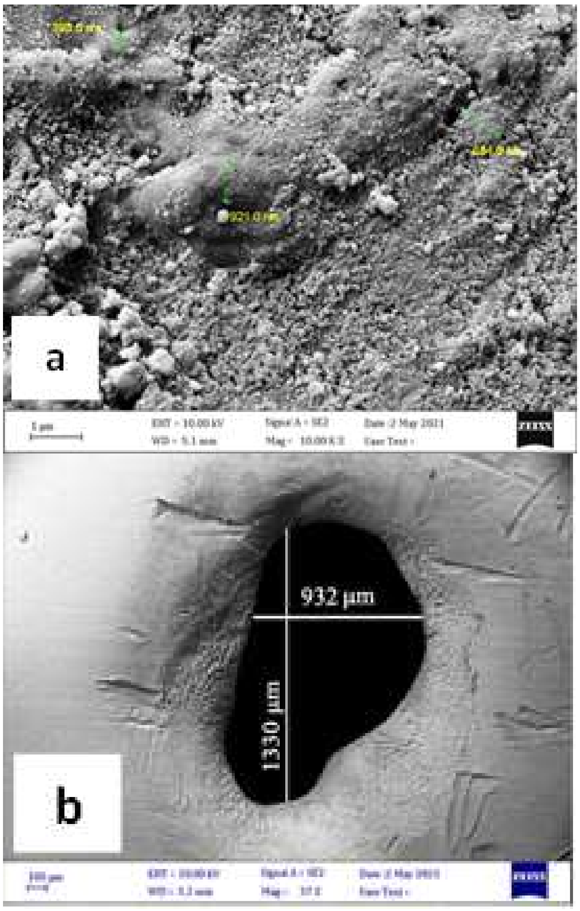

Figure (8, a-b): The FESEM test of aggregated nanoparticles and holes in aluminium alloy when the laser energy is 800mJ, repetition rate is 10Hz, exposure is 30sec and 90% concentration ratio of nanoparticles

Changing the concentration ratio of nanofluid to 50% (of the nanoparticles), the laser pulse energy is 600mJ, repetition rate is 5Hz and exposure time (30)sec, the microholes were obtained on the target, as shown in figure (9).

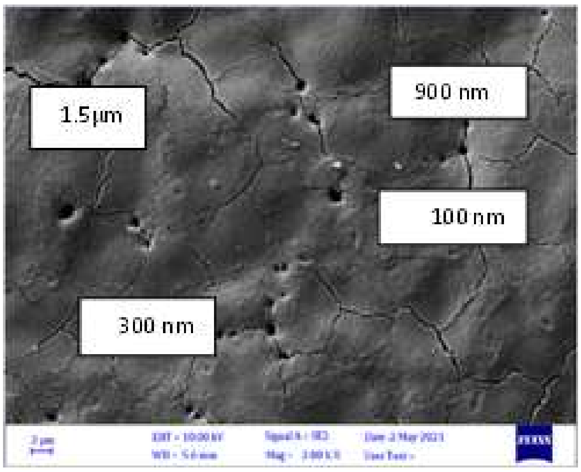

Figure (9): The FESEM test of micro holes in aluminium alloy with laser energy of 600mJ, repetition rate is 5Hz, exposure time is 30sec and 50% concentration ratio of nanoparticles

If the concentration ratio of the nanofluid is reduced to be as 5% (of the nanoparticles) and sprayed it on the target, the laser pulse energy is 600mJ, repetition rate is 5Hz and exposure time is (30)sec, microholes and nanoholes for the 8009 aluminium alloy are achieved, as shown in Figure (10 (a,b)). In this figure, less regular holes were obtained as compared to holes achieved from SiC nanoparticles (figure (7)). The reason for this is due to the difference in the melting point and physical properties between the two nanoparticles as the tungsten carbide nanoparticle needs more time to melt and fall to drill. Due to the continues nanofluid spraying process during the work, part of the tungsten carbide nanoparticle will be heated but doesn't melt. These heated nanoparticles will come down into the metal, causing irregularities in the diameter of the holes, but do not cause aggregations (or may cause a small aggregation) because the concentration here is little.

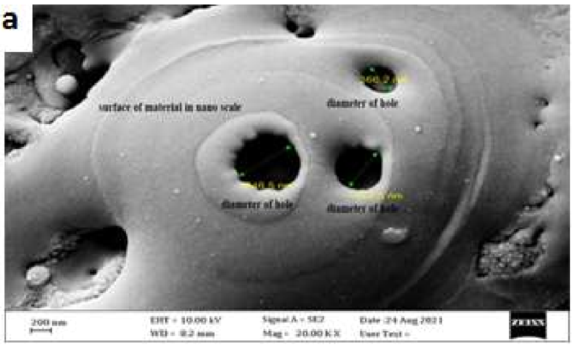

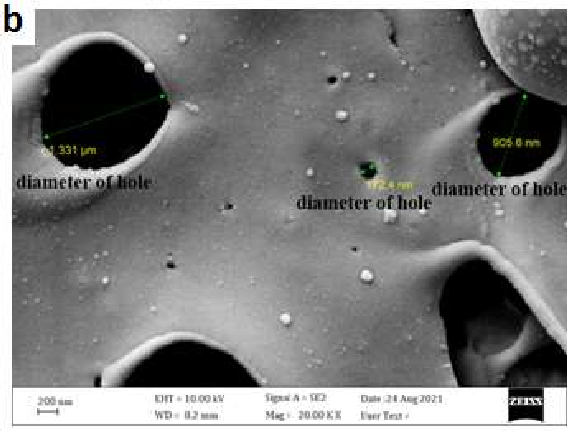

Figure (10, a-b): The FESEM test of nano holes in aluminium alloy with laser energy of 600mJ, repetition rate of 5Hz, exposure time is 30sec and 5% concentration ratio of nanoparticles.

5. Conclusion

The micro and nanodrlling process in 8009 Al alloy were investigated. The micro and nanoholes showed a strong dependence on laser parameters, specially, when the pulse laser energy is 600, and repetition rate is 5Hz. The difference in the physical properties of the tungsten carbide and silica carbide nanoparticles used in this study, like melting point(2870°C, 1650°C), density(15.63g/cc, 3.8g/cc), and grain diameter(55nm, 50nm) respectively, lead to use different exposure time for the two nanoparticle types which play an important role in the numbers and the size of the investigated holes.

6. References

[1] Kansal, H., Jain, A., & Grover, V. (2017). *"Micro Drilling and Drilling with Nano Materials*: A Review". 4th National Conference on Advancements in Simulation and Experimental Techniques in Mechanical Engineering. Department of Mechanical Engineering. Thapar University, Patiala, India

[2] Bhuyan, S. K. (2009). *"Micro-Drilling using Nd-YAG Laser* (Doctoral dissertation)". INDIAN INSTITUTE OF TECHNOLOGY, DELHI).

[3] Roy, N., Kuar, A. S., Mitra, S., & Acherjee, B. (2015). *"Nd: YAG laser microdrilling of SiC-30BN nanocomposite: Experimental study and process optimization".* In Lasers Based Manufacturing (pp. 317-341). Springer, New Delhi.

[4] Casalino, G., Losacco, A. M., Arnesano, A., Facchini, F., Pierangeli, M., & Bonserio, C. (2017). *"Statistical analysis and modelling of an Yb: KGW femtosecond laser micro-drilling process*". Procedia CIRP, 62, 275-280.

[5] Zhao, W., & Wang, L. (2018). "*Microdrilling of through-holes in flexible printed circuits using picosecond ultrashort pulse laser*". Polymers, 10(12), 1390.

[6] Singh, P., Pramanik, A., Basak, A. K., Prakash, C., & Mishra, V. (2020). "Developments of non-conventional drilling methods—a review". The International Journal of Advanced Manufacturing Technology, 106(5), 2133-2166.

[7] Pyatenko, A., Wang, H., Koshizaki, N., & Tsuji, T. (2013*)." Mechanism of pulse laser interaction with colloidal nanoparticles*". Laser & Photonics Reviews, 7(4), 596-604.

[8] Farahmand, P., Liu, S., Zhang, Z., & Kovacevic, R. (2014). *"Laser cladding assisted by induction heating of Ni–WC composite enhanced by nano-WC and La2O3*". Ceramics International, 40(10), 15421-15438.

[9] Farahmand, P., Liu, S., Zhang, Z., & Kovacevic, R. (2014*). "Laser cladding assisted by induction heating of Ni–WC composite enhanced by nano-WC and La2O3".* Ceramics International, 40(10), 15421-15438.

[10] Tunna, L., O'Neill, W., Khan, A., & Sutcliffe, C. (2005). *"Analysis of laser micro drilled holes through aluminium for micro-manufacturing applications".* Optics and Lasers in Engineering, *43*(9), 937-950.

[11] Li, S. H., Yang, W., Liu, Y., Song, X. R., Liu, R., Chen, G., ... & Yang, H. H. (2018). *"Engineering of tungsten carbide nanoparticles for imaging-guided single 1,064 nm laser-activated dual-type photodynamic and photo thermal therapy of cancer".* Nano Research, 11(9), 4859-4873.

[12] Barbaux, Y., & Pons, G. (1993)." *New rapidly solidified aluminium alloys for elevated temperature applications on aerospace structures*‶. Le Journal de Physique IV, 3(C7), C7-191.

[13] Liu, H., Zhang, H., Jiang, F., & Fu, D. (2019).‶ *The intermetallic formation in the extruded AlSi20/8009 aluminium alloy during annealing treatment".* Vacuum, 168, 108800.

[14] Liu, H., Zhang, H., Jiang, F., & Fu, D. (2019). ‶*The intermetallic formation in the extruded AlSi20/8009 aluminum alloy during annealing treatment"*. Vacuum, 168, 108800.

[15] Jankowski, J. (2019). *"Development of Novel High Temperature Aluminum Alloys "*. Colorado School of Mines.

[16] Liu, H. B., Su, H. G., Fu, D. F., Jiang, F. L., & Zhang, H. (2020). *"Phase evolution in AlSi20/8009 aluminum alloy during high temperature heating near melting point and cooling processes"*. Transactions of Nonferrous Metals Society of China, 30(5), 1157-1168

[17] Kuchariková, L., Liptáková, T., Tillová, E., Kajánek, D., & Schmidová, E. (2018)." *Role of chemical composition in corrosion of aluminum alloys "*. Metals, 8(8), 581.

[18] Rafati, R., Smith, S. R., Haddad, A. S., Novara, R., & Hamidi, H. (2018). "*Effect of nanoparticles on the modifications of drilling fluids properties: A review of recent advances"*. Journal of Petroleum Science and Engineering, 161, 61-76.

التثقيب المايكروي و النانوي بالليزر لسبيكة الألومنيوم باستخدام الدقائق النانوية من كربيد التنجستن و كربيد السيليكا

نبراس حامد عبد، محمود شاكر محمود
معهد الليزر للدراسات العليا، جامعة بغداد، العراق

الخلاصة

تم إنتاج الثقوب المايكروية و النانوية بواسطة ليزر Q-switched Nd: YAG (1064 نانومتر) مع سبيكة Al 8009 باستخدام الدقائق النانوية. تم استخدام نوعين من الدقائق النانوية مع هذه السبيكة و هي كربيد التنجستن (WC) وكربيد السيليكا (SiC). في هذا العمل، تم عمل الثقوب المايكروية و النانوية بواسطة نبضات ليزرية بطاقات مختلفة (600 ، 700 و 800) مللي جول، ومعدلات تكرار مختلفة (5 هرتز و 10 هرتز) وتراكيز مختلفة من الدقائق النانوية (90٪، 50٪ و 5٪). تشير النتائج إلى أن الثقوب المايكروية و النانوية قد تحققت عندما تكون طاقة نبضة الليزر 600 مللي جول ، ومعدل تكرار نبض الليزر 5 هرتز، وتراكيز الدقائق النانوية (لنوعي الدقائق النانوية) 5٪. تزداد أقطار الثقوب إلى ملليمترات وتتشكل الشقوق مع زيادة طاقة نبضة الليزر ، ومعدل تكرار نبض الليزر باستخدام تركيز عالٍ من الموائع النانوية.